

**NASA TECHNICAL
MEMORANDUM**



NASA TM X-1304

NASA TM X-1304

FACILITY FORM 602

N67 10234
(ACCESSION NUMBER)

80
(PAGES)

TMX-1304
(NASA CR OR TMX OR AD NUMBER)

(THRU)

(CODE)

(CATEGORY)

PRICE \$

PRICE(S) \$

Hard copy (HC)

Microfiche (MF)

8-1304 July 65

**AERODYNAMIC CHARACTERISTICS OF
A 0.187-SCALE MODEL OF A TARGET
MISSILE AT MACH 1.80 TO 2.16**

by William A. Corlett

Langley Research Center

Langley Station, Hampton, Va.

AERODYNAMIC CHARACTERISTICS
OF A 0.187-SCALE MODEL OF A TARGET MISSILE

AT MACH 1.80 TO 2.16

By William A. Corlett

Langley Research Center
Langley Station, Hampton, Va.

NATIONAL AERONAUTICS AND SPACE ADMINISTRATION

For sale by the Clearinghouse for Federal Scientific and Technical Information
Springfield, Virginia 22151 - Price \$2.50

AERODYNAMIC CHARACTERISTICS
OF A 0.187-SCALE MODEL OF A TARGET MISSILE
AT MACH 1.80 TO 2.16

By William A. Corlett
Langley Research Center

SUMMARY

An investigation has been made in the Langley Unitary Plan wind tunnel at Mach numbers 1.80, 2.00, and 2.16 to determine the aerodynamic characteristics of a 0.187-scale model of a target missile. The model consisted of a fuselage (of fineness ratio 22.9) with conventional wings and tail-fin controls, above which was a large nacelle, pylon-mounted. The tests were conducted through an angle-of-attack range of approximately -4° to 12° and an angle-of-sideslip range from approximately -6° to 6° at a constant Reynolds number of 10.55×10^6 based on fuselage length.

The results indicated satisfactory longitudinal and directional stability characteristics at low angles of attack throughout the test Mach number range; however, some pitch-up and yaw nonlinearity was indicated at the higher angles of attack. A reduction in nacelle mass-flow ratio resulted in a sizable increase in drag coefficient and zero-lift pitching-moment coefficient. The pitch control effectiveness of the tail fins increased slightly with increase in angle of attack. Differential deflection of the tail fins provided roll control with sizable amounts of yaw and corrective deflections of the rudder added to the roll power.

INTRODUCTION

An investigation of the supersonic aerodynamic characteristics of a 0.187-scale model of a target missile was conducted in the Langley Unitary Plan wind tunnel. The model had a fuselage with a fineness ratio of 22.9 and a large ramjet engine nacelle that was pylon-mounted above the fuselage. The model had conventional wings and all-movable tail fins to provide control.

The objectives of these tests were to obtain performance, stability, and control data for the configuration and its modifications. Specific objectives of the investigation were the effect of nacelle mass-flow ratio on the aerodynamic characteristics, effectiveness of controls, and determination of hinge and bending moments on the left tail fin. In addition,

the effect of model attitude and Mach number on the fuel-control-probe pressure sensor was investigated.

The tests were performed in the Langley Unitary Plan wind tunnel at Mach numbers of 1.80, 2.00, and 2.16 through angles of attack from about -4° to 12° and angles of side-slip from about -6° to 6° at a constant Reynolds number of 10.55×10^6 based on fuselage length.

SYMBOLS

The results are referenced to the body axis, except for lift and drag which are presented about the stability axis. The location of the moment center is 33.16 inches (84.23 cm) aft of the nose-probe juncture and on the fuselage center line. The symbols are defined as follows:

A	maximum cross-sectional area of fuselage
b_F	tail-fin span
C_A	axial-force coefficient, $\frac{\text{Axial force}}{qA}$
$C_{A,b}$	base axial-force coefficient, $\frac{\text{Base axial force}}{qA}$
$C_{A,i}$	internal axial-force coefficient, $\frac{\text{Internal axial force}}{qA}$
C_B	bending-moment coefficient (left fin), $\frac{\text{Bending moment}}{qS_F b_F}$
C_D	drag coefficient, $\frac{\text{Drag}}{qA}$
$C_{D,b}$	base-drag coefficient, $\frac{\text{Base drag}}{qA}$
$C_{D,i}$	internal-drag coefficient, $\frac{\text{Internal drag}}{qA}$
C_L	lift coefficient, $\frac{\text{Lift}}{qA}$
C_l	rolling-moment coefficient, $\frac{\text{Rolling moment}}{qAl}$

C_m	pitching-moment coefficient, $\frac{\text{Pitching moment}}{qAl}$
$C_{m,0}$	pitching-moment coefficient at $C_L = 0$
C_N	normal-force coefficient, $\frac{\text{Normal force}}{qA}$
C_n	yawing-moment coefficient, $\frac{\text{Yawing moment}}{qAl}$
C_H	hinge-moment coefficient (left fin), $\frac{\text{Hinge moment}}{qS_F \bar{c}_F}$
C_Y	side-force coefficient, $\frac{\text{Side force}}{qA}$
\bar{c}_F	tail-fin mean aerodynamic chord
L/D	lift-drag ratio
l	fuselage length
M	free-stream Mach number
m	mass flow through nacelle, lbm/sec (kilogram/second)
m_∞	mass flow at free-stream conditions through a stream tube of cross-sectional area equal to the inlet area, lbm/sec (kilogram/second)
p_t	tunnel stagnation pressure, psfa (newton/meter ²)
p_t'	total pressure
q	free-stream dynamic pressure
r	radius, in. (centimeter)
S_F	tail-fin surface area
α	angle of attack, deg

β angle of sideslip, deg

δ_F tail-fin deflection angle (positive leading edge up), deg

δ_p pylon rudder deflection angle (negative trailing edge left), deg

Subscripts:

L left

R right

Designations:

N_1, N_2, N_0 nacelle configurations (table I)

APPARATUS AND TESTS

Tunnel

The investigation was conducted in the low Mach number test section of the Langley Unitary Plan wind tunnel, which is a continuous-flow, variable-pressure facility. The test section is about 4 by 4 feet (1.26 m) in cross section and about 7 feet (2.13 m) in length. The nozzle leading to the section is of the asymmetric sliding-block type which permits continuous variation in Mach number from 1.47 to 2.86.

Model

The test configuration was a 0.187-scale model of a target missile. Dimensional details of the model are presented in figure 1 and table I, and photographs of the model are shown in figure 2. The model was constructed so that the balance-sting combination could be installed in the fuselage for the flow-through nacelle configurations, or in the nacelle (with a conical fairing over the inlet) for the configurations with the fuselage afterbody. Provision was also made for hinge- and bending-moment instrumentation of the tail fin.

The fuselage, which was composed of an ogive nose, cylindrical body, and ogive afterbody, had a length-diameter ratio of 22.9. The conventional wings were trapezoidal in planform with a NACA 65A003 airfoil section. The trapezoidal tail fins had an anhedral angle of 34° and a NACA 65A005 airfoil section.

Each of the three nacelles had the same external dimensions and were pylon-mounted above the fuselage. A fuel-control wedge-and-pitot unit was attached to and protruded from the pylon leading edge. Two flow-through nacelles, N_1 and N_2 , had venturis sized to obtain 0.85 and 0.65 mass-flow ratios, m/m_∞ , respectively, at Mach 1.5 with choked flow at the throat. (See table I for nacelle dimensions.) A plugged nacelle N_0 had a 5-inch (12.70-cm) cone-shaped fairing attached to the inlet. A small vertical fin with beveled leading and trailing edges was located in the plane of symmetry on top of the nacelle.

Various external protuberances were affixed to the model to simulate the flight vehicle fully.

Tests

The tests were performed at Mach numbers of 1.80, 2.00, and 2.16 with a constant Reynolds number of 10.55×10^6 based on fuselage length. A constant stagnation temperature of 150°F (338°K) was maintained. The dewpoint was kept below -30°F (238°K) to insure negligible condensation effects. Angles of attack were varied from about -4° to 12° and angles of sideslip were varied from about -6° to 6° .

All tests were performed with 1/16-inch (0.159-cm) strips of No. 60 carborundum grit affixed to the nose 1 inch (2.54 cm) aft of the nose-probe juncture and on all other surfaces 0.5 inch (1.27 cm) aft, in the streamwise direction from the leading edges.

Measurements and Corrections

Aerodynamic forces and moments were determined with an internally mounted electrical strain-gage balance. The fuselage base pressure was measured by a single static orifice located in the fuselage cavity. For the plugged nacelle, the nacelle base pressure was measured by a single static tube extending into the nacelle cavity. The flow-through nacelles were provided with static-pressure orifices located at the nacelle base. Mass-flow ratio, m/m_∞ , and internal drag were determined with a rake which had 16 total-pressure and 2 static-pressure orifices located at the nacelle exit.

The results have been adjusted to free-stream conditions acting over the bases of the fuselage and nacelle (figs. 3, 4, and 5). Internal drag corrections for the flow-through nacelles, N_1 and N_2 , are presented in figure 6. All data have been corrected for deflection of the balance and sting due to aerodynamic loads and for tunnel-flow angularity.

Schlieren photographs of several of the configurations are presented as figure 7.

Accuracy

The estimated accuracies of the data, based on calibrations and data repeatability, are within the following limits:

C_N	± 0.11
C_L	± 0.11
C_A	± 0.02
C_D	± 0.02
C_m	± 0.01
C_l	± 0.002
C_n	± 0.01
C_Y	± 0.11
α , deg	± 0.10
β , deg	± 0.10
M	± 0.015

PRESENTATION OF RESULTS

The results of this investigation are presented in the following figures:

	Figure
Effect of balance-sting location on the aerodynamic characteristics of identical configurations. Afterbody off; conical fairing over nacelle inlet; $\delta_F = 0^0$; $\delta_p = 0^0$	8
Effect of mass-flow ratio of nacelles on the longitudinal aerodynamic characteristics. Balance in fuselage; $\delta_F = 0^0$; $\delta_p = 0^0$	9
Effect of tail fins and tail-fin deflections on the longitudinal aerodynamic characteristics. Balance in nacelle; afterbody off; $\delta_p = 0^0$	10
Effect of fuselage afterbody on the longitudinal aerodynamic characteristics. Balance in nacelle; $\delta_F = 0^0$; $\delta_p = 0^0$	11
Effect of nose probe and speed brake on the longitudinal aerodynamic characteristics. Balance in nacelle; afterbody on; $\delta_F = 0^0$; $\delta_p = 0^0$; $M = 2.00$	12
Effect of angle of attack on the lateral aerodynamic characteristics for the N_1 nacelle configuration. Balance in fuselage; $\delta_F = 0^0$; $\delta_p = 0^0$; $M = 2.00$	13
Effect of mass-flow ratio of nacelles on the lateral aerodynamic characteristics. Balance in fuselage; $\delta_F = 0^0$; $\delta_p = 0^0$	14

	Figure
Effect of differential tail-fin deflections on the lateral aerodynamic characteristics. Balance in nacelle; afterbody off; $\delta_p = 0^\circ$	15
Effect of pylon rudder control on the lateral aerodynamic characteristics. Balance in nacelle; afterbody off; $\delta_F = 0^\circ$	16
Effect of fuselage afterbody on the lateral aerodynamic characteristics. Balance in nacelle; $\delta_F = 0^\circ$; $\delta_p = 0^\circ$	17
Variation of hinge- and bending-moment coefficients with angle of attack for the left tail fin. Balance in nacelle; afterbody off	18
Variation of fuel-control-probe pressure, p'_t/p_t , with angle of attack. Balance in fuselage; N_1 nacelle	19

DISCUSSION

Effect of Balance Location

The scope of this investigation required tests of the model with the balance-sting combination fastened in the fuselage and also in the nacelle; therefore, it was considered necessary to perform tests of identical configurations differing only in balance mounting location to determine whether any variation in data existed. A comparison of the aerodynamic characteristics obtained from these tests is presented in figure 8. The slight difference indicated in C_N and C_L between the two balance locations may be attributed to a small variation in tunnel flow angle due to the change in model position in the tunnel when the balance was moved to the nacelle. Also, the small variation in C_m possibly reflects the accuracy of transferring data obtained with the balance located in the nacelle to the moment center on the fuselage center line. There was no significant difference noted in the lateral aerodynamic characteristics.

Longitudinal Characteristics

The effects of nacelle mass-flow ratio on the aerodynamic characteristics in pitch are presented in figure 9 for $M = 1.80$ and $M = 2.00$. The measured mass-flow ratio, m/m_∞ , for the flow-through nacelles was 0.90 at $M = 1.80$, 0.93 at $M = 2.00$ for N_1 ; and 0.69 at $M = 1.80$, and 0.72 at $M = 2.00$ for N_2 . Included in this figure are data for the nacelle inlet faired with a conical cover. The data for this latter configuration have been adjusted to free-stream static conditions at the base of the nacelle. A decrease in mass-flow ratio leads to decreased lift capability and a sizable increase in drag coefficient which, in turn, causes a noticeable decrease in lift-drag ratio for the configuration. Fairing the nacelle inlet reduced the drag but had no significant effect on the lift-curve slope or the stability of the configuration.

The normal force and lift curves are essentially linear throughout the test angle-of-attack range at all Mach numbers, and the pitching-moment curves are linear at low angles of attack, although at the higher angles of attack there is a slight pitch-up tendency (figs. 9 and 10).

The control effectiveness of the tail fins (fig. 10) is about the same for positive and negative deflections of 5° . There is a slight increase in fin control effectiveness with increase in angle of attack at each Mach number. Increasing the Mach number results in a general decrease in control effectiveness.

The effect of the fuselage afterbody on the aerodynamic characteristics in pitch is shown in figure 11. These data show that the fuselage afterbody causes an increase in drag coefficient (because of the absence of the base-drag correction that was applied to the afterbody-off configuration) and a decrease in $C_{m,0}$. The afterbody had little effect on the stability characteristics of the configuration. There is also a slight increase in lift for the configuration with the fuselage afterbody on. It should be noted, however, that there is a tunnel-wall shock reflection striking the afterbody at angles of attack to about 10° at $M = 1.80$ and at small positive angles of attack even at $M = 2.00$. (See schlieren photographs of fig. 7.) The data obtained in this condition are shown by flagged symbols in figures 10, 11, and 12.

There are essentially no effects of the nose probe on the pitch characteristics of the model at $M = 2.00$. (See fig. 12.) Deflection of the speed brake caused a significant increase in drag of the configuration and a substantial decrease in $C_{m,0}$.

Lateral Characteristics

The effects of angle of attack on the lateral aerodynamic characteristics of the N_1 nacelle configuration are presented in figure 13 for a Mach number of 2.00. The rolling- and yawing-moment coefficients are reasonably linear with β , although an increase in α tends to produce some nonlinearity at the highest sideslip angles. These data show that the configuration is directionally stable and has positive effective dihedral for the selected center-of-gravity location.

There is little or no effect of change in nacelle mass-flow ratio on the lateral stability characteristics of the configuration, although the faired nacelle inlet configuration N_0 displays a slight decrease in positive effective dihedral. (See fig. 14.)

The data of figure 15 show that differential tail-fin deflection was effective in providing roll control, but sizable amounts of yaw resulted. The deflections required to balance the rolling moment due to positive sideslip resulted in a yawing moment that tended to trim at a negative angle of sideslip. Some yaw correction can be obtained by deflection of the rudder (fig. 16) but the deflections required to overcome the yaw due to

differential tail-fin deflection, in turn, added to the roll power. In fact, the use of the rudder to trim the rolling moment due to positive sideslip resulted in a tendency for the yaw to be self-trimming. (See fig. 16.)

Only small effects of the fuselage afterbody on the lateral aerodynamic characteristics of the configuration were noted. (See fig. 17.)

Hinge- and Bending-Moment Characteristics

The variation of the hinge-moment and bending-moment coefficients with angle of attack for the left tail fin are presented in figure 18. The hinge-moment axis is at body station 44.529 and the bending-moment axis is at the intersection of the fin with the fuselage. There are only small effects of fin deflection (for $\pm 5^\circ$) or angle of attack on the hinge-moment coefficients in the test Mach number range. However, there is an increase in the magnitude of bending moment with fin deflection and a relatively linear increase in bending-moment coefficient occurs with increasing angle of attack at each test Mach number for each fin deflection.

Fuel-Control Sensor Characteristics

The data presented in figure 19 indicate that the fuel-control probe is relatively free of interference effects in the angle-of-attack range at test Mach numbers of 1.80 and 2.00.

CONCLUDING REMARKS

An investigation has been made to determine the aerodynamic characteristics of a 0.187-scale model of a target missile at Mach numbers from 1.80 to 2.16. The results indicate satisfactory longitudinal and directional stability characteristics at low angles of attack at the Mach numbers tested; however, some pitch-up and yaw nonlinearity was indicated at the higher test angles of attack. A reduction in nacelle mass-flow ratio resulted in a sizable increase in drag and zero-lift pitching-moment coefficients. The pitch control effectiveness of the tail fins increased slightly with increase in angle of attack. Differential deflection of the tail fins provided roll control with sizable amounts of yaw and corrective deflections of the rudder added to the roll power.

Langley Research Center,
National Aeronautics and Space Administration,
Langley Station, Hampton, Va., July 18, 1966.

TABLE I.- MODEL DETAILS

Afterbody (ogive contour with rounded tip):			
Length	11.18 in.	(28.40 cm)	
Fuselage (cylindrical body faired into nose with rounded tip (nose probe attached)):			
Length, including afterbody but excluding nose probe	60.28 in.	(153.11 cm)	
Diameter, maximum	2.244 in.	(5.700 cm)	
Fuel control probe (wedge and pitot unit attached to and protruding from pylon leading edge):			
Wedge angle	16°		
Tip location:			
Body station	32.105 in.	(81.547 cm)	
Vertical distance from fuselage reference line	2.726 in.	(6.924 cm)	
Nacelles (large ramjet; configurations N ₁ , N ₂ , and N ₀):			
	N ₁	N ₂	N ₀
Length	19.504 in. (49.540 cm)	19.504 in. (49.540 cm)	19.504 in. (49.540 cm)
Diameter, maximum	3.566 in. (9.058 cm)	3.566 in. (9.058 cm)	3.566 in. (9.058 cm)
Location of inlet, body station	33.525 in. (85.154 cm)	33.525 in. (85.154 cm)	33.525 in. (85.154 cm)
Inlet area	3.450 in ² (22.258 cm ²)	3.450 in ² (22.258 cm ²)	
Exit area	2.717 in ² (17.529 cm ²)	2.075 in ² (13.387 cm ²)	
Base area	4.356 in ² (28.103 cm ²)	4.997 in ² (32.239 cm ²)	7.073 in ² (45.632 cm ²)
Nacelle pylon (including trailing-edge rudder):			
Length	12.95 in.	(32.89 cm)	
Thickness	0.374 in.	(0.950 cm)	
Location of leading edge, body station	33.90 in.	(86.11 cm)	
Speed brake (rectangular fuselage panel located on lower mold line on fuselage):			
Length	1.248 in.	(3.170 cm)	
Width	1.169 in.	(2.970 cm)	
Deflection angle, trailing edge downward	45°		
Hinge-line location, body station	46.73 in.	(118.69 cm)	
Tail fins (trapezoidal planform with NACA 65A005 airfoil section):			
Area (one panel, exposed)	7.553 in ²	(48.729 cm ²)	
Span	2.749 in.	(6.982 cm)	
Anhedral angle	34°		
Aspect ratio	1.00		
Root chord	3.927 in.	(9.974 cm)	
Tip chord	1.571 in.	(3.990 cm)	
Mean aerodynamic chord	2.917 in.	(7.409 cm)	
1/4 mean aerodynamic chord location, body station	43.945 in.	(111.620 cm)	
Hinge-line location, body station	44.529 in.	(113.104 cm)	
Leading-edge sweep angle	40.6°		
Trailing-edge sweep angle	0°		
Vertical fin (located in the plane of symmetry on top of the nacelle; beveled leading and trailing edges):			
Area	1.863 in ²	(12.019 cm ²)	
Span	1.350 in.	(3.429 cm)	
Root chord	2.551 in.	(6.480 cm)	
Tip chord	0.208 in.	(0.528 cm)	
Leading-edge sweep angle	60.0°		
Trailing-edge sweep angle	0°		
Location of trailing edge, body station	45.039 in.	(114.399 cm)	
Wing (trapezoidal planform with NACA 65A003 airfoil section):			
Total area (including 25.076 in ² (161.78 cm ²) covered by fuselage)	84.899 in ²	(547.734 cm ²)	
Total span (including fuselage width)	13.090 in.	(33.249 cm)	
Aspect ratio	2.02		
Root chord	10.233 in.	(25.992 cm)	
Tip chord	0.819 in.	(2.080 cm)	
Mean aerodynamic chord	6.861 in.	(17.427 cm)	
1/4 mean aerodynamic chord location, body station	34.406 in.	(87.391 cm)	
Leading-edge sweep angle	60.0°		
Trailing-edge sweep angle	0°		

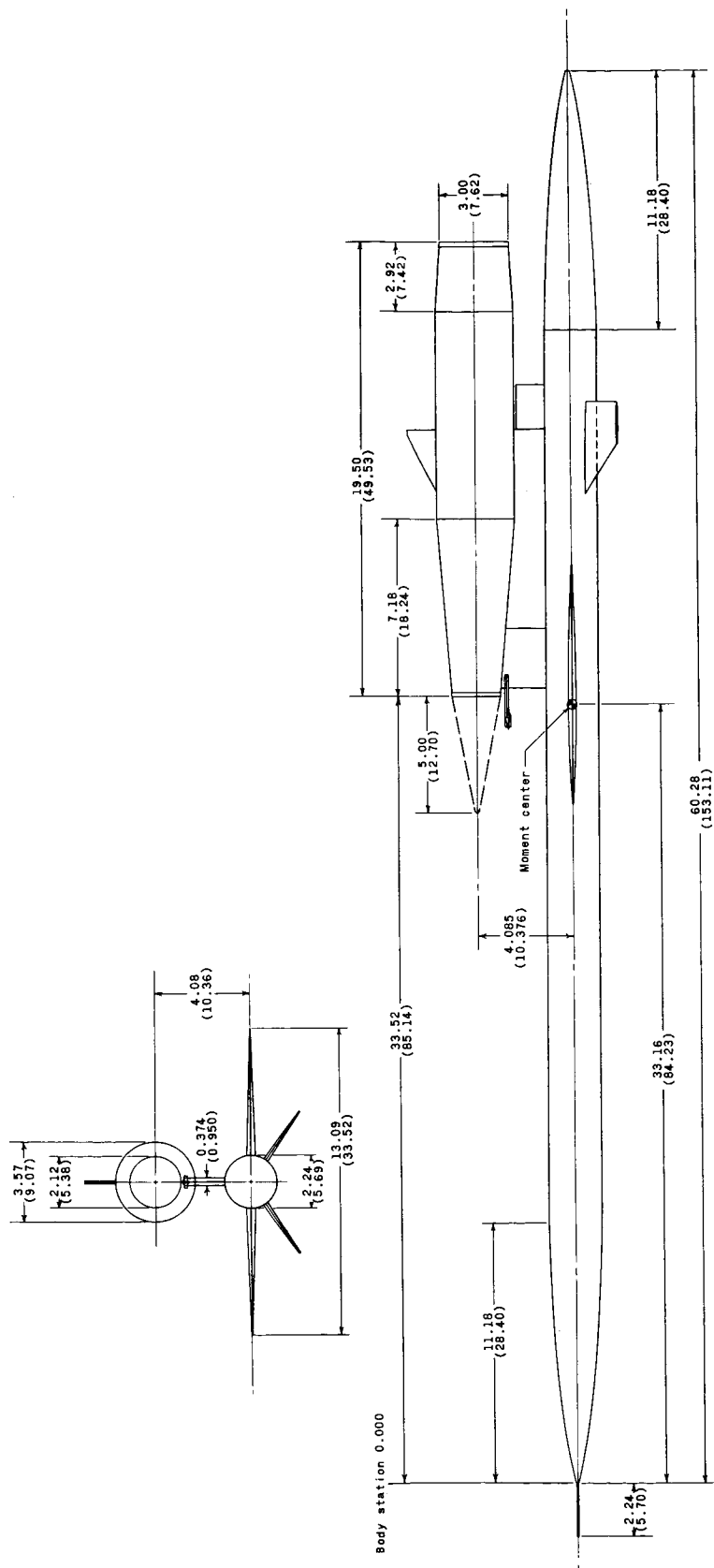


Figure 1.- Model details. (All dimensions are given in inches and parenthetically in centimeters.)

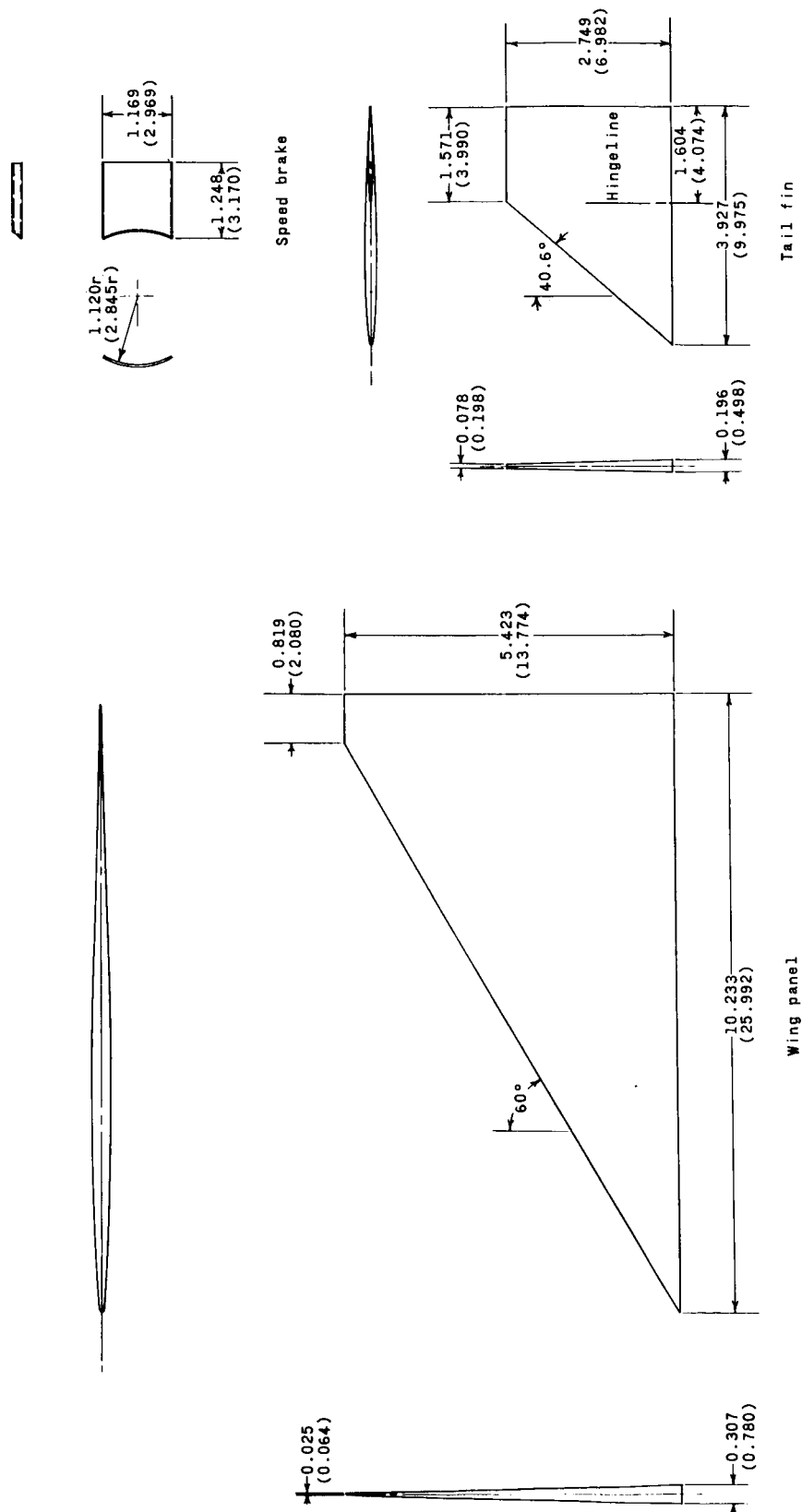
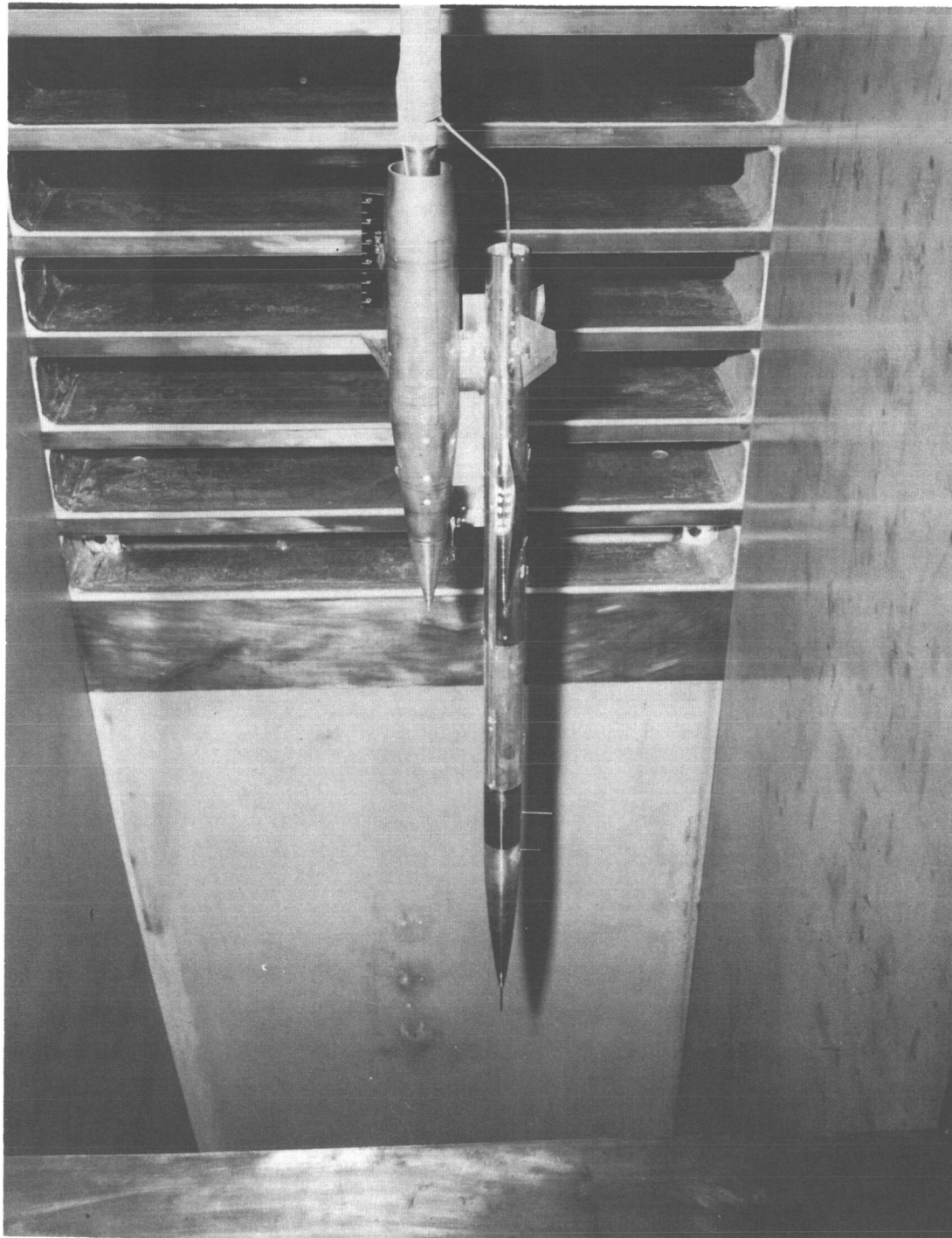


Figure 1.- Concluded.



(a) Balance in nacelle with afterbody off.

Figure 2.- Photographs of model.

L-65-697



L-65-701

(b) Balance in nacelle with afterbody on.

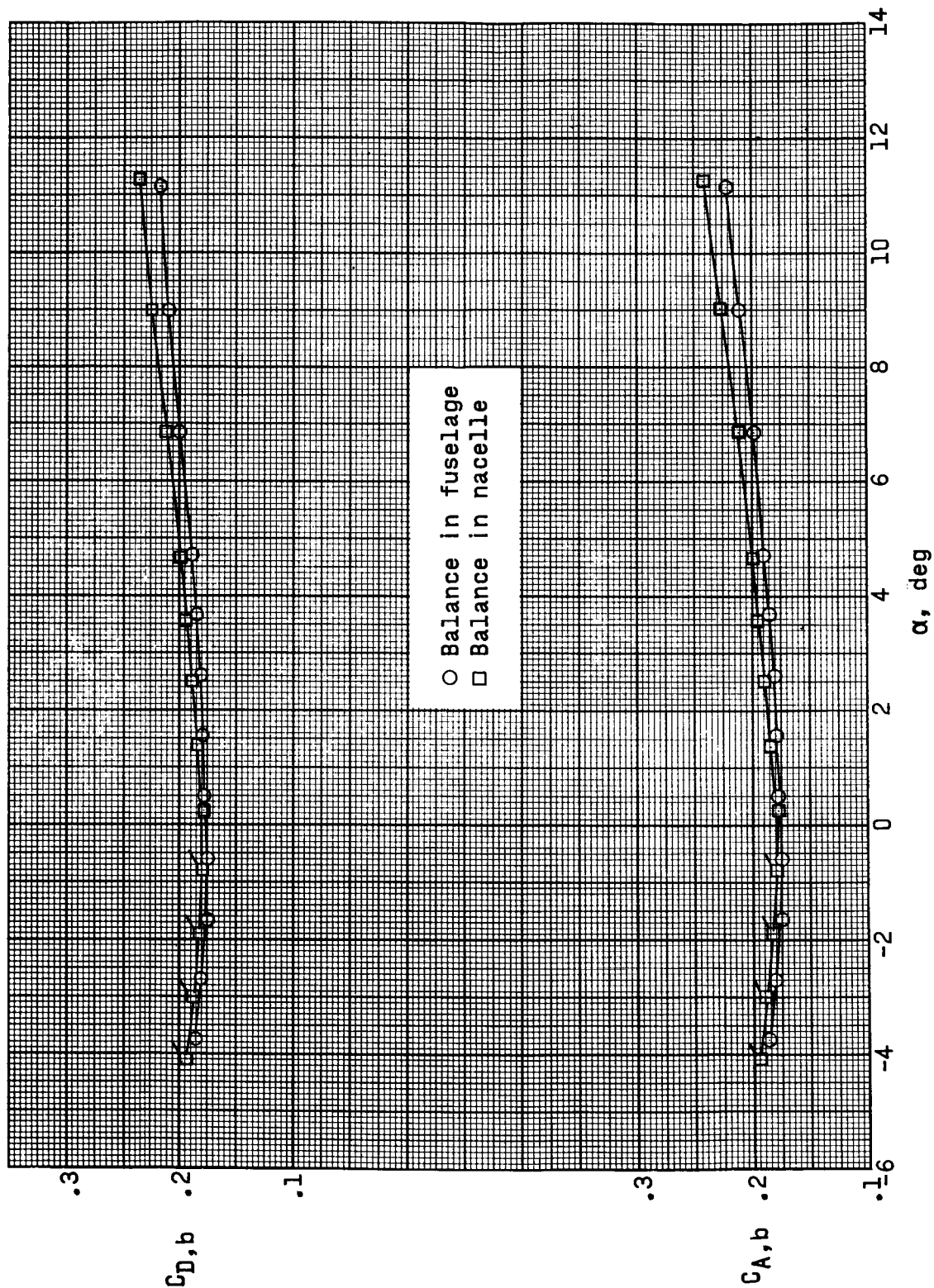
Figure 2.- Continued.



L-65-700

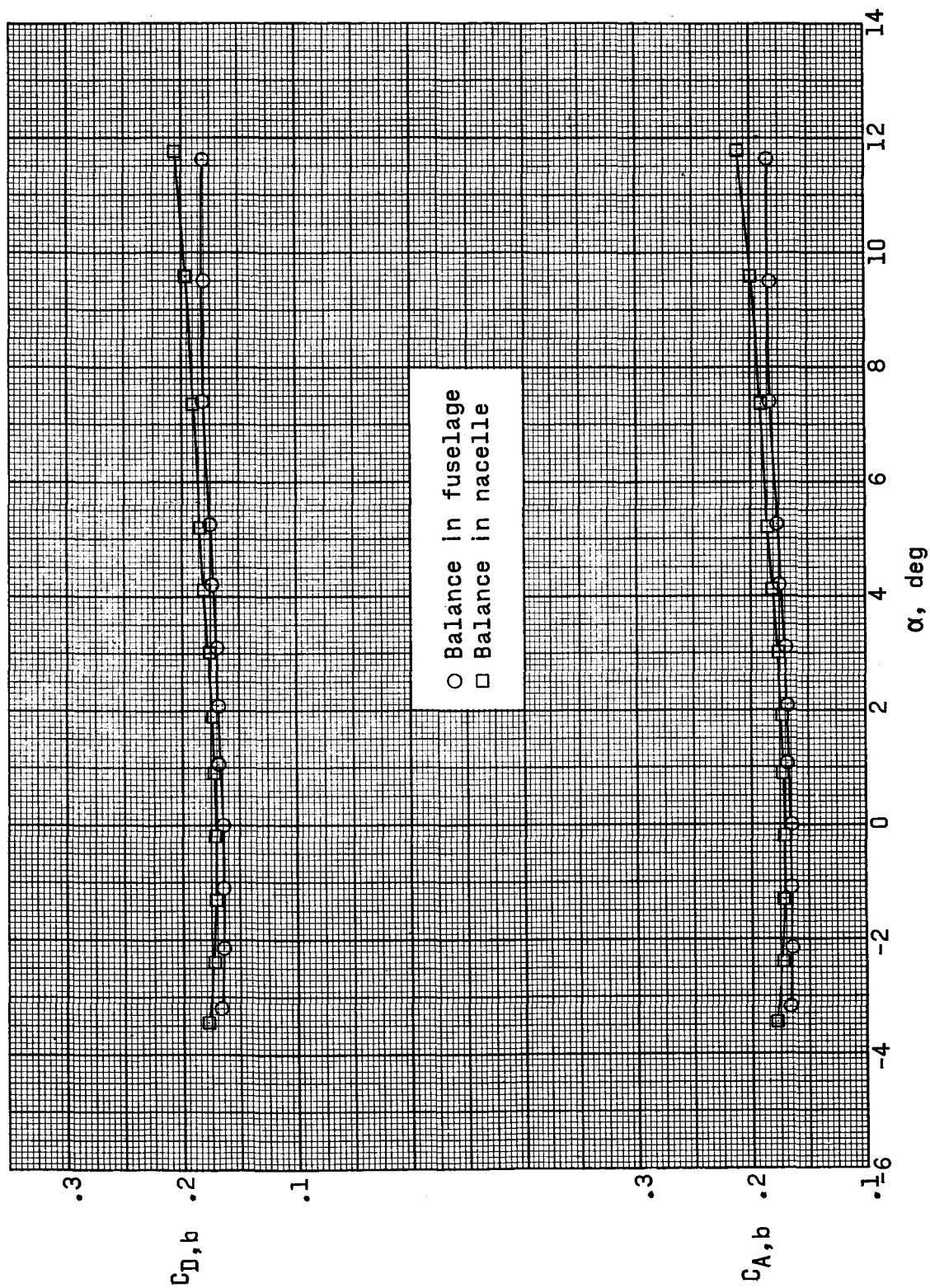
(c) Balance in fuselage with nacelle rake attached.

Figure 2.- Concluded.



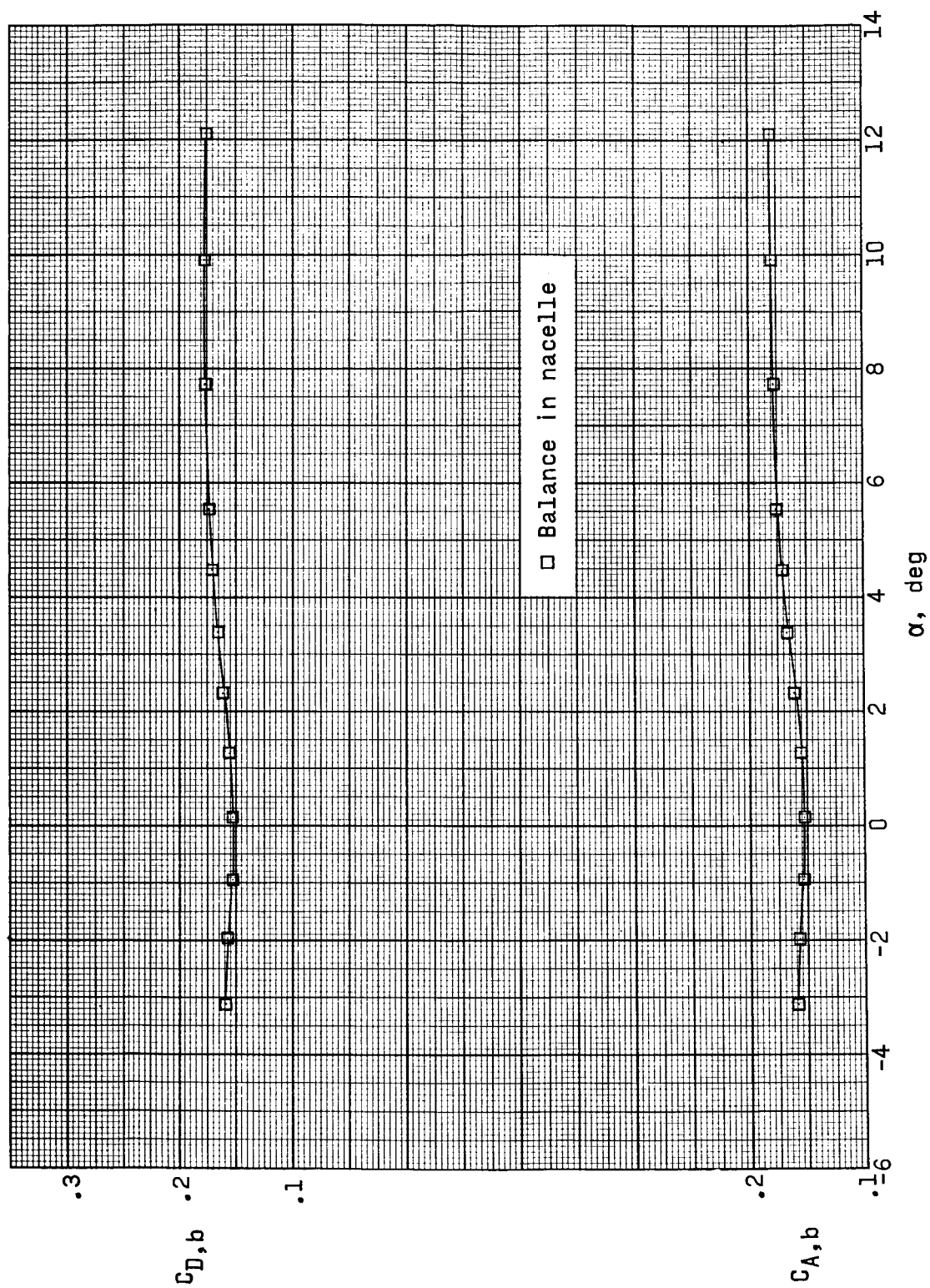
(a) $M = 1.80$.

Figure 3.- Variation of base axial-force and drag coefficients of fuselage with angle of attack. Afterbody off; $\delta_f = 0^\circ$; $\delta_p = 0^\circ$.



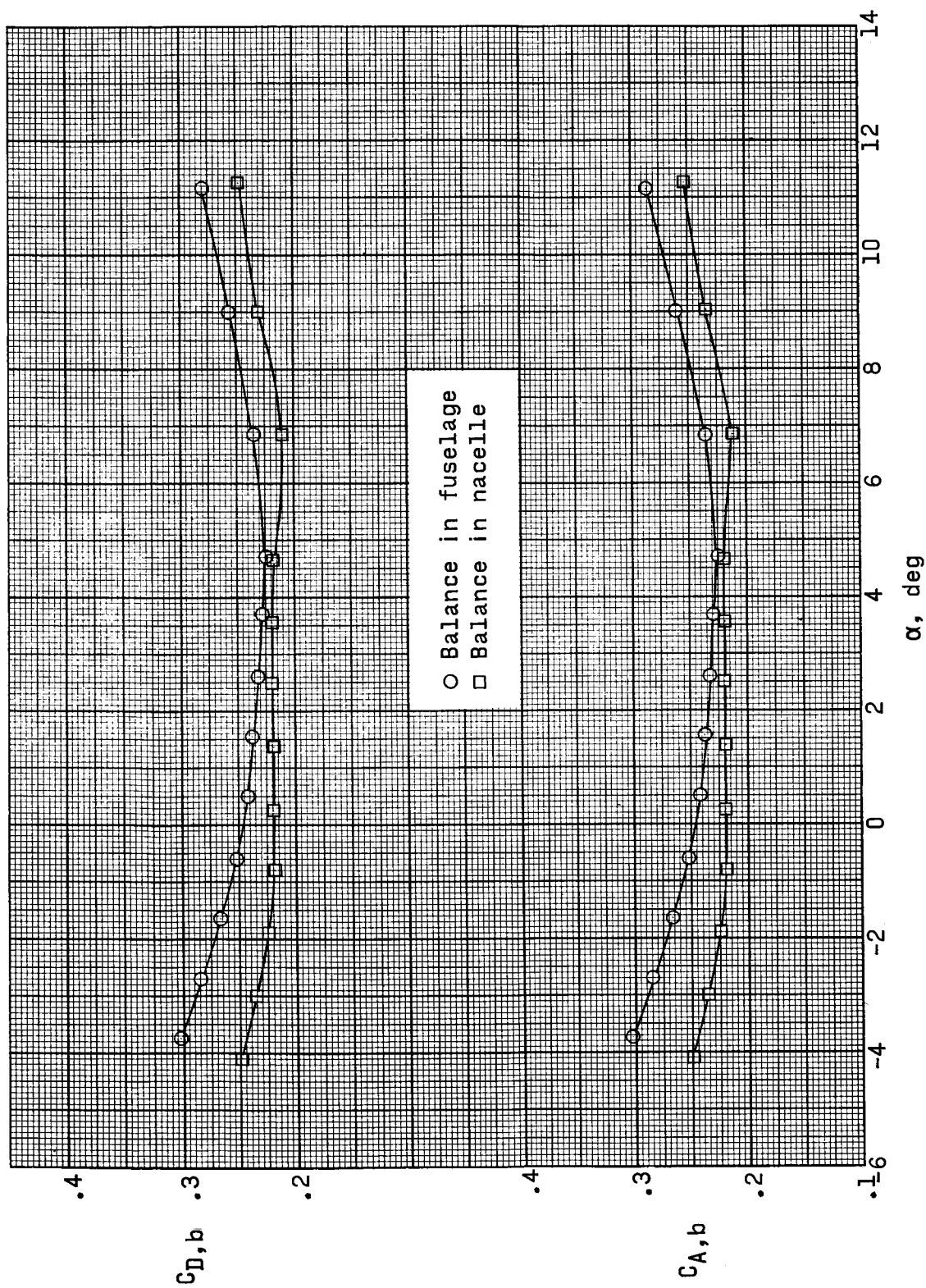
(b) $M = 2.00$.

Figure 3.- Continued.



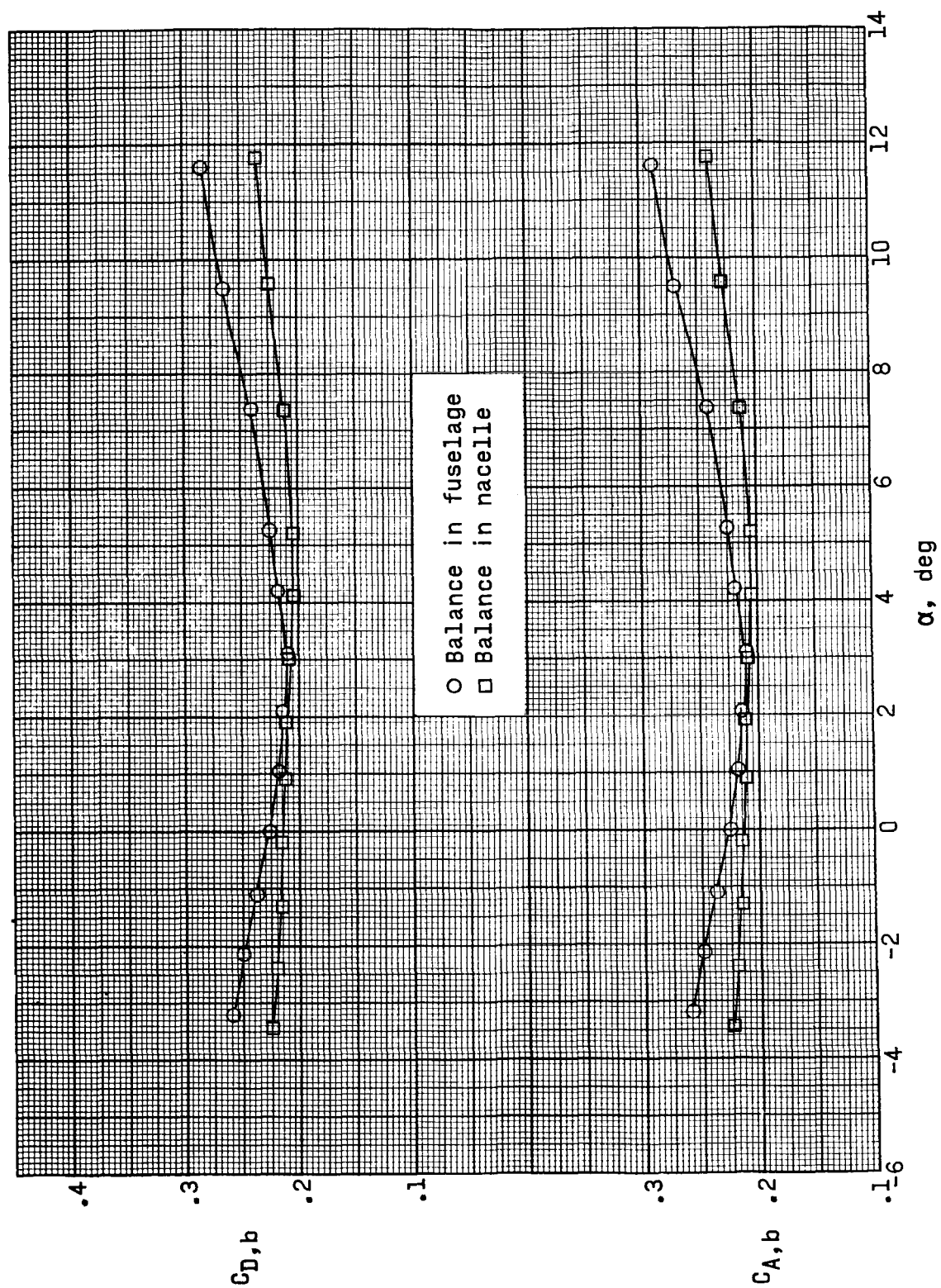
(c) $M = 2.16$.

Figure 3.- Concluded.



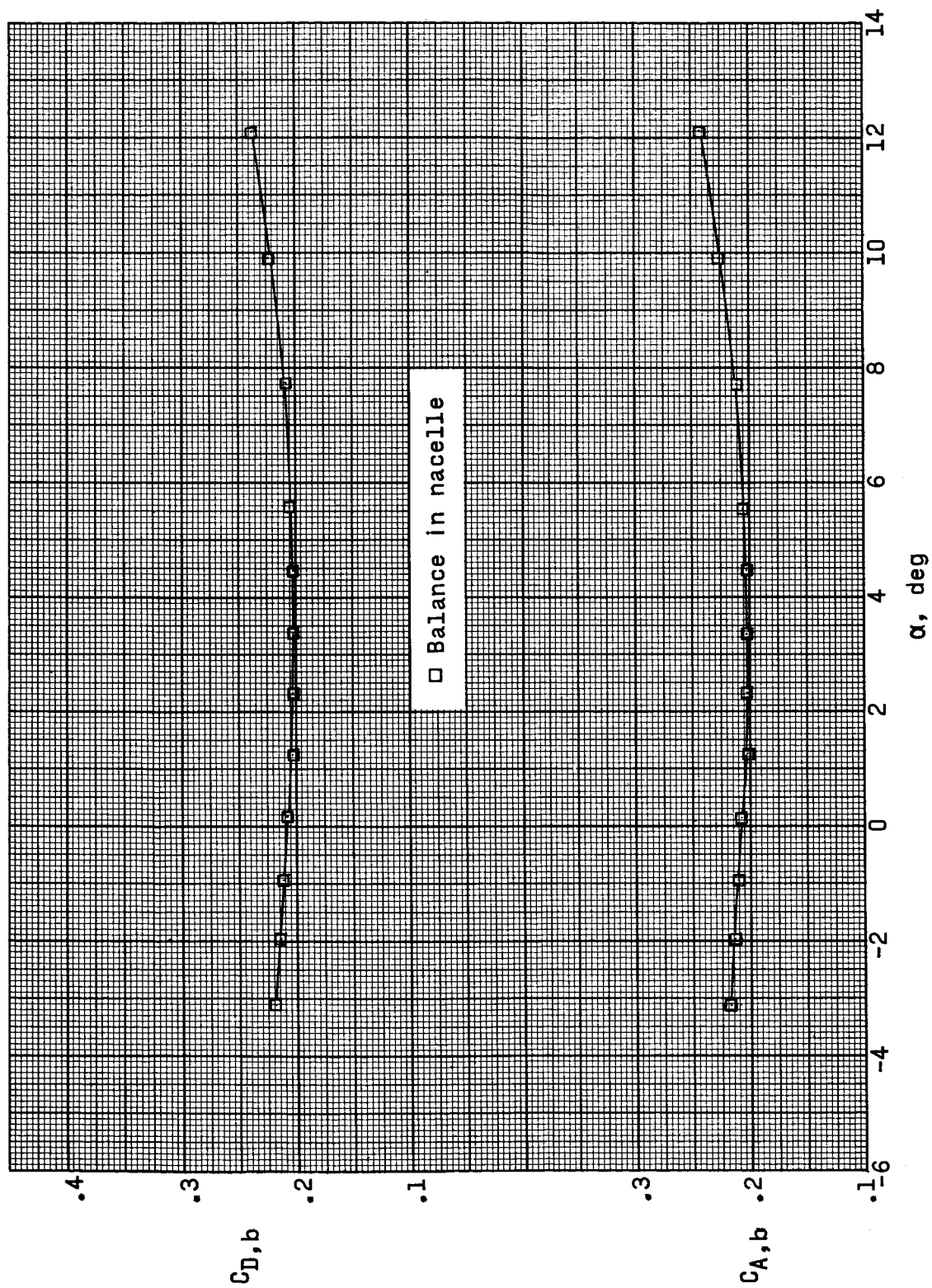
(a) $M = 1.80$.

Figure 4.- Variation of base axial-force and drag coefficients of N_0 nacelle with angle of attack. Afterbody off; $\delta_f = 0^\circ$; $\delta_p = 0^\circ$.



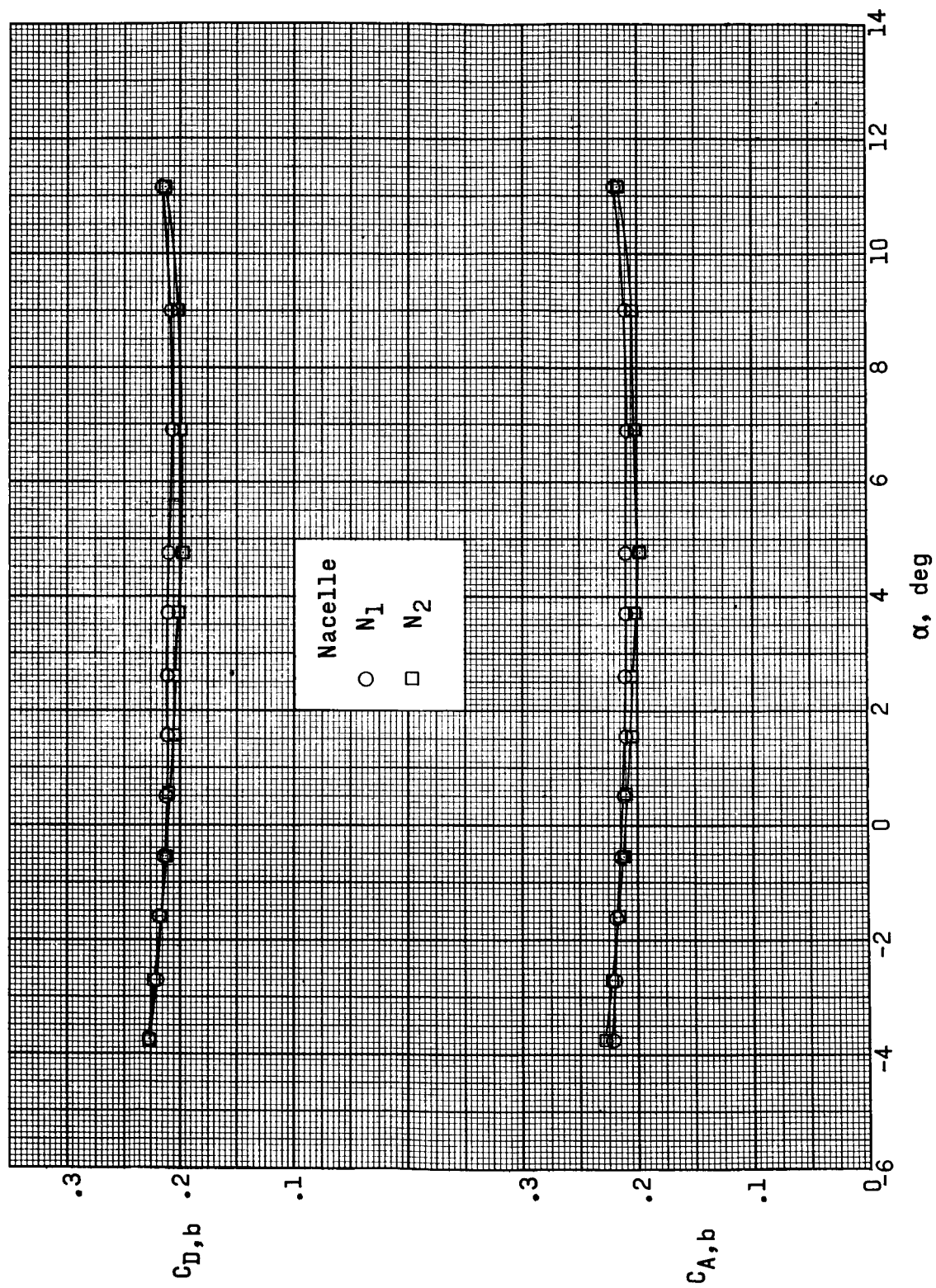
(b) $M = 2.00$.

Figure 4.- Continued.



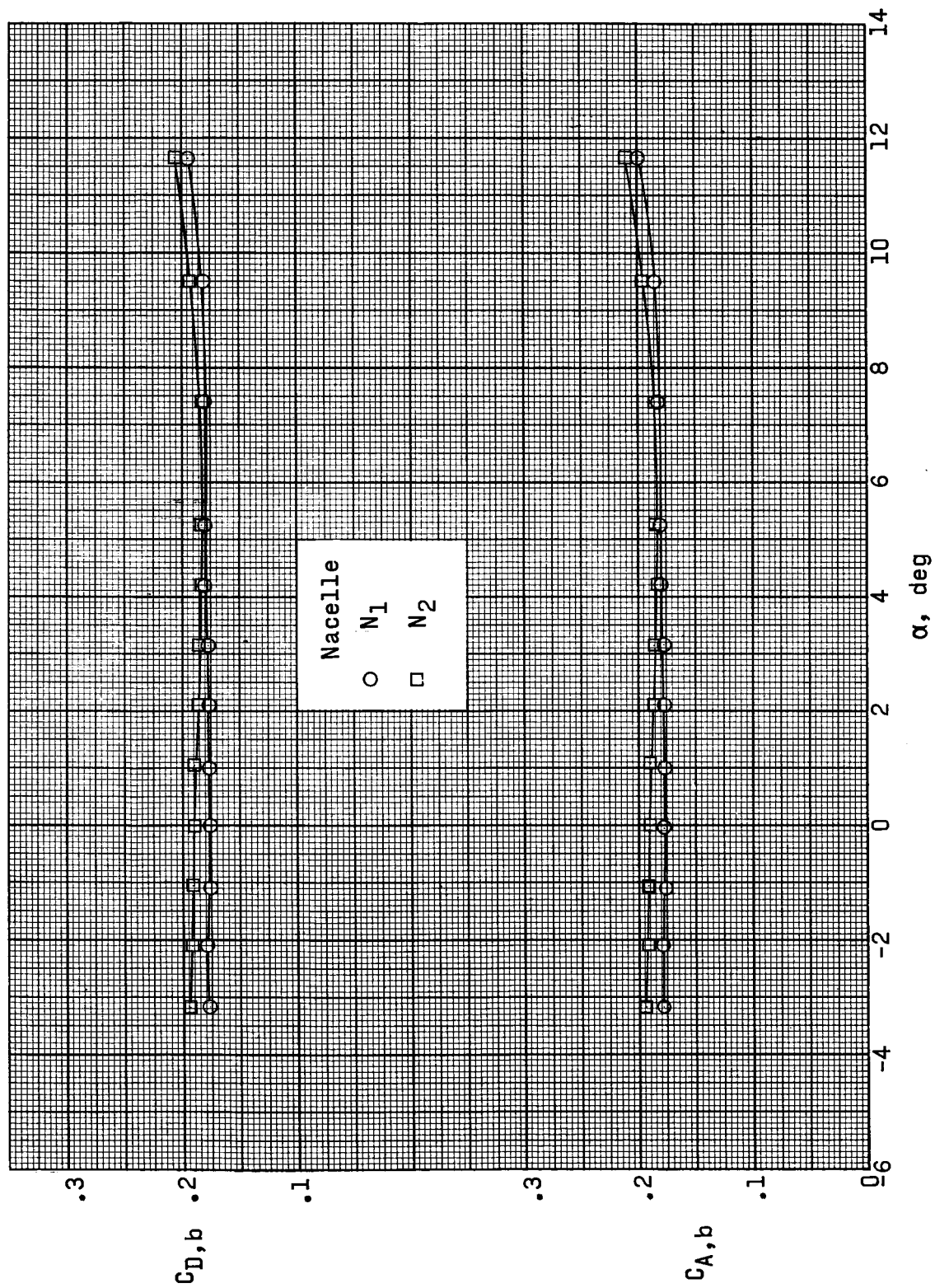
(c) $M = 2.16$.

Figure 4.- Concluded.



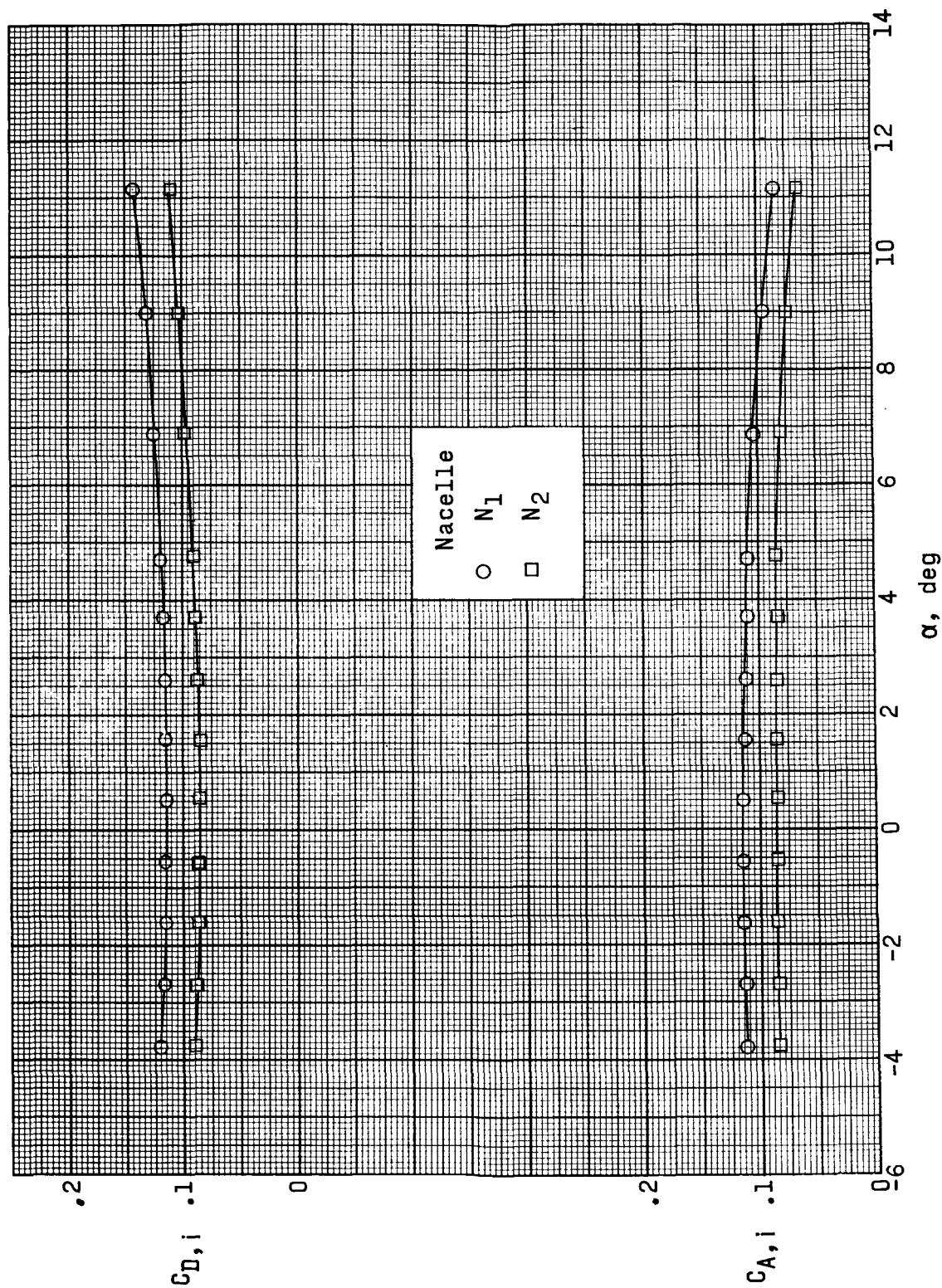
(a) $M = 1.80$.

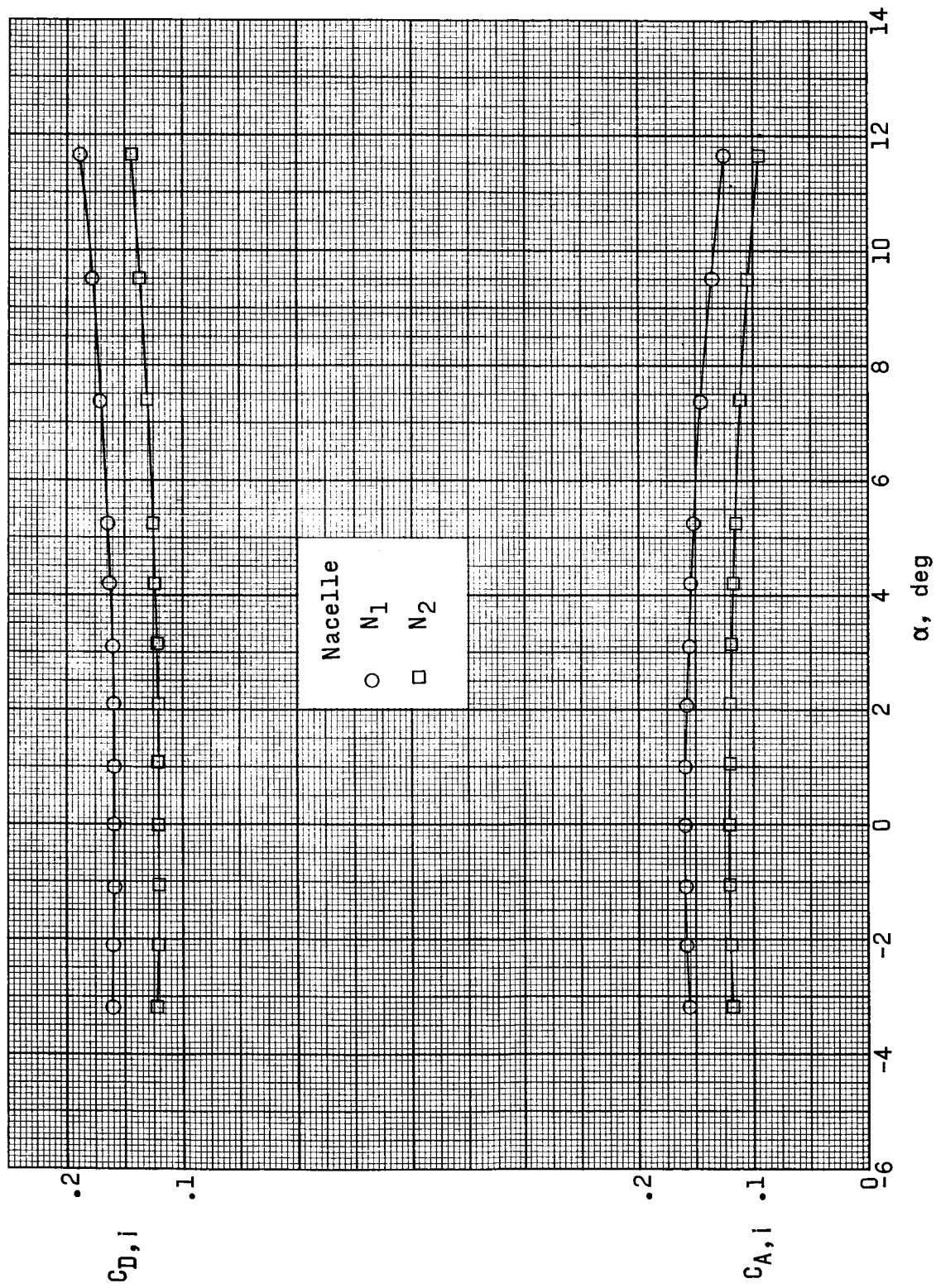
Figure 5.- Variation of base axial-force and drag coefficients of nacelles N_1 and N_2 with angle of attack. Afterbody off; $\delta_T = 0^\circ$; $\delta_p = 0^\circ$.



(b) $M = 2.00$.

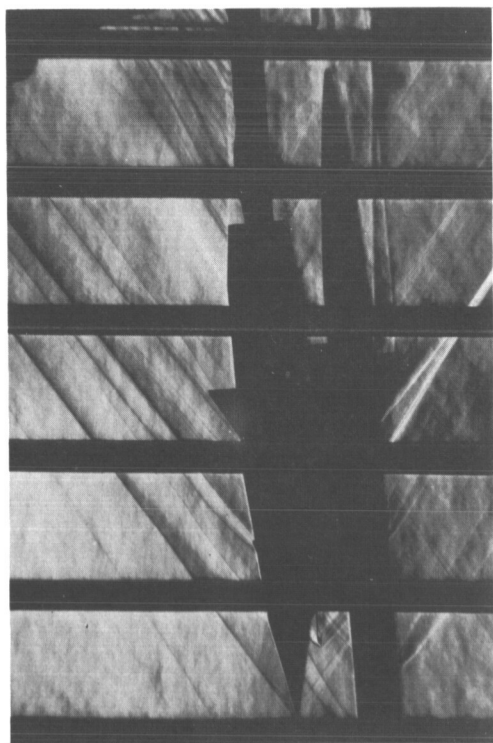
Figure 5.- Concluded.

(a) $M = 1.80$.Figure 6.- Variation of nacelle internal flow axial-force and drag coefficients with angle of attack. Afterbody off; $\delta_f = 0^\circ$; $\delta_p = 0^\circ$.

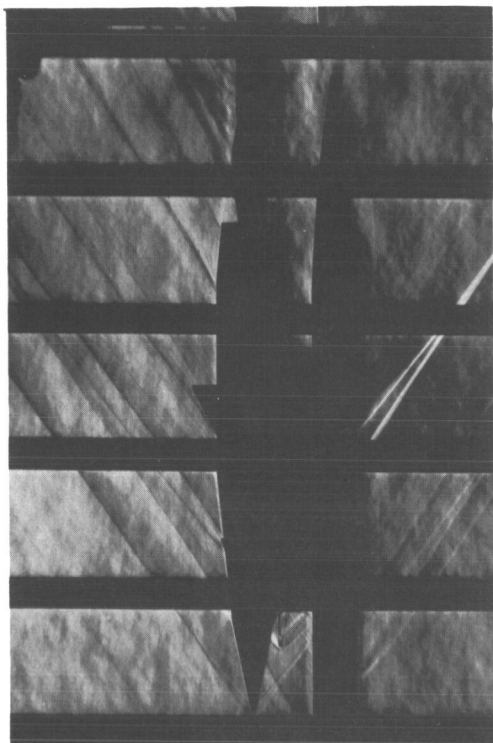


(b) $M = 2.00$.

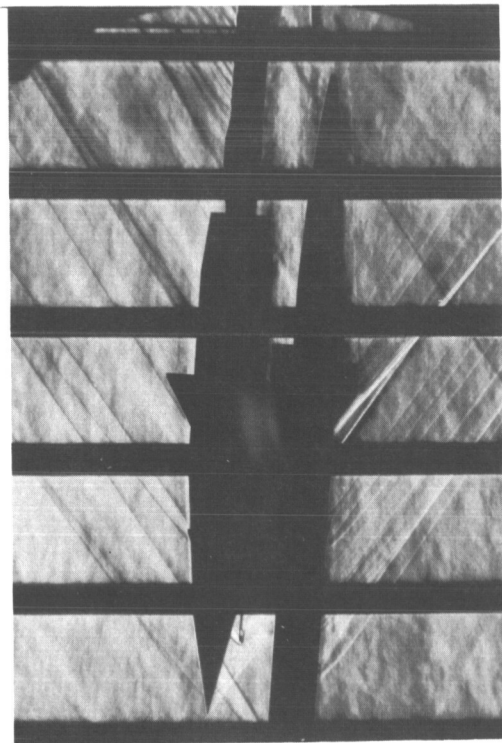
Figure 6.- Concluded.



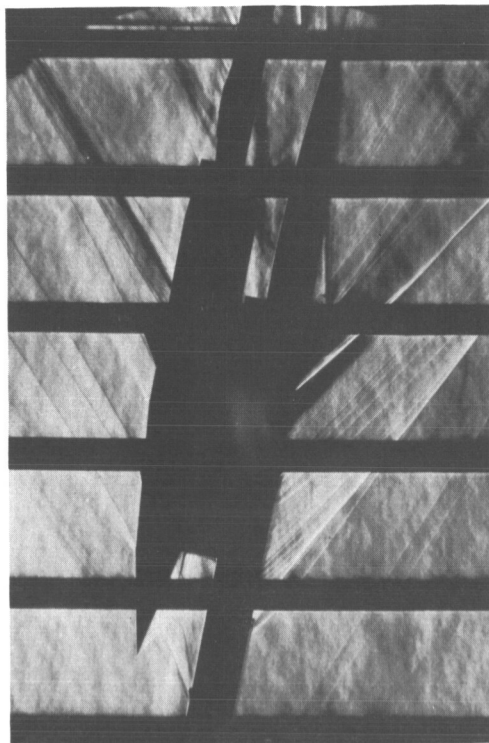
$M = 1.80; \alpha = -4.1^\circ$



$M = 1.80; \alpha = 0.3^\circ$



$M = 1.80; \alpha = 4.6^\circ$

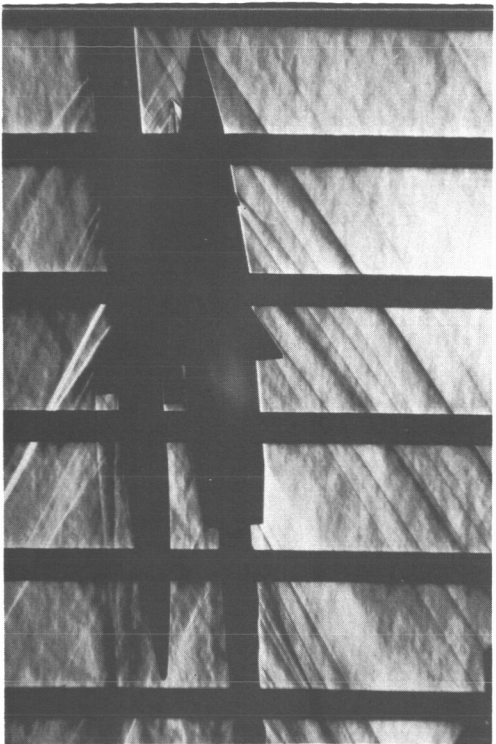


$M = 1.80; \alpha = 11.3^\circ$

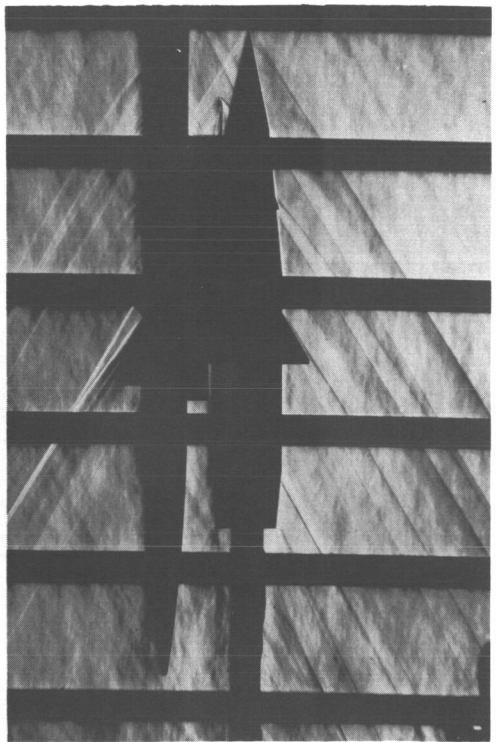
(a) Balance in nacelle with afterbody on. $\delta_f = 0^\circ$; $\delta_p = 0^\circ$.

Figure 7.- Schlieren photographs of model.

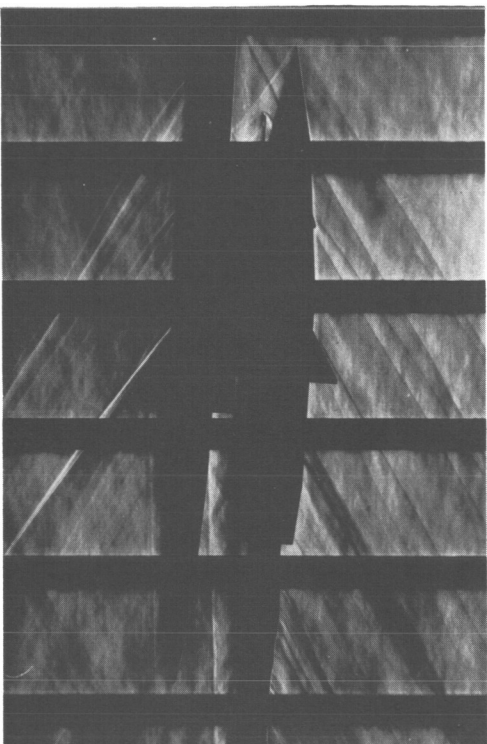
L-66-4529



$M = 2.00; \alpha = -3.5^\circ$



$M = 2.00; \alpha = 0.9^\circ$



$M = 2.00; \alpha = 5.2^\circ$

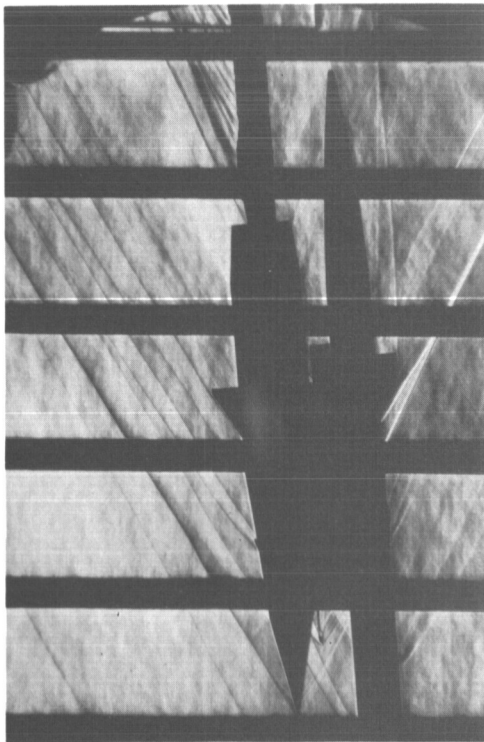


$M = 2.00; \alpha = 11.8^\circ$

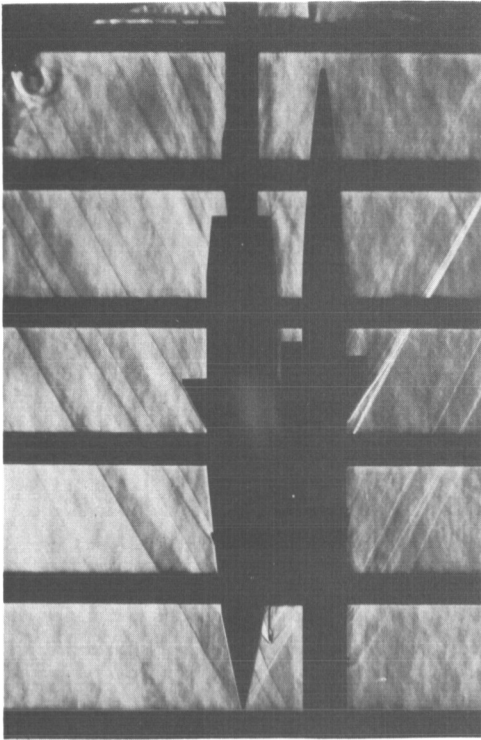
(a) Continued.

Figure 7.- Continued.

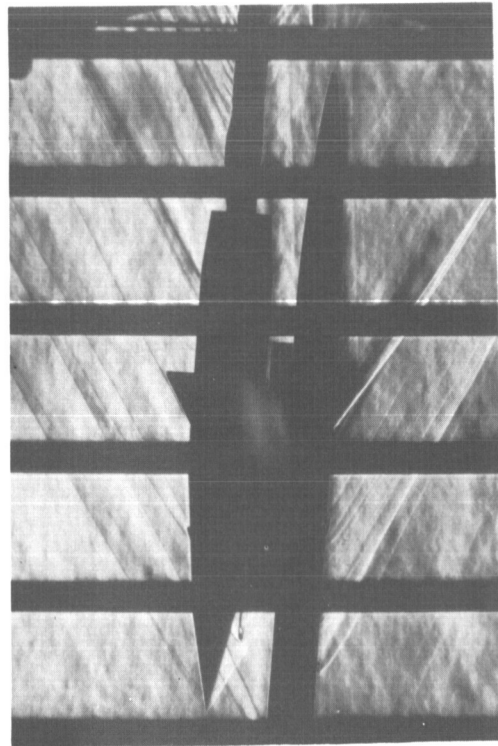
L-66-4530



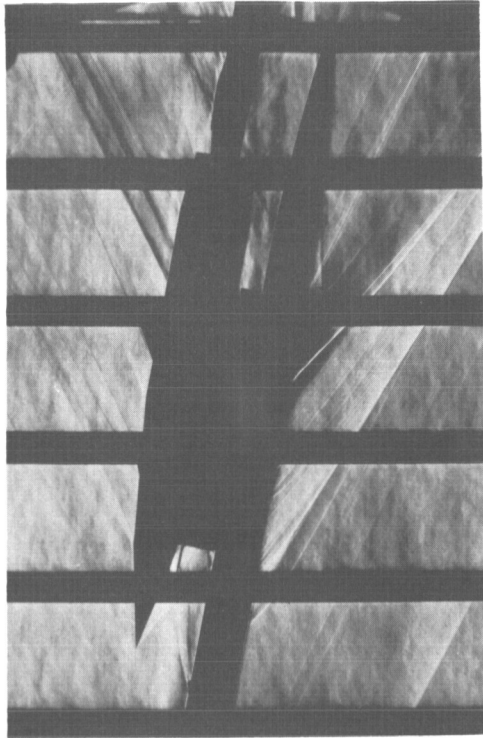
$M = 2.16; \alpha = -3.1^\circ$



$M = 2.16; \alpha = 1.2^\circ$



$M = 2.16; \alpha = 5.6^\circ$

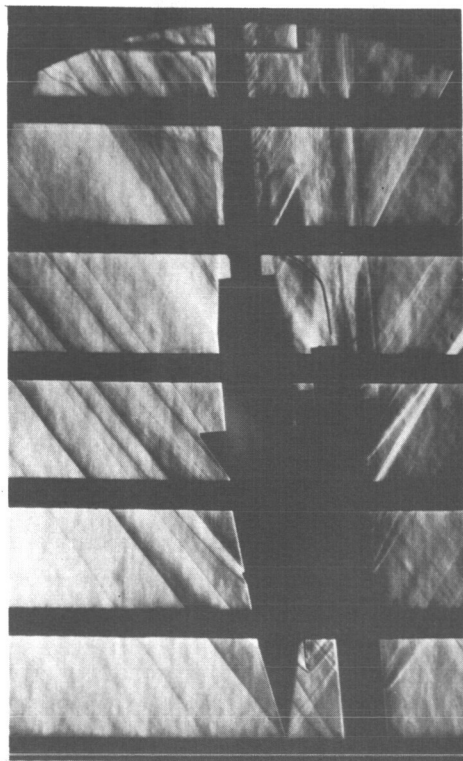


$M = 2.16; \alpha = 12.1^\circ$

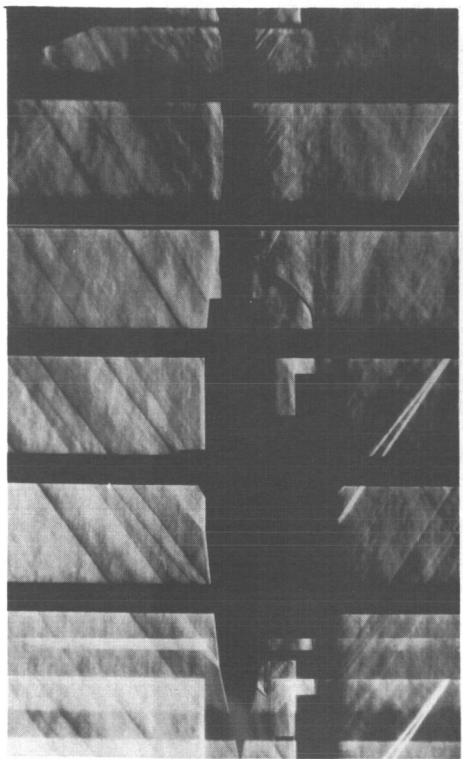
(a) Concluded.

Figure 7.- Continued.

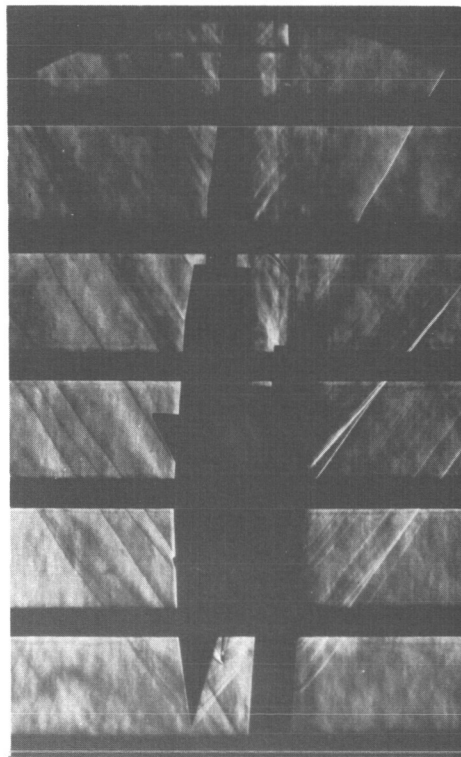
L-66-4531



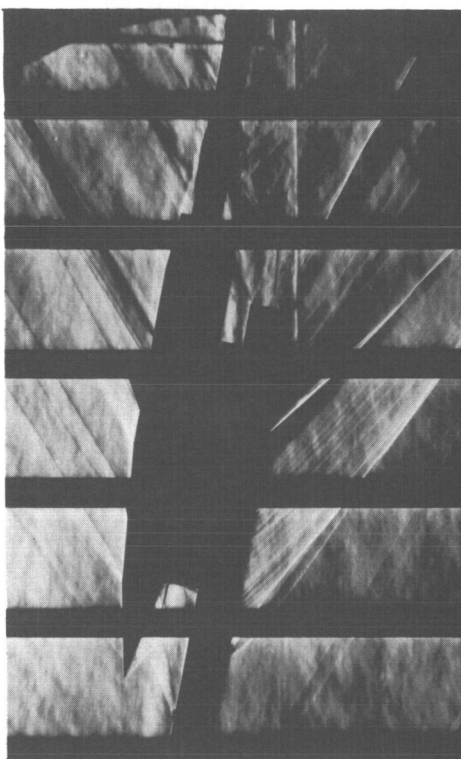
$M = 1.80; \alpha = -4.1^\circ$



$M = 1.80; \alpha = 0.3^\circ$



$M = 1.80; \alpha = 4.7^\circ$

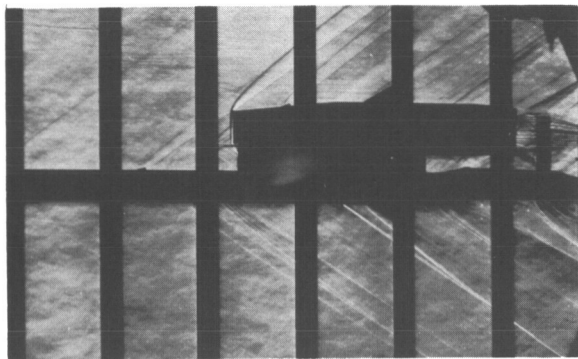


$M = 1.80; \alpha = 11.3^\circ$

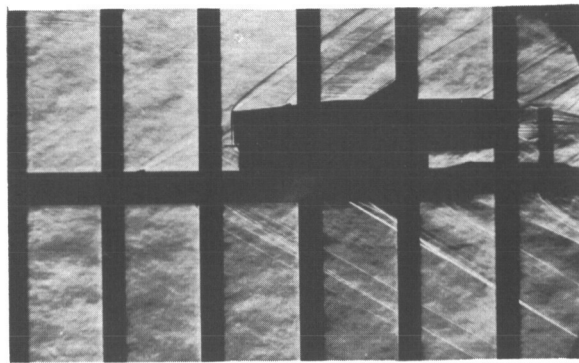
(b) Balance in nacelle with afterbody off. $\delta_F = 0^\circ; \delta_P = 0^\circ$.

Figure 7.- Continued.

L-66-4532

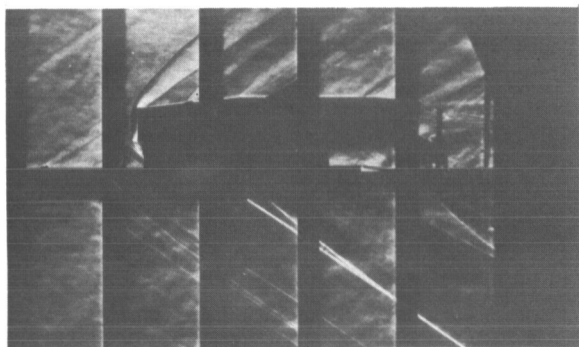


$M = 1.80; \alpha = 0.5^\circ$

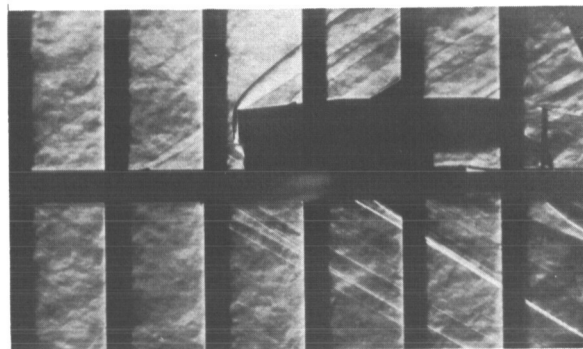


$M = 2.00; \alpha = 1.0^\circ$

N_1 nacelle with rake attached

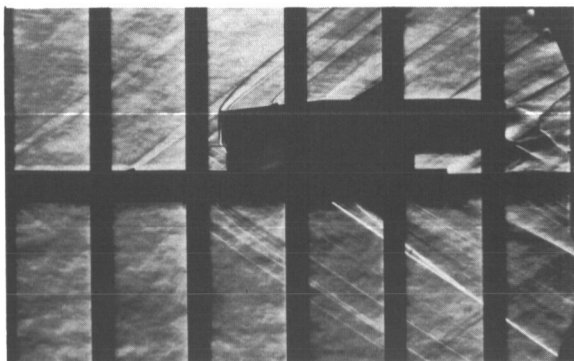


$M = 1.80; \alpha = 0.5^\circ$

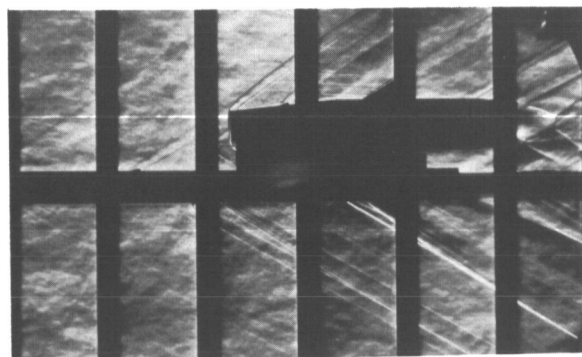


$M = 2.00; \alpha = 1.0^\circ$

N_2 nacelle with rake attached



$M = 1.80; \alpha = 0.5^\circ$



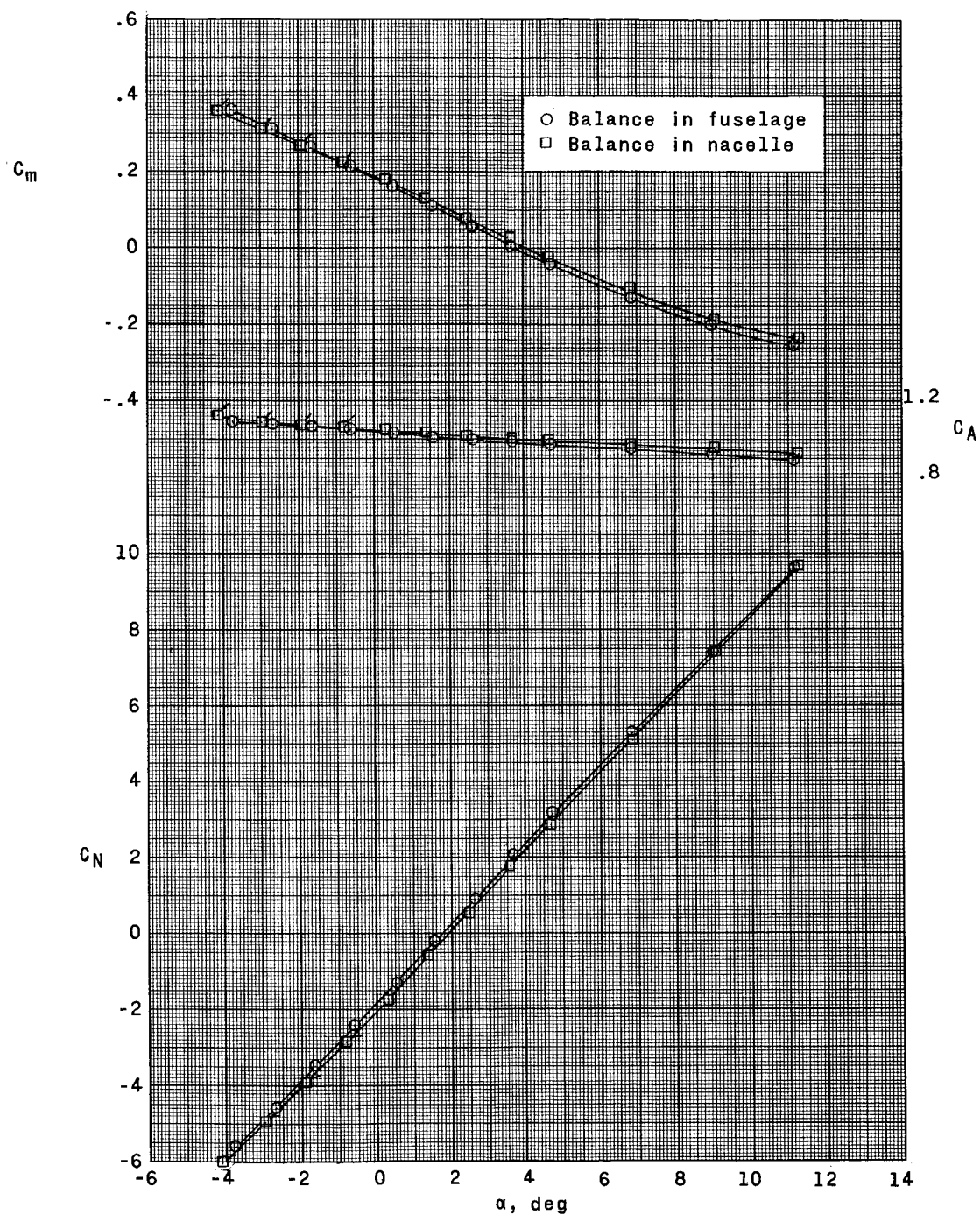
$M = 2.00; \alpha = 1.0^\circ$

N_1 nacelle with rake removed

(c) Balance in fuselage with afterbody off. $\delta_f = 0^\circ; \delta_p = 0^\circ$.

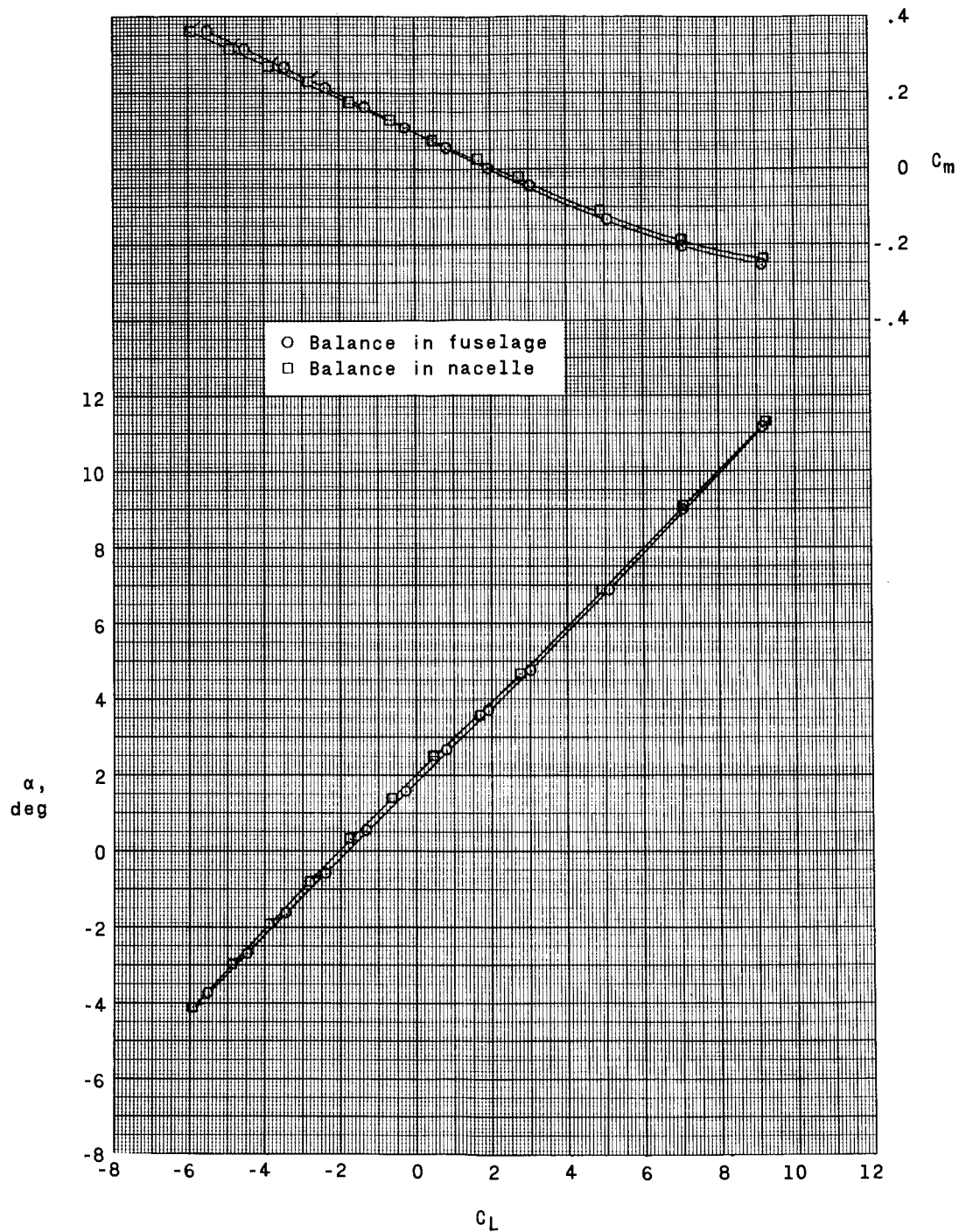
L-66-4533

Figure 7.- Concluded.



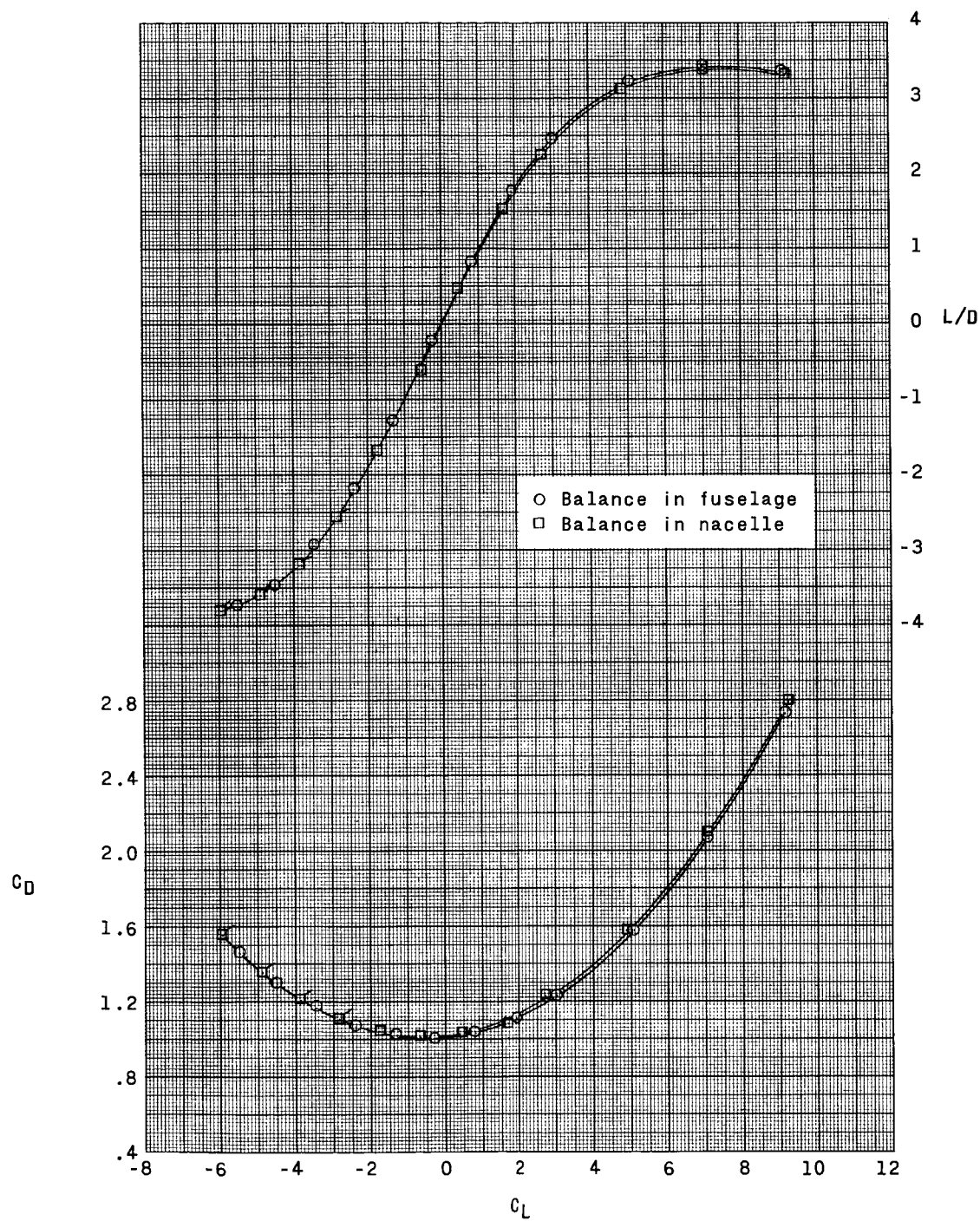
(a) $M = 1.80$; $\beta = 0^\circ$.

Figure 8.- Effect of balance-sting location on aerodynamic characteristics of identical configurations. Afterbody off; conical fairing over nacelle inlet; $\delta_f = 0^\circ$; $\delta_p = 0^\circ$.



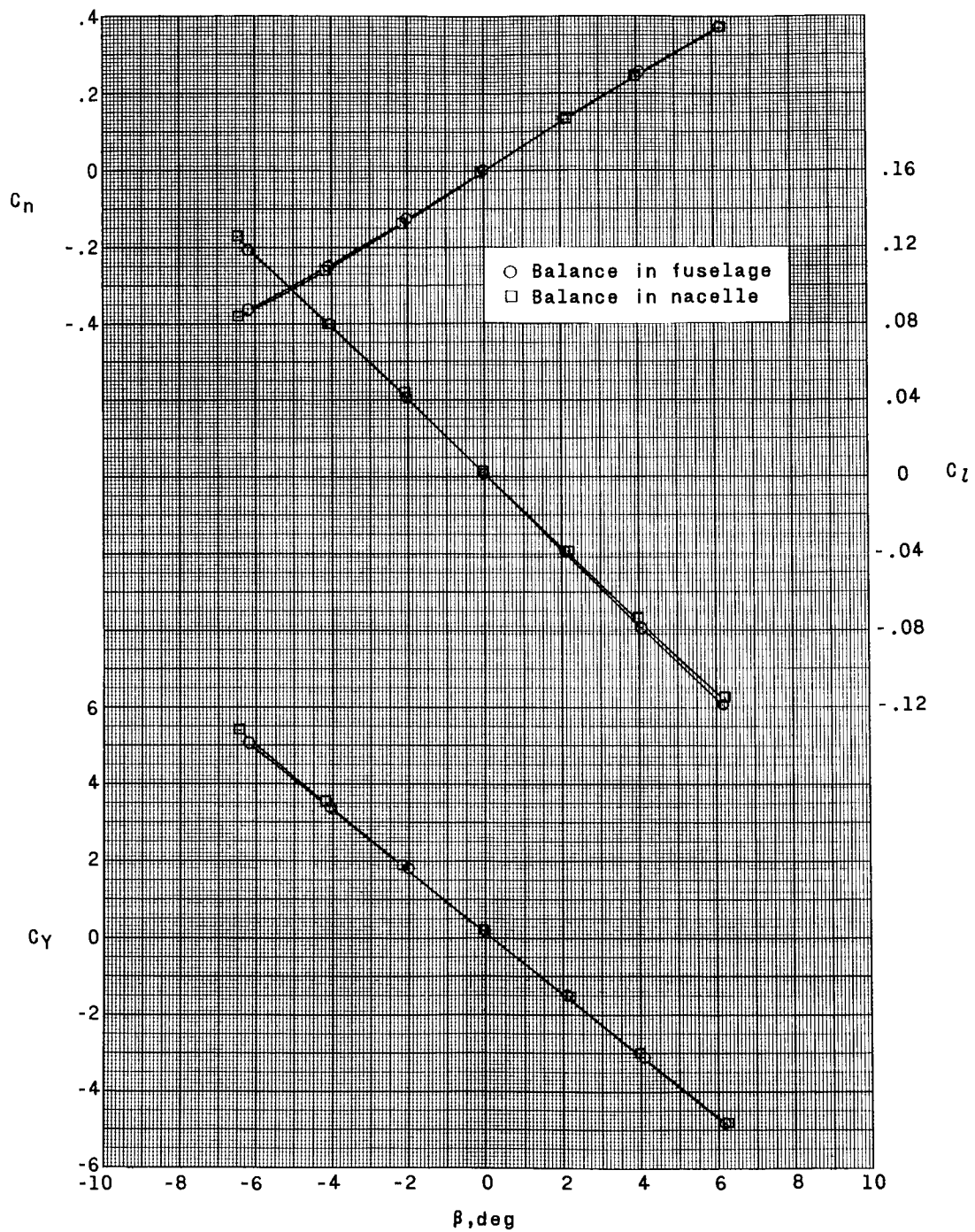
(a) Continued.

Figure 8.- Continued.



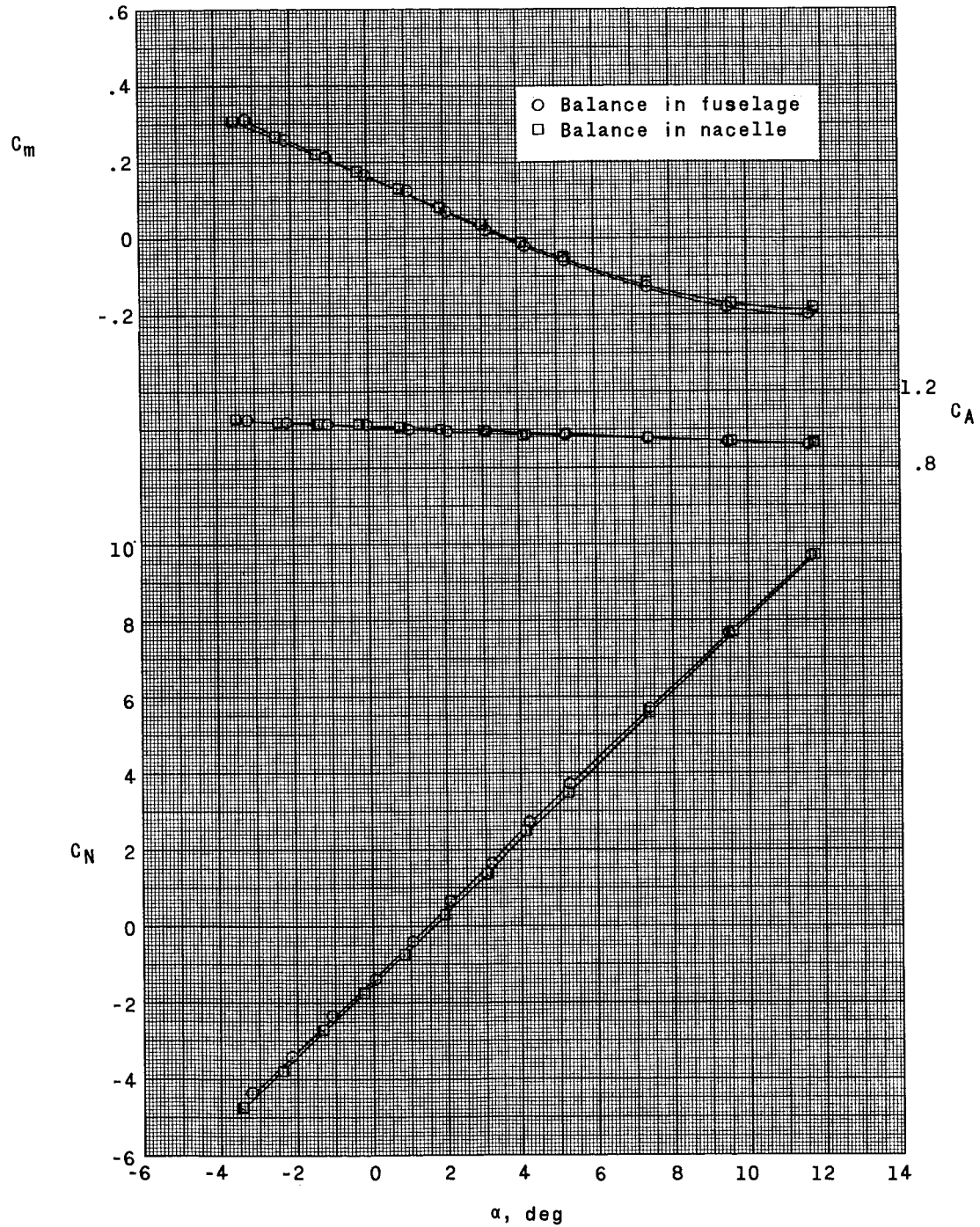
(a) Continued.

Figure 8.- Continued.



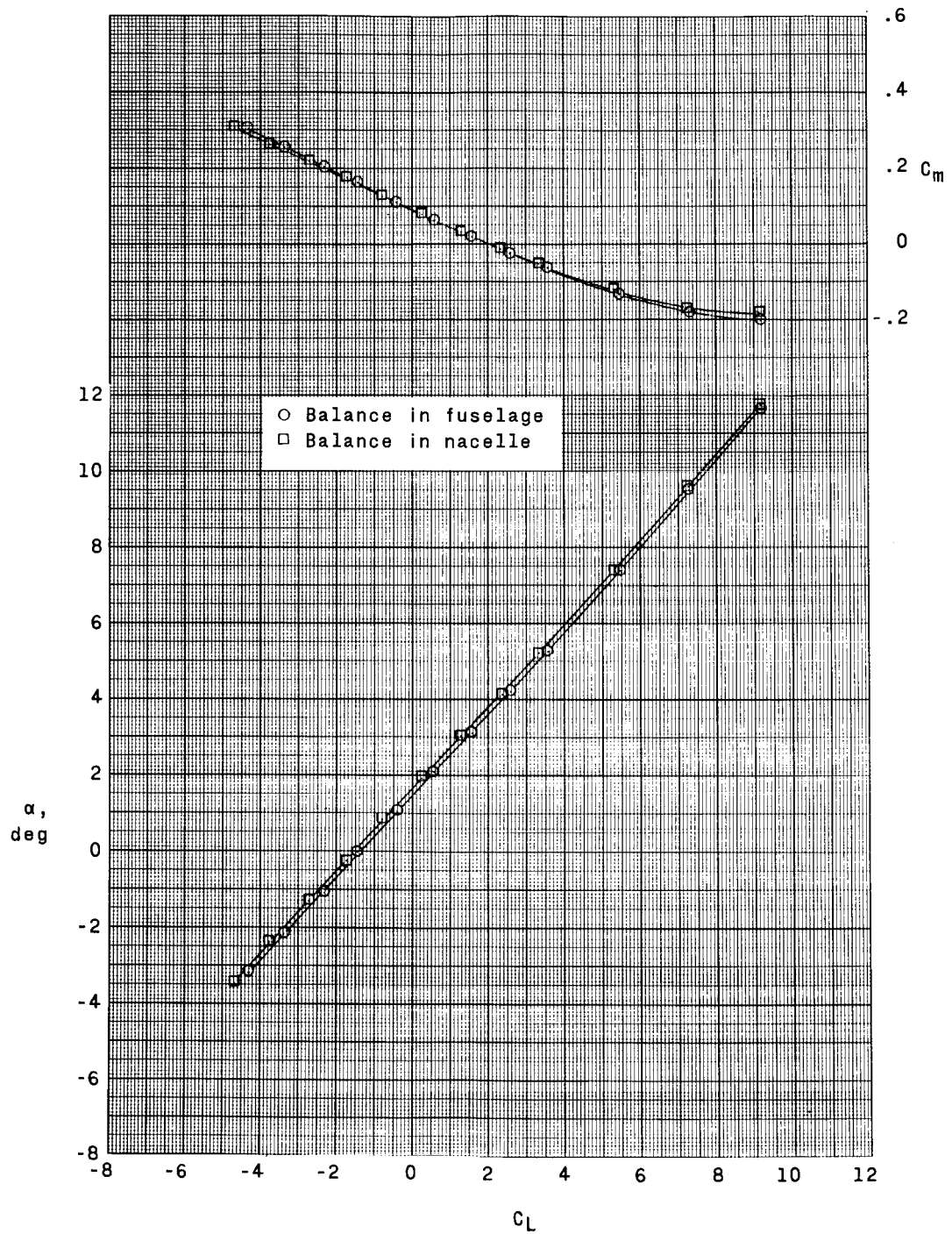
(a) Concluded.

Figure 8.- Continued.



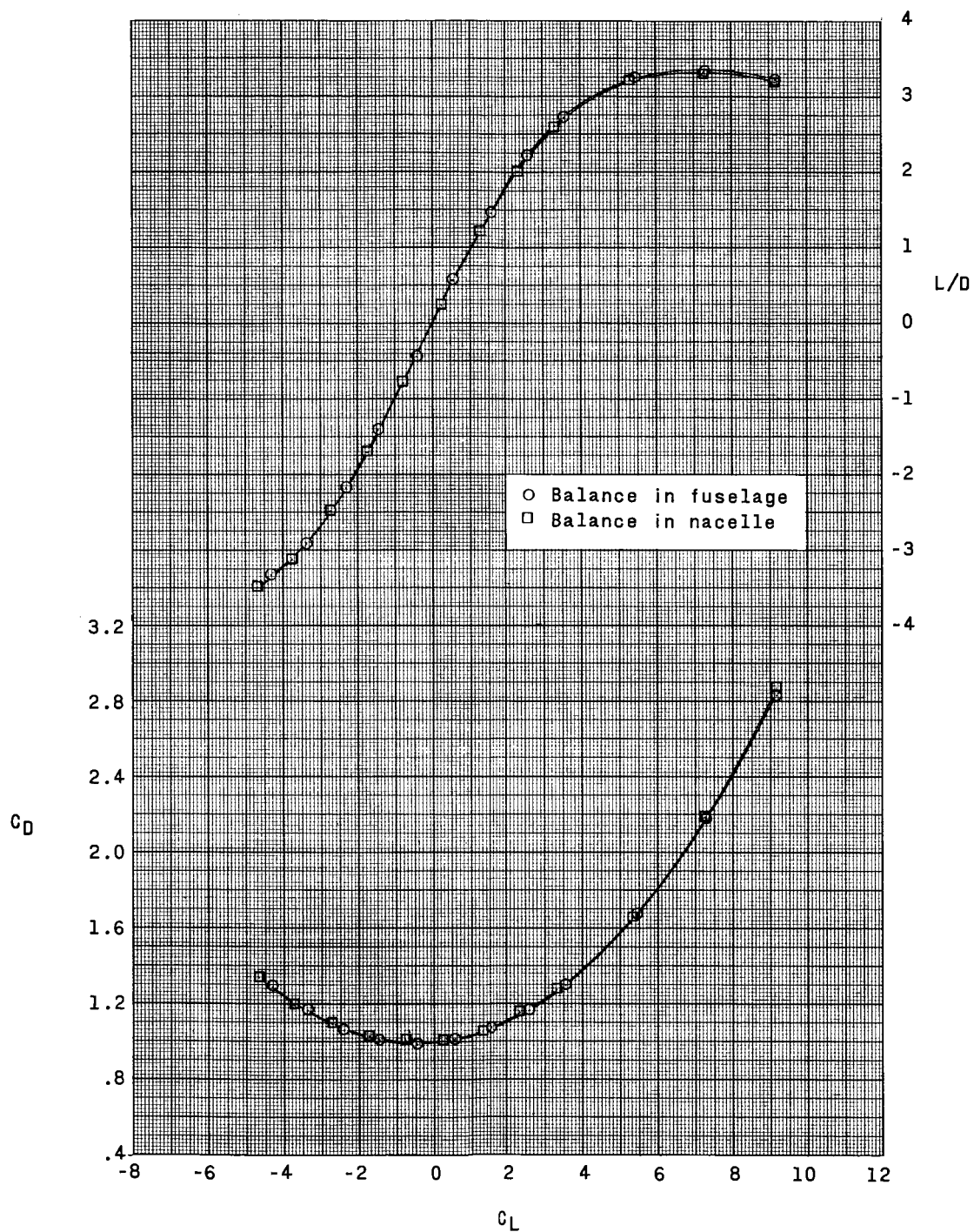
(b) $M = 2.00$; $\beta = 0^\circ$.

Figure 8.- Continued.



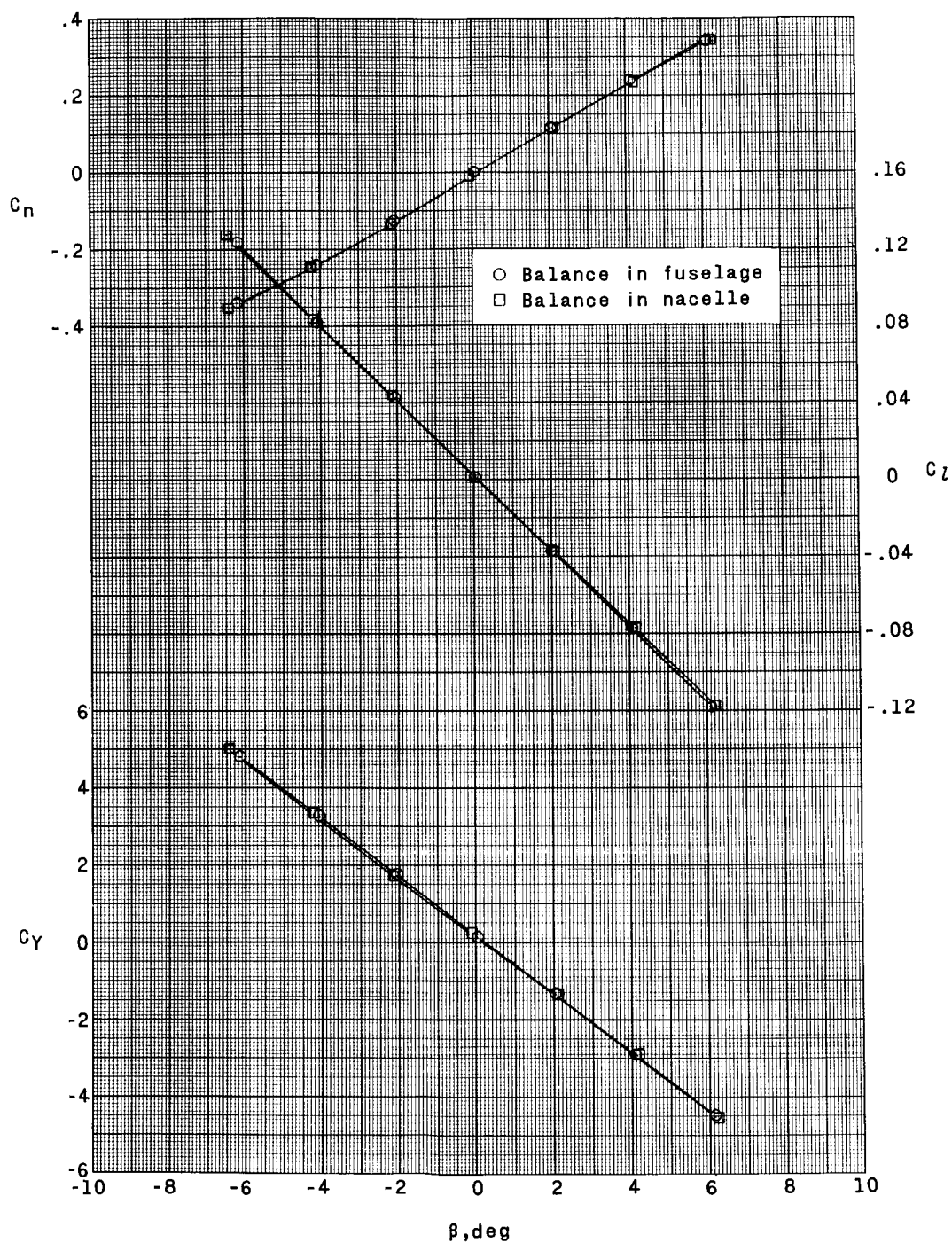
(b) Continued.

Figure 8.- Continued.



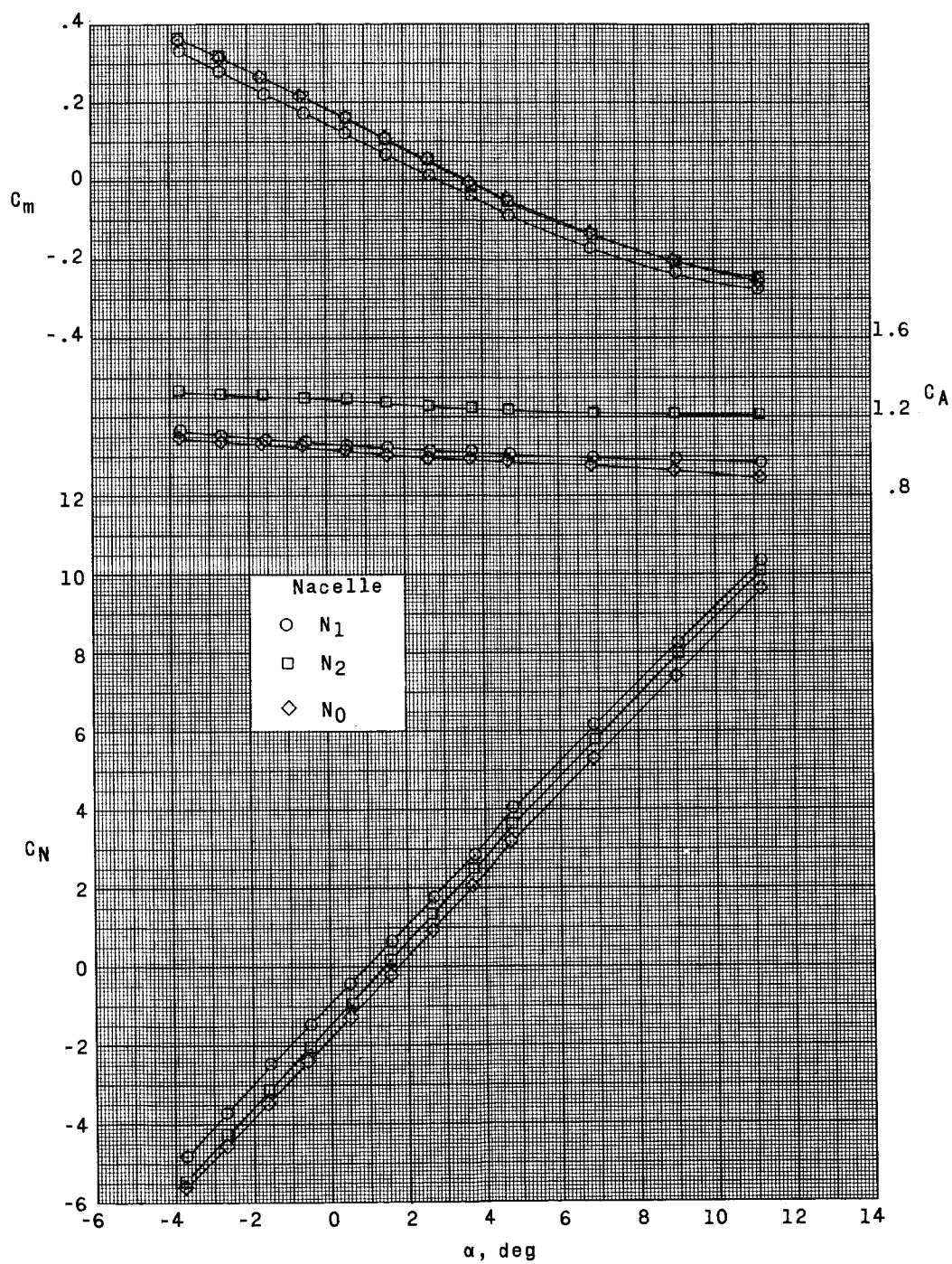
(b) Continued.

Figure 8.- Continued.



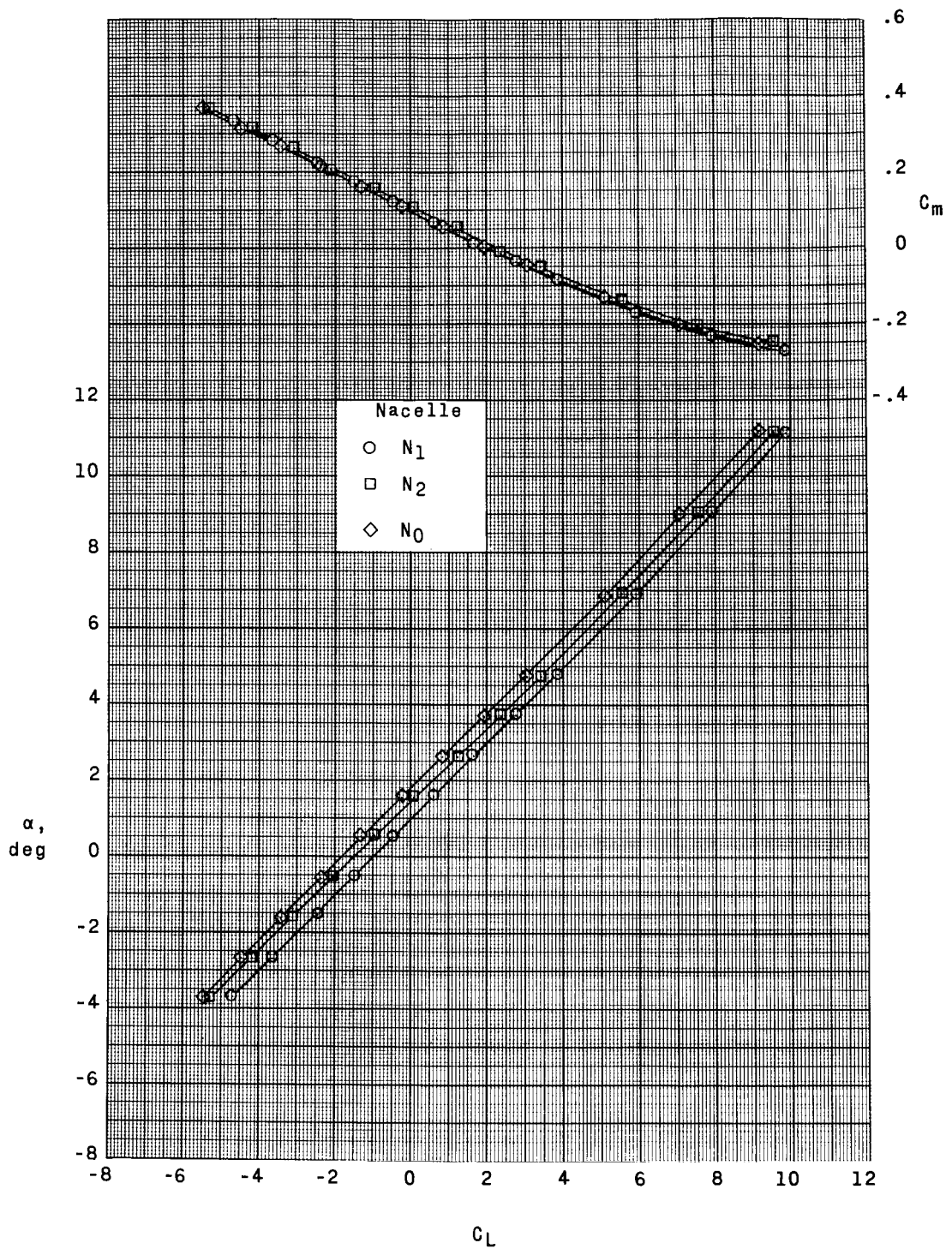
(b) Concluded.

Figure 8.- Concluded.



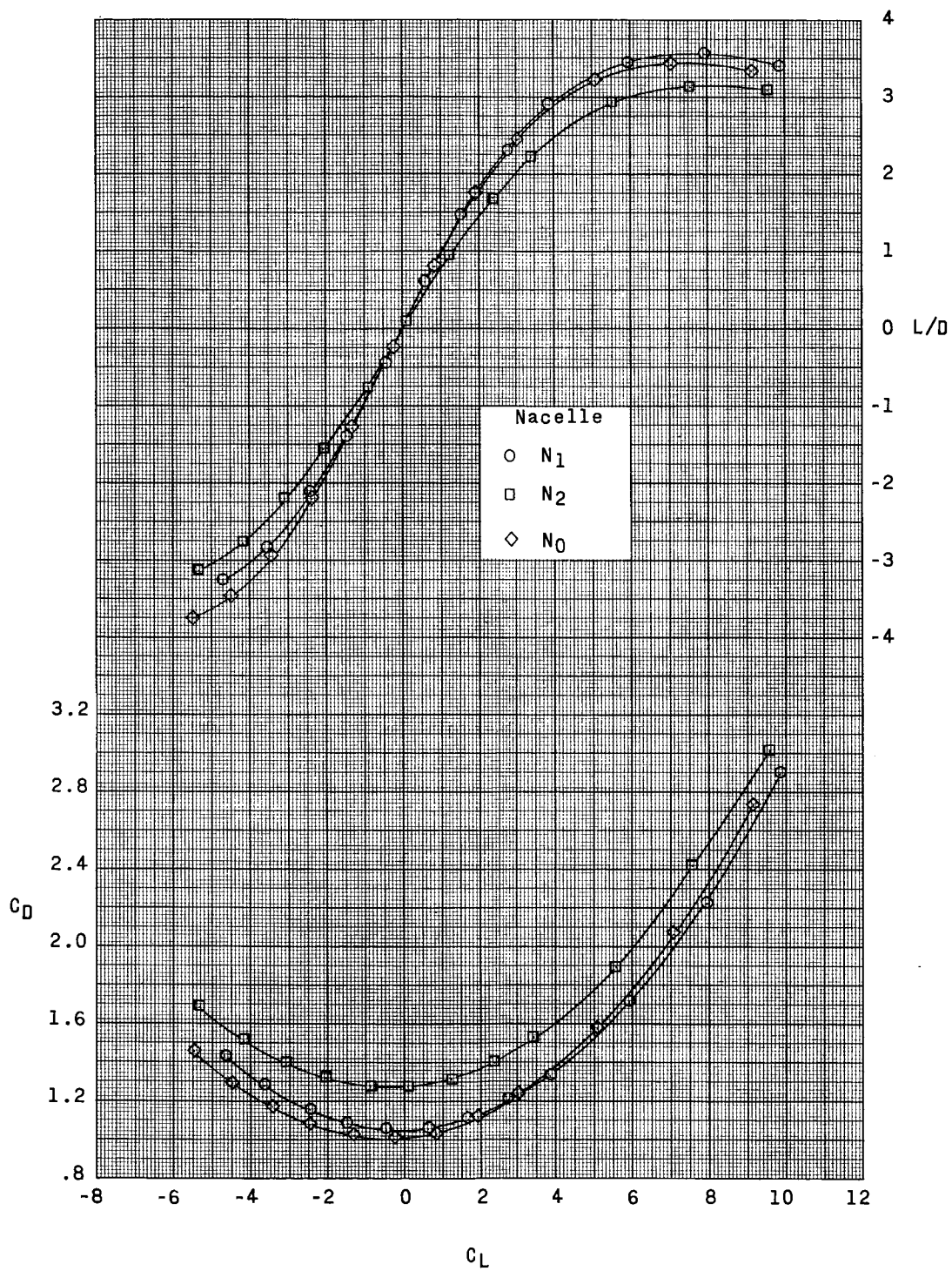
(a) $M = 1.80$.

Figure 9.- Effect of mass-flow ratio of nacelles on longitudinal aerodynamic characteristics. Balance in fuselage; $\delta_F = 0^\circ$; $\delta_p = 0^\circ$.



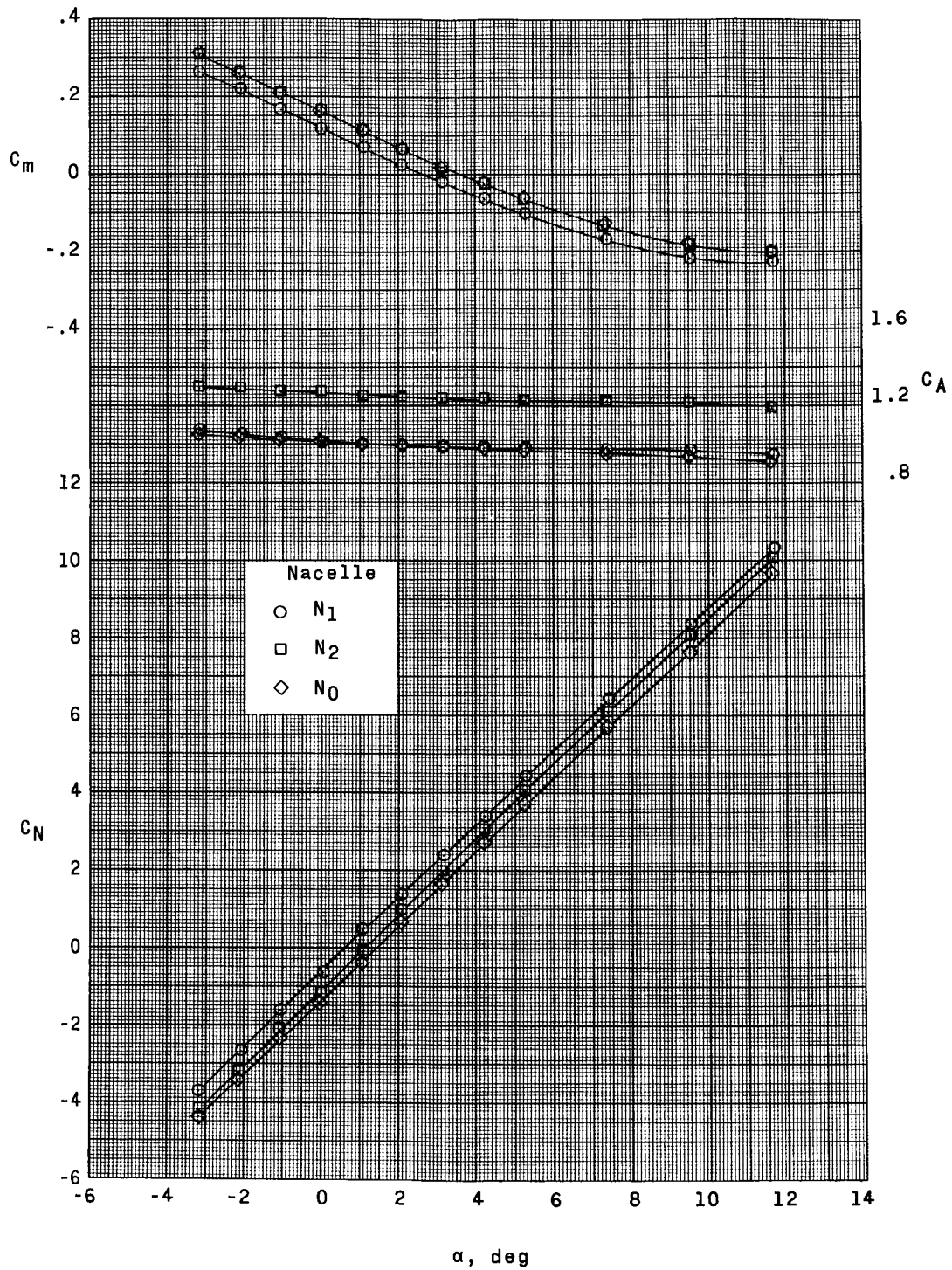
(a) Continued.

Figure 9.- Continued.



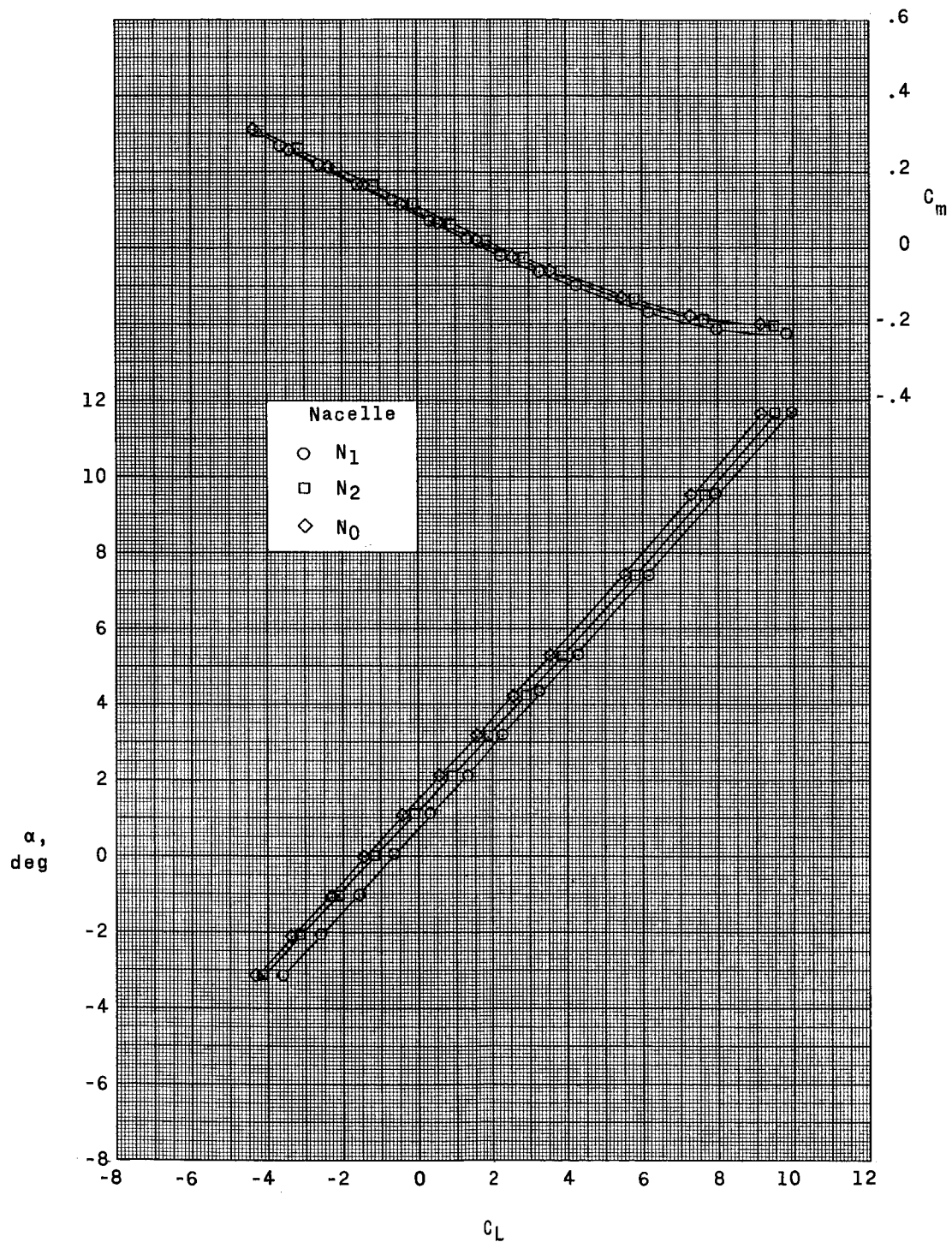
(a) Concluded.

Figure 9.- Continued.



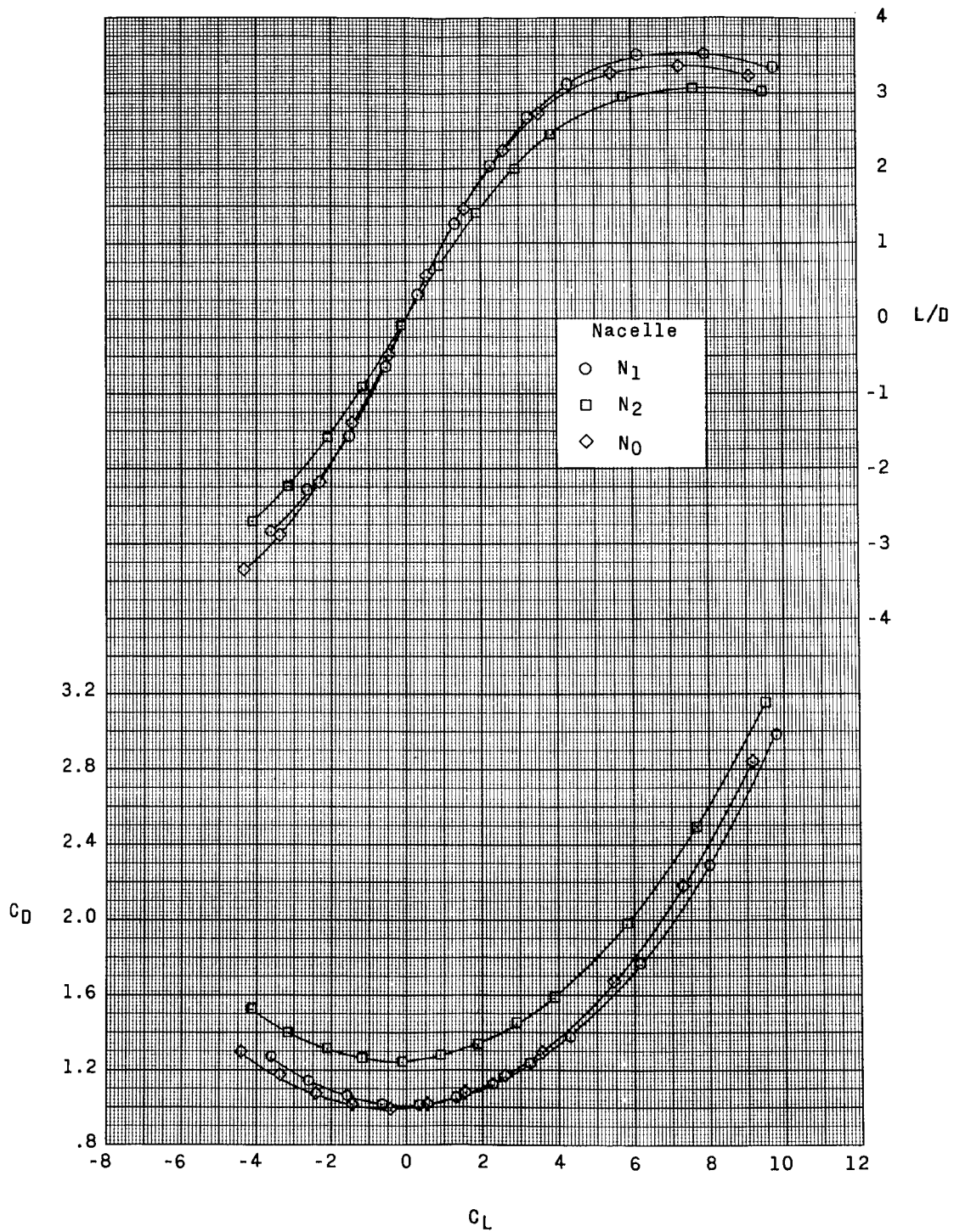
(b) $M = 2.00$.

Figure 9.- Continued.



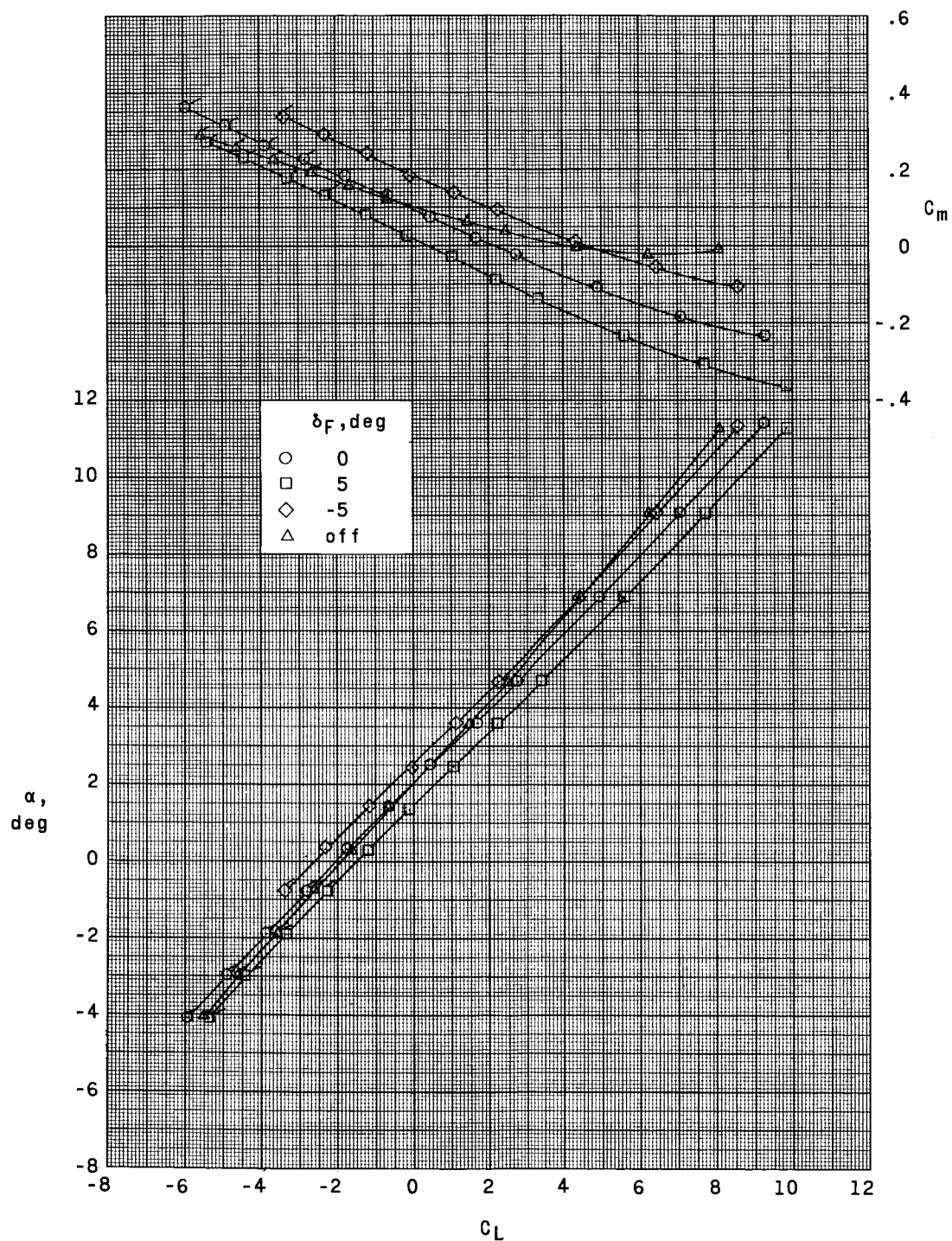
(b) Continued.

Figure 9.- Continued.



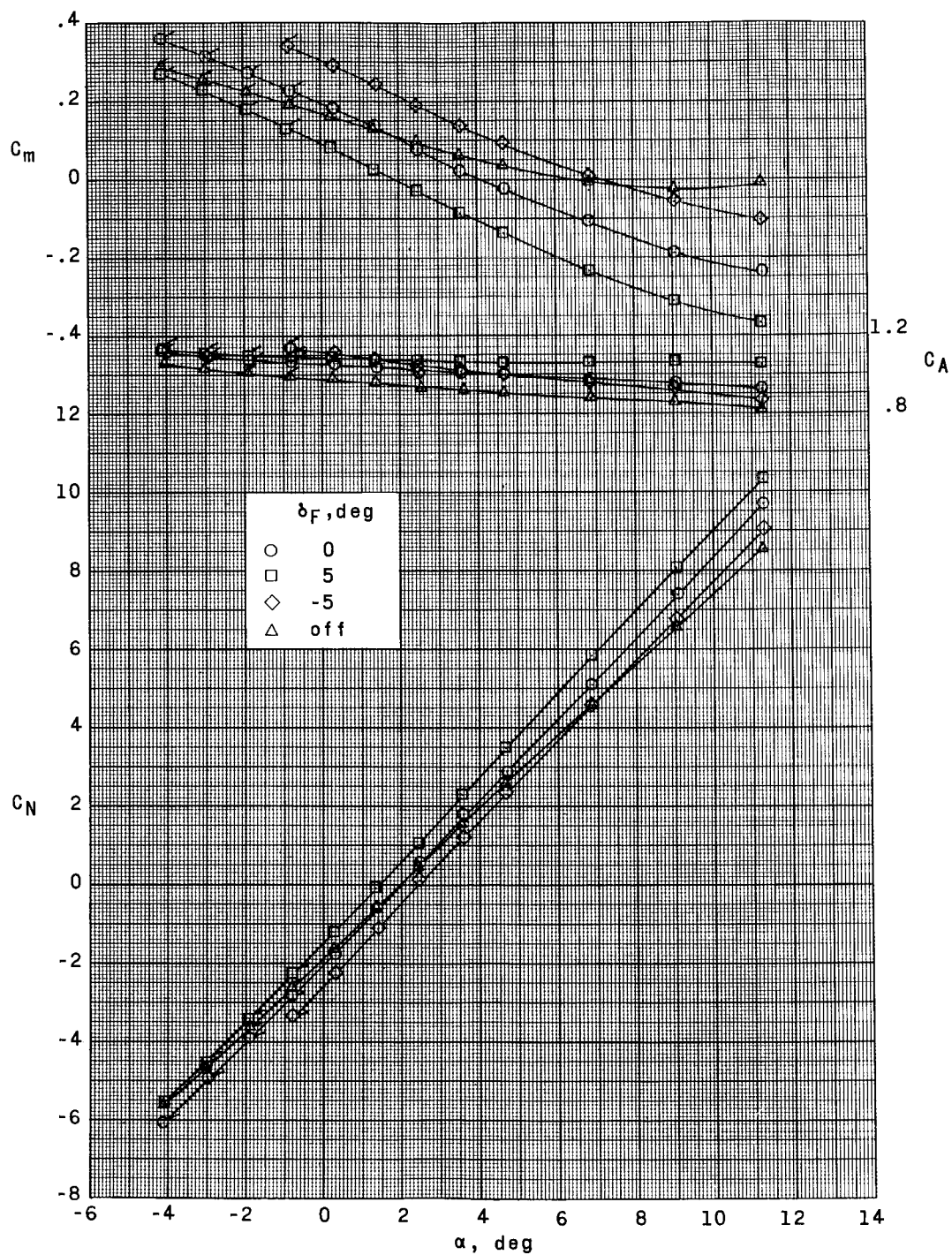
(b) Concluded.

Figure 9.- Concluded.



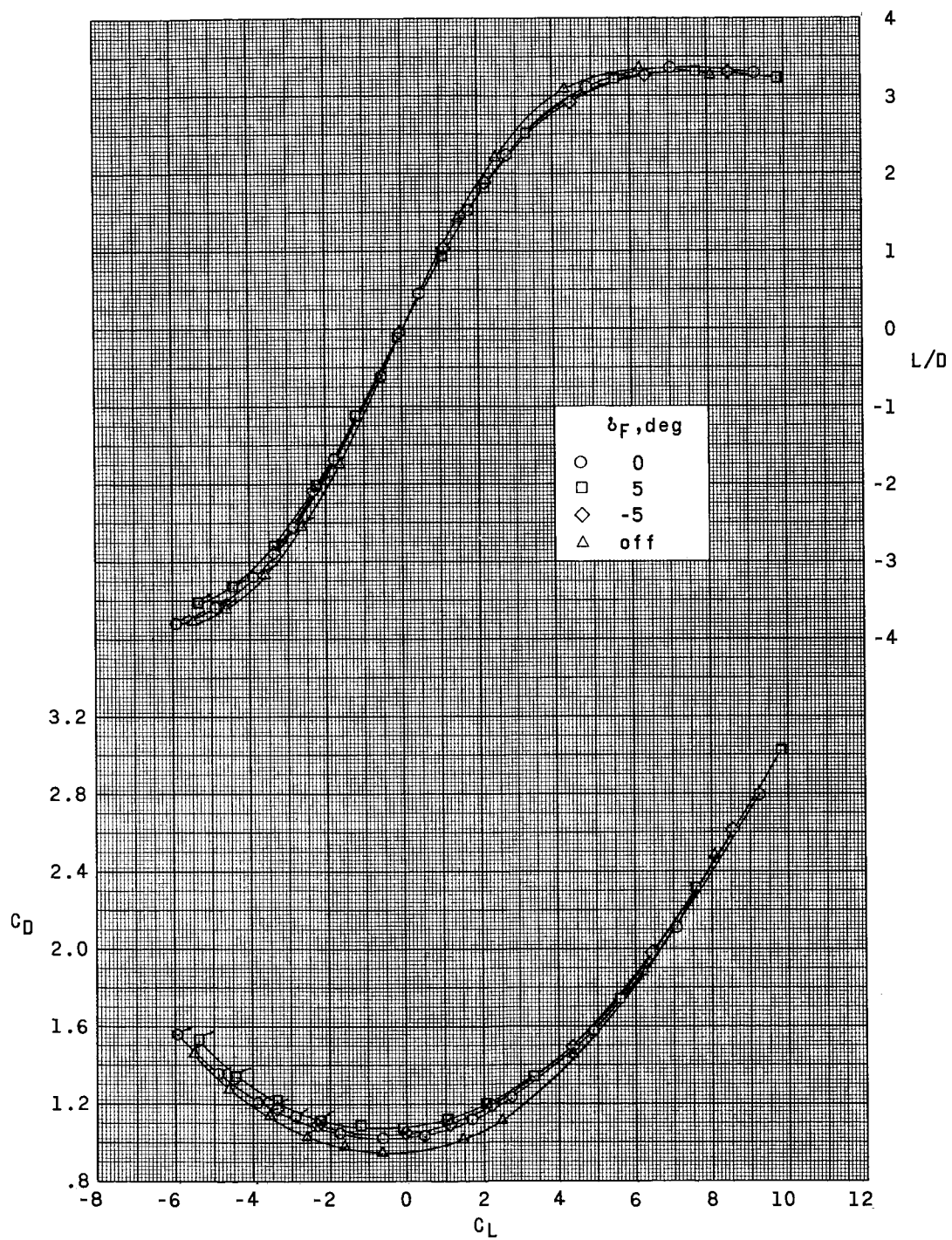
(a) $M = 1.80$.

Figure 10.- Effect of tail fins and tail-fin deflections on longitudinal aerodynamic characteristics. Balance in nacelle; afterbody off; $\delta_p = 0^\circ$. (Flagged symbols denote shock impingement on model.)



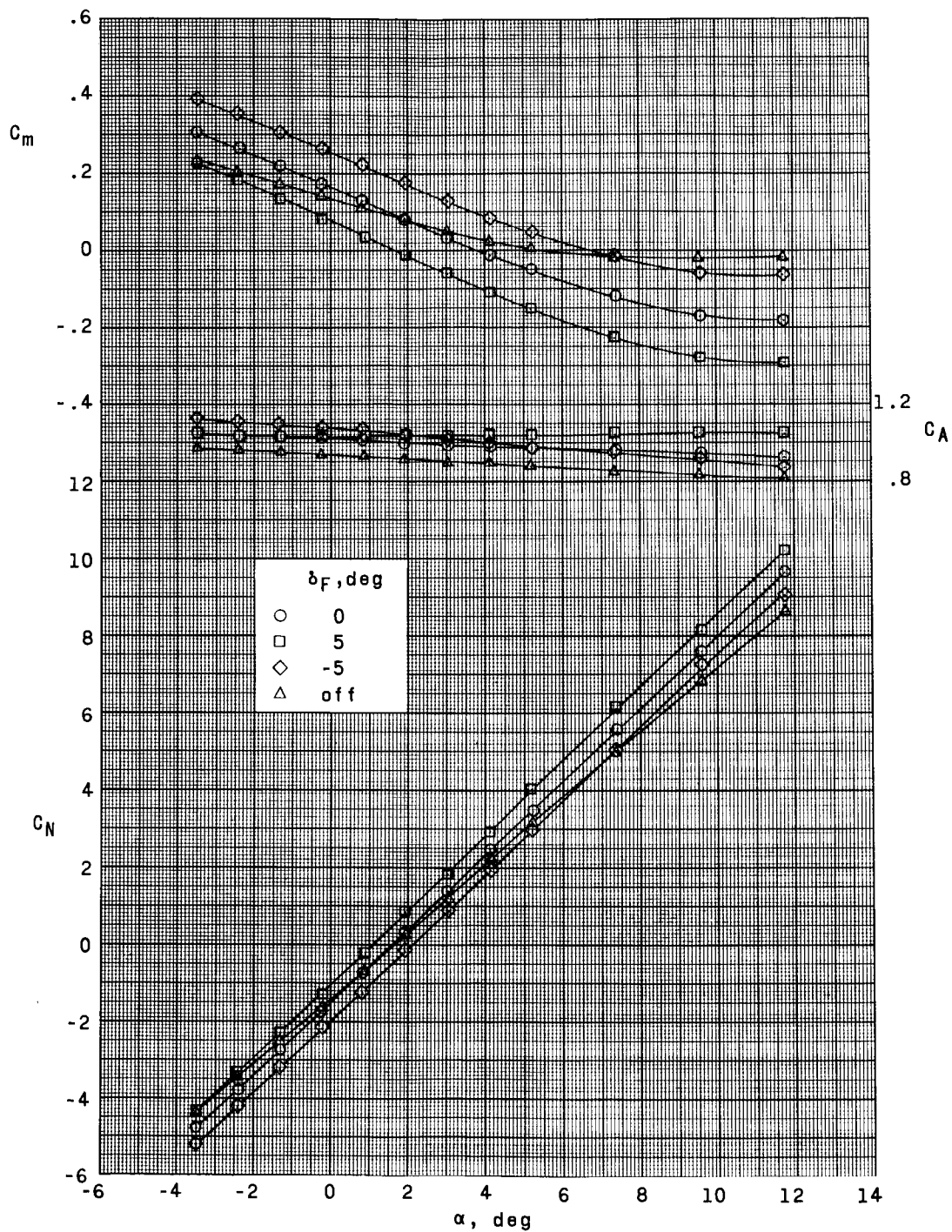
(a) Continued.

Figure 10.- Continued.



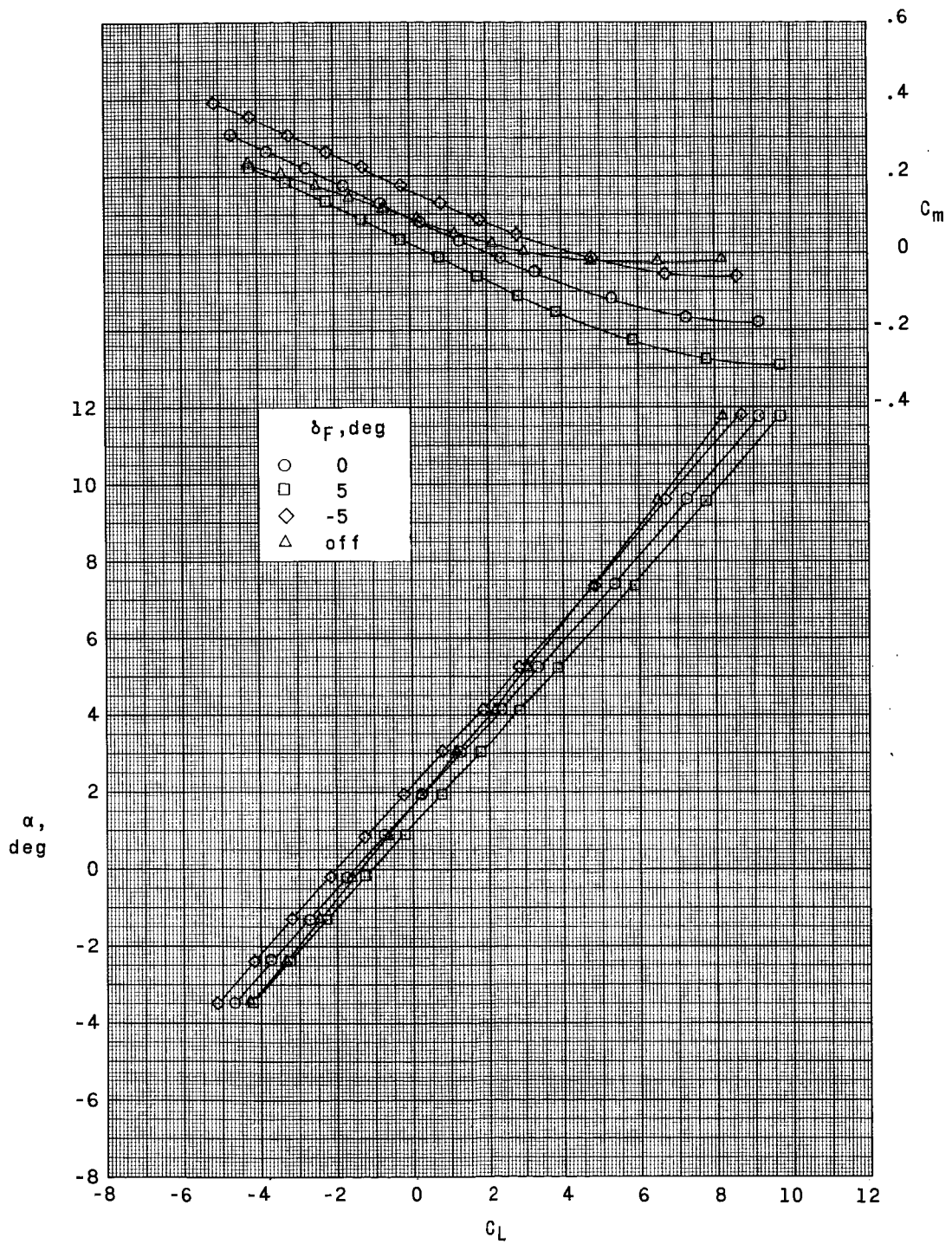
(a) Concluded.

Figure 10.- Continued.



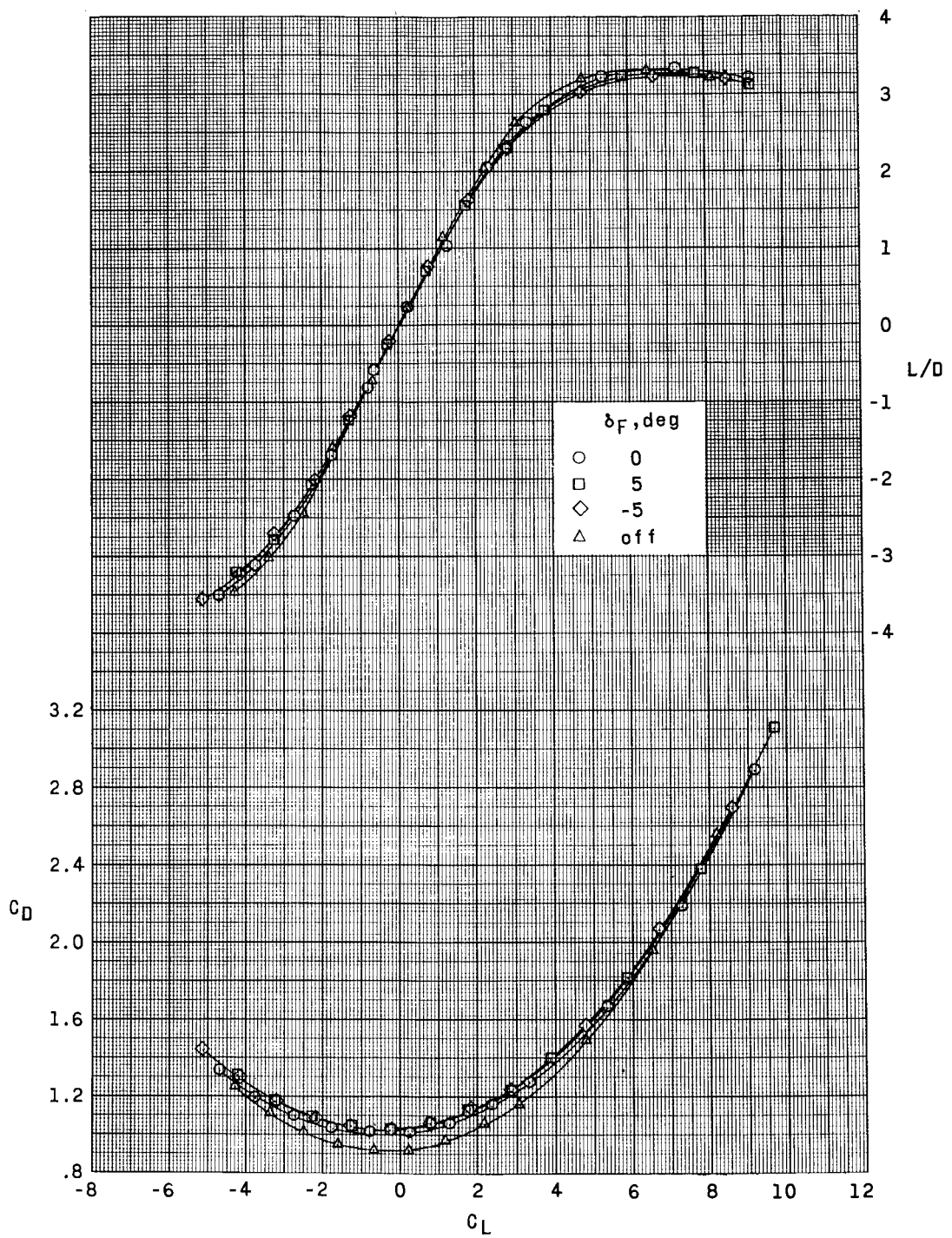
(b) $M = 2.00$.

Figure 10.- Continued.



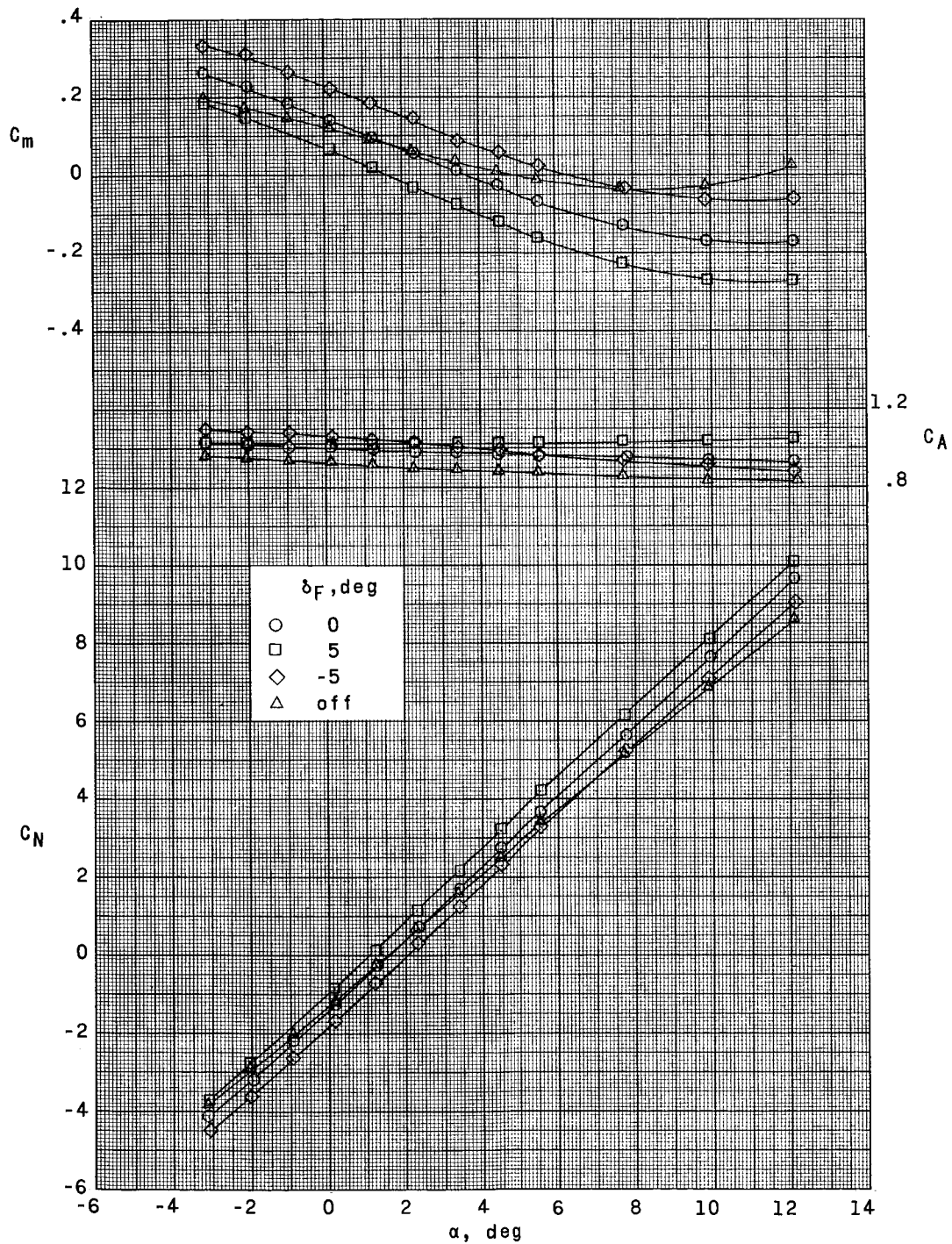
(b) Continued.

Figure 10.- Continued.



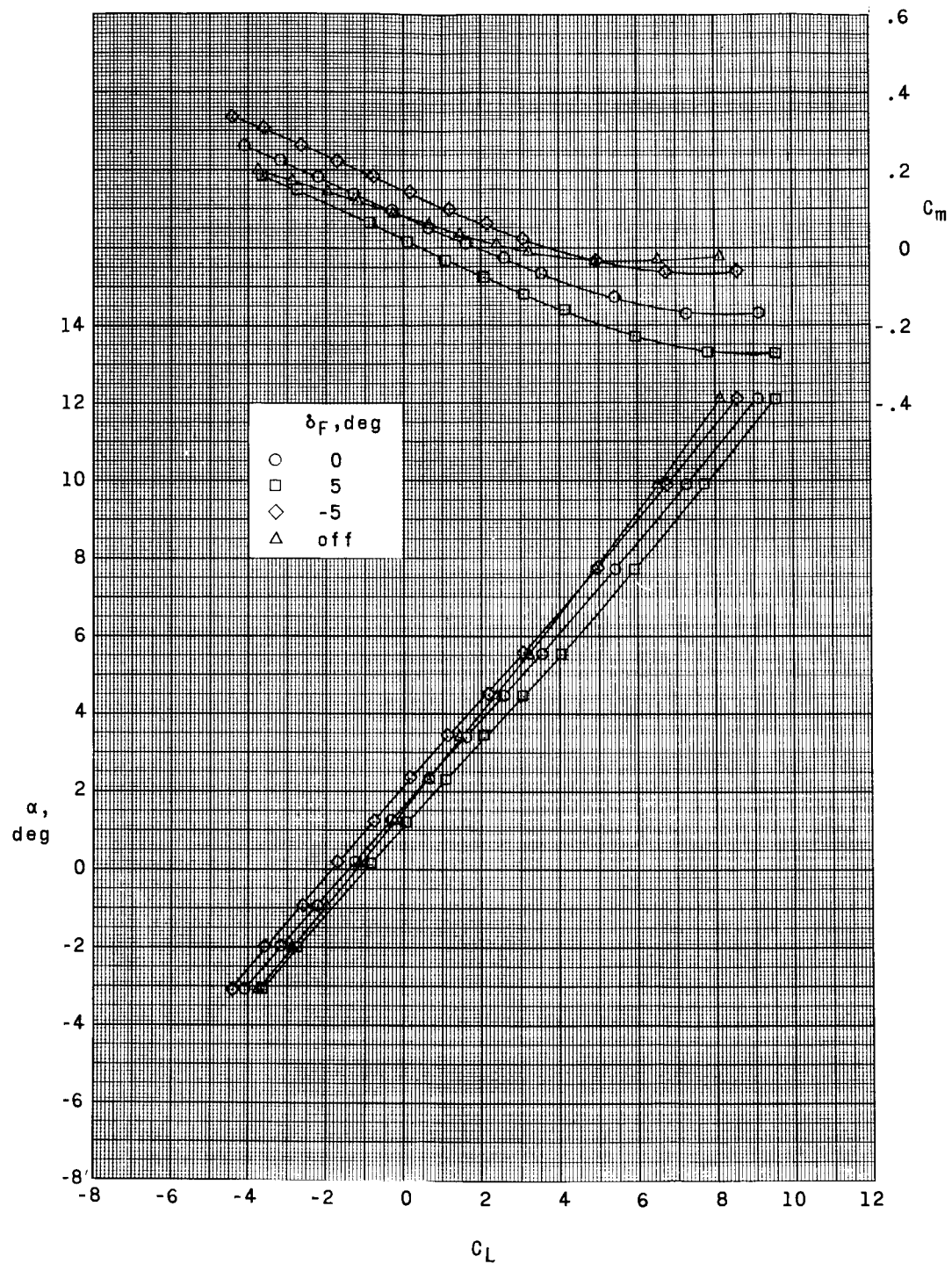
(b) Concluded.

Figure 10.- Continued.



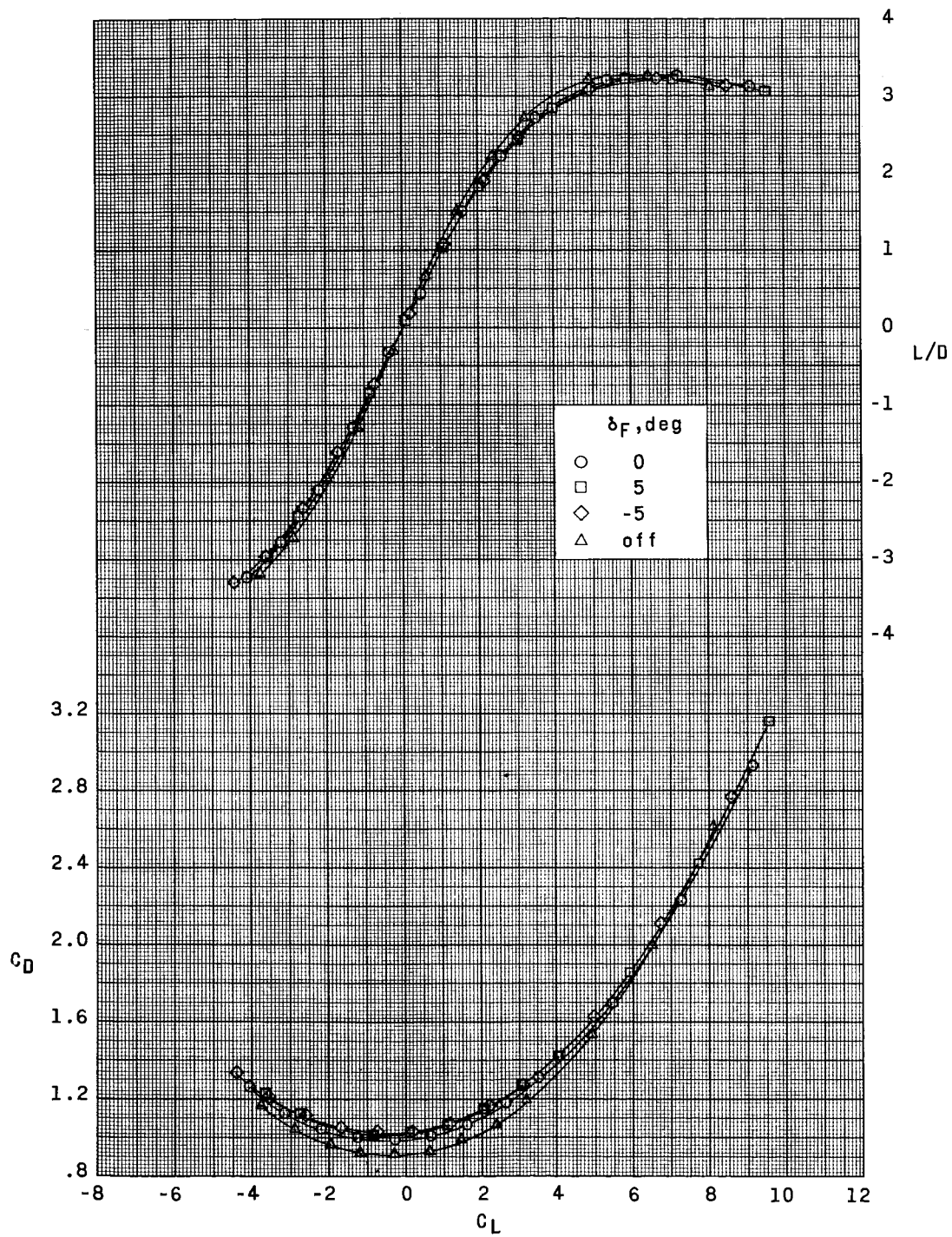
(c) $M = 2.16$.

Figure 10.- Continued.



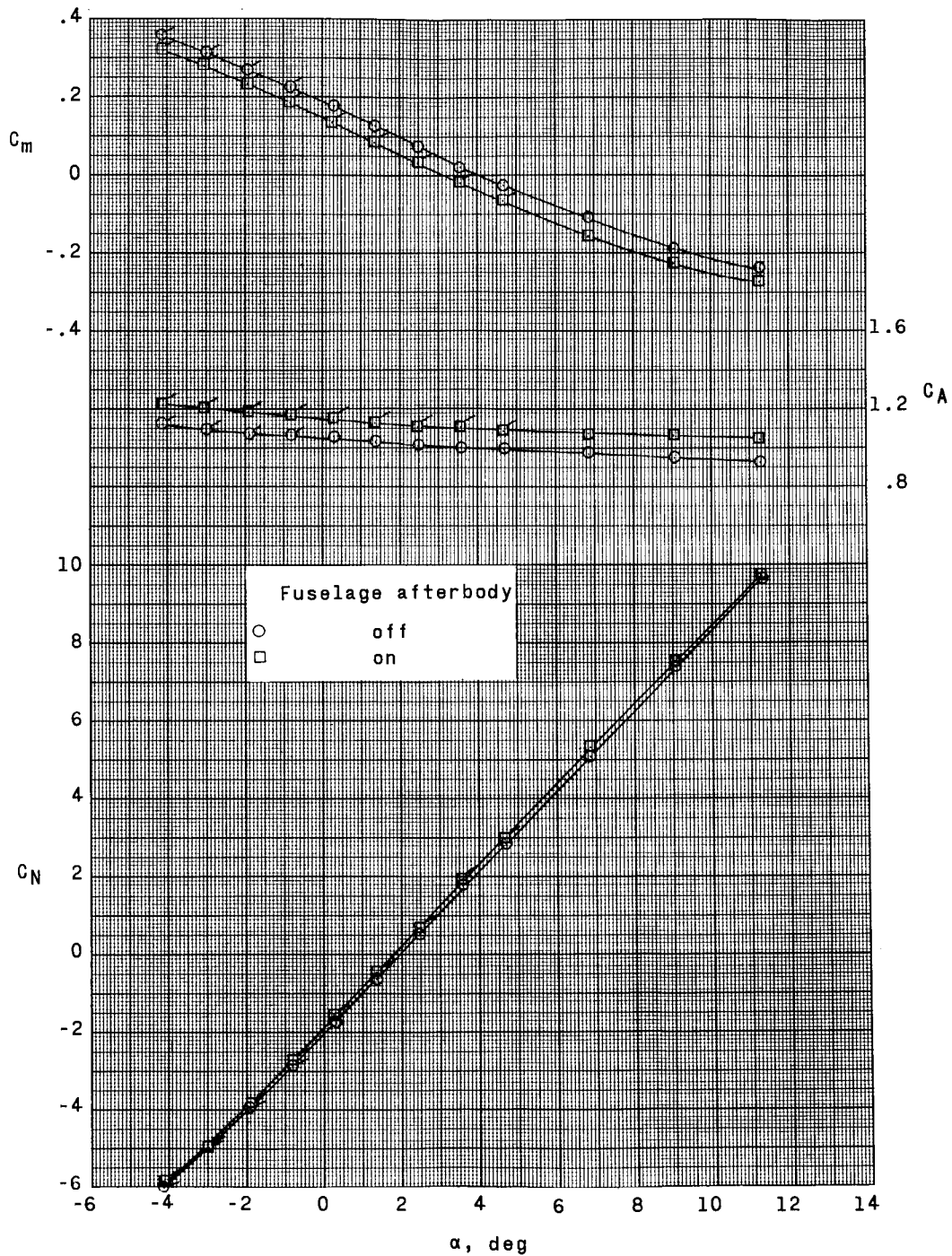
(c) Continued.

Figure 10.- Continued.



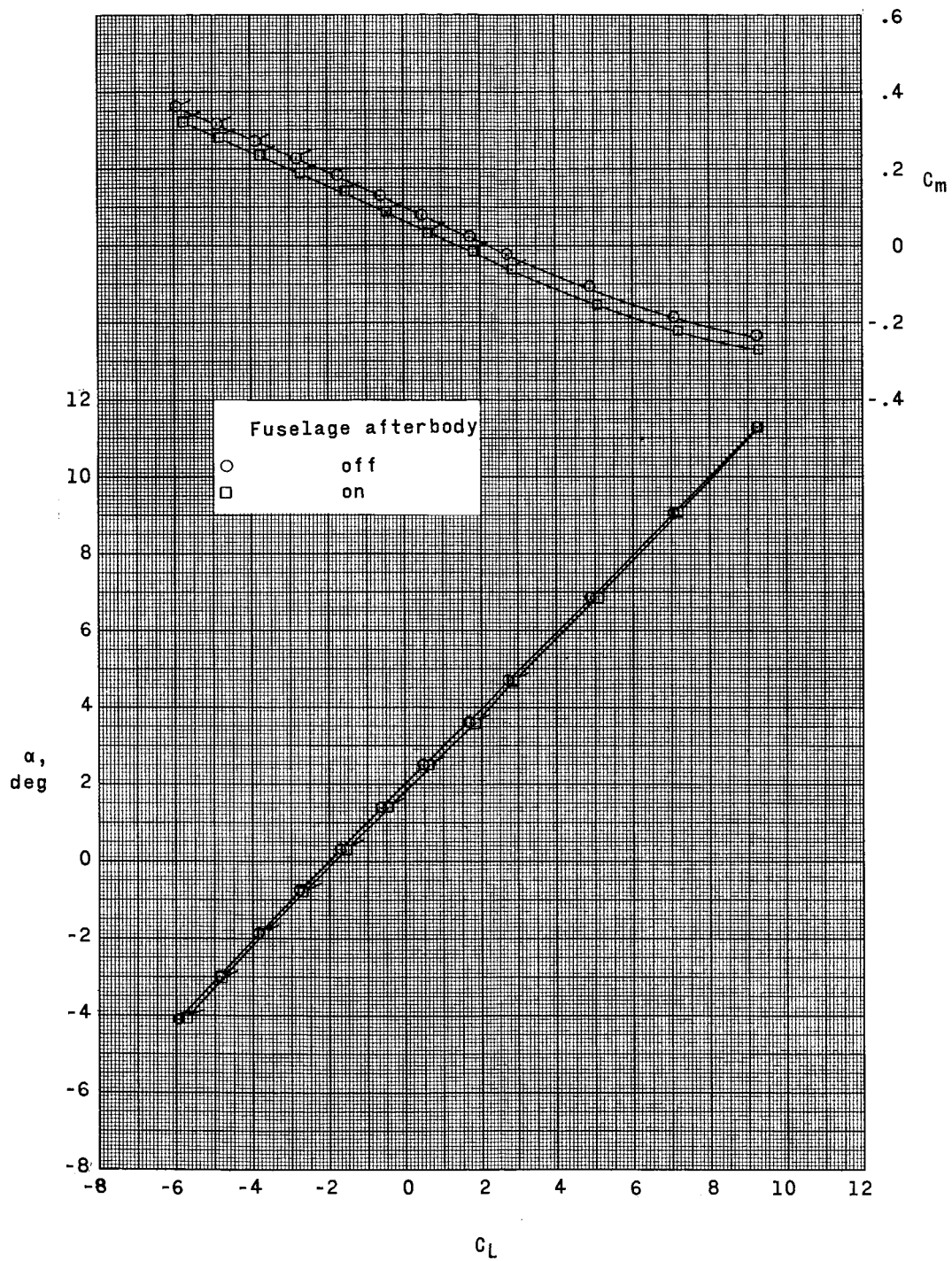
(c) Concluded.

Figure 10.- Concluded.



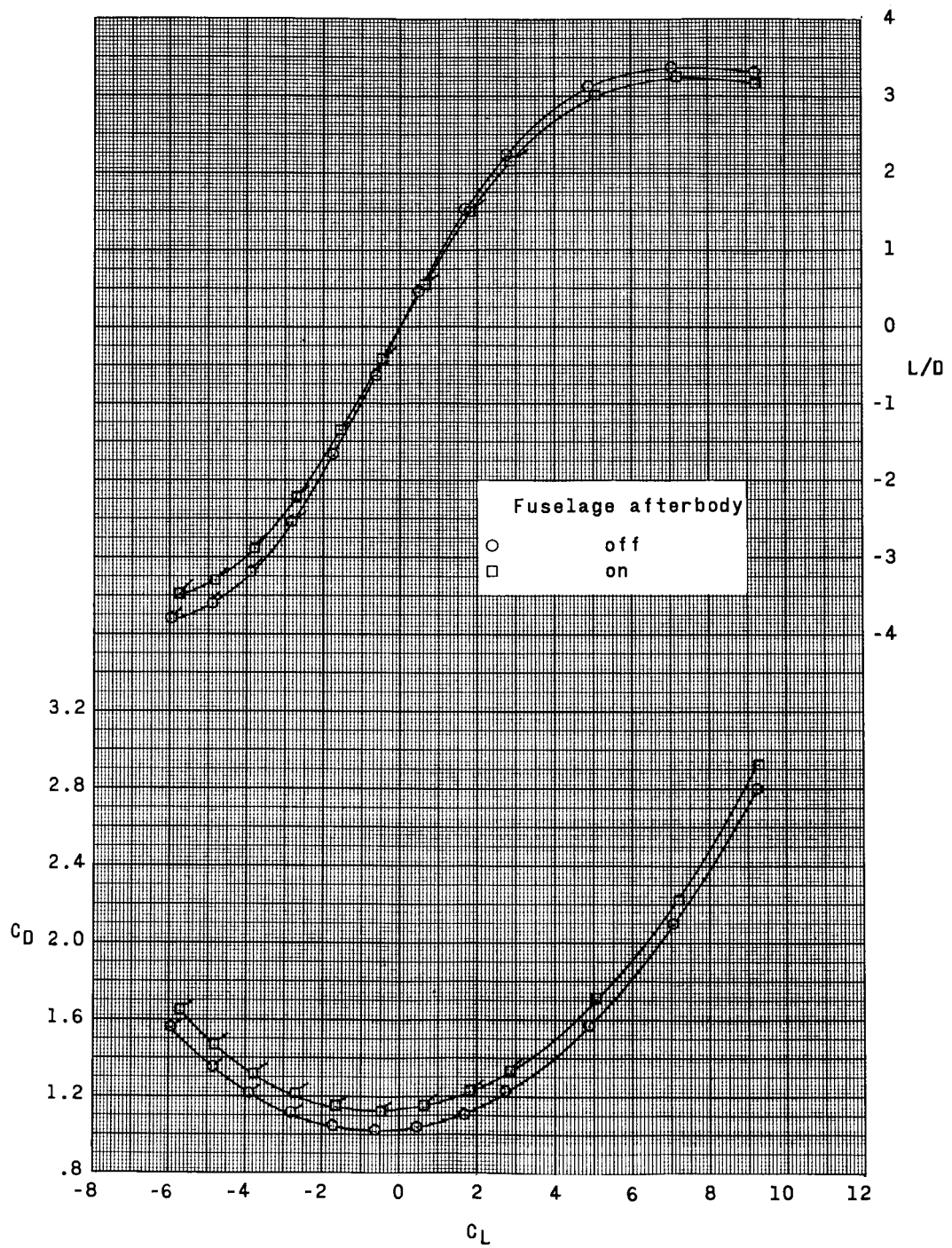
(a) $M = 1.80$.

Figure 11.- Effect of fuselage afterbody on longitudinal aerodynamic characteristics. Balance in nacelle; $\delta_f = 0^\circ$; $\delta_p = 0^\circ$. (Flagged symbols denote shock impingement on model.)



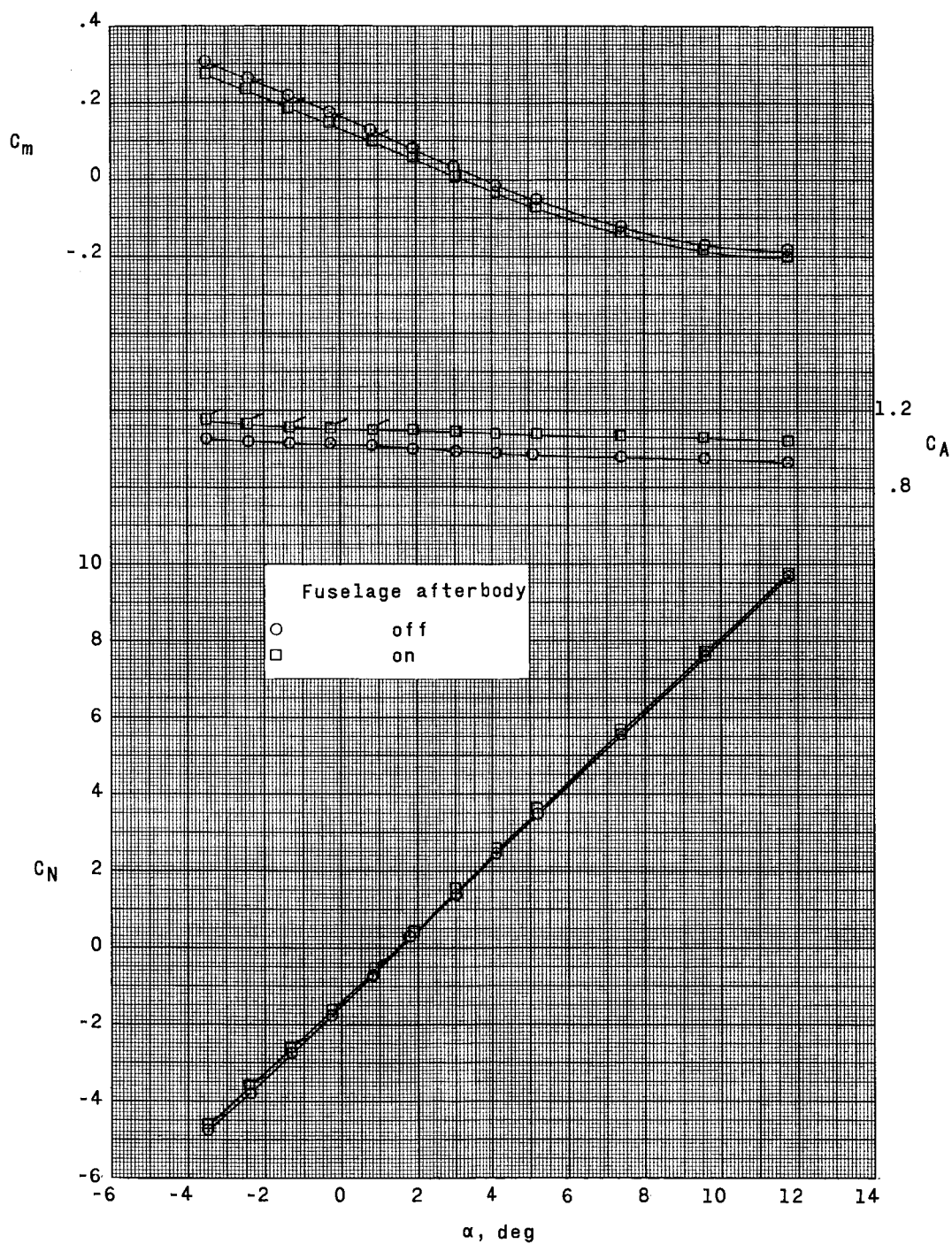
(a) Continued.

Figure 11.- Continued.



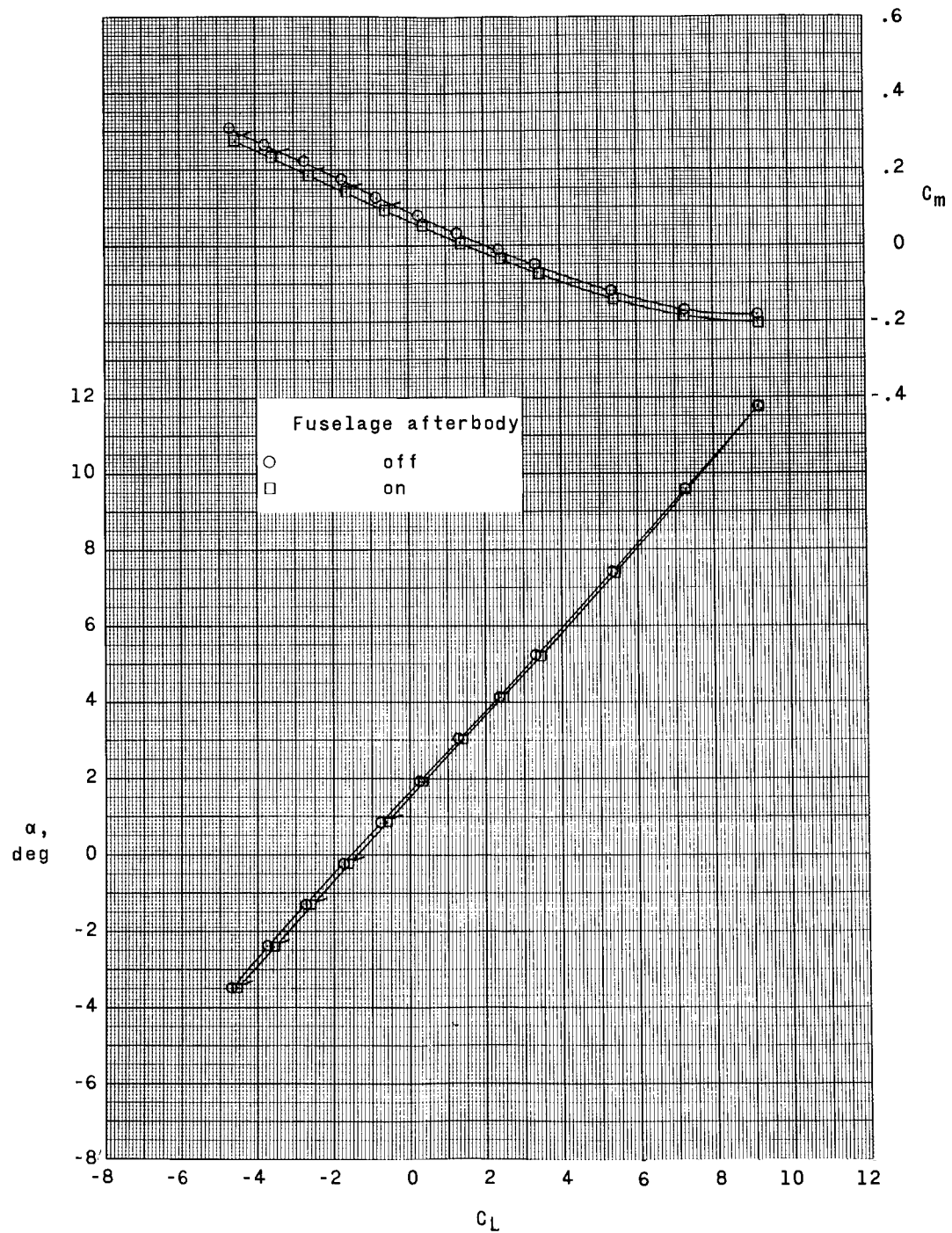
(a) Concluded.

Figure 11.- Continued.



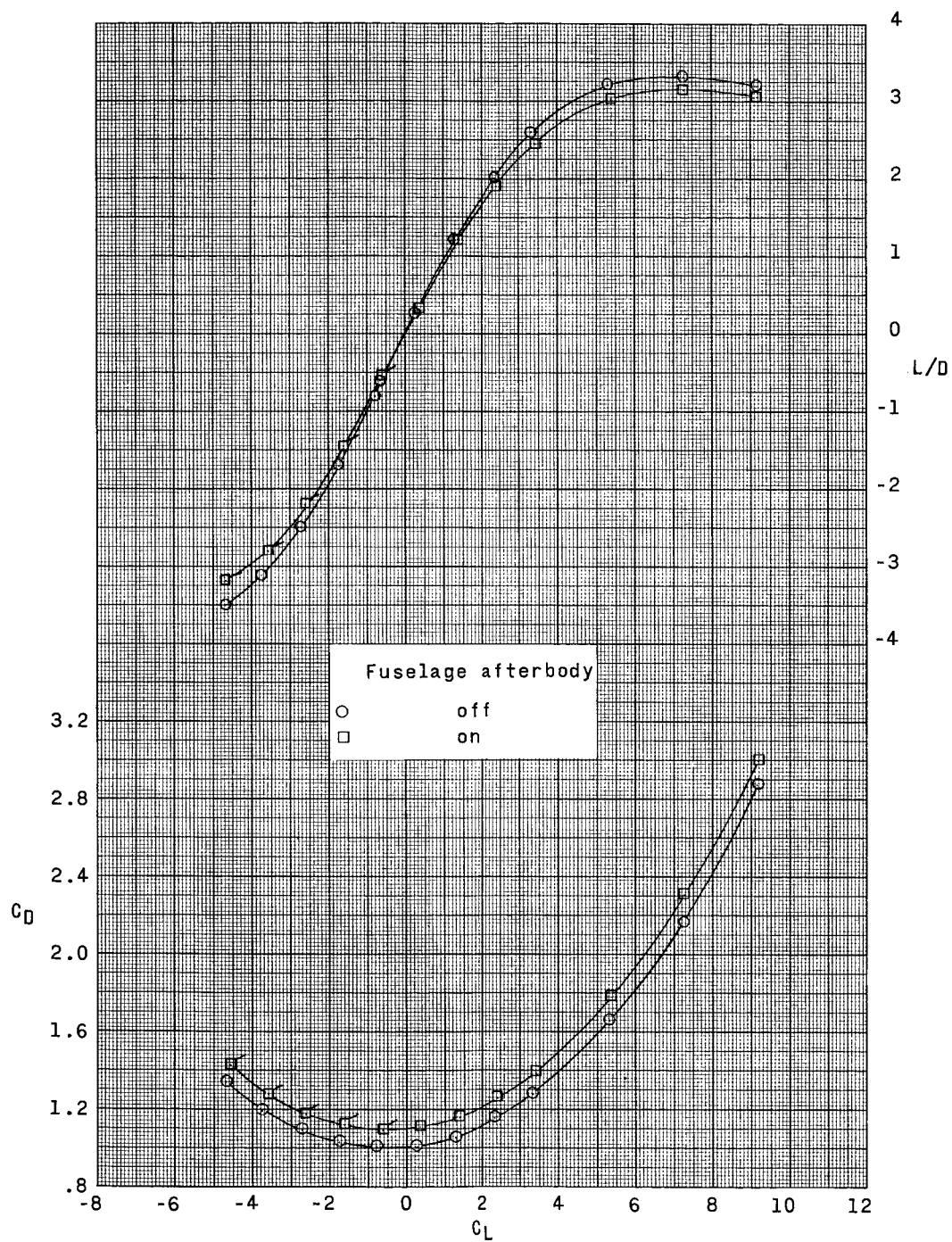
(b) $M = 2.00$.

Figure 11.- Continued.



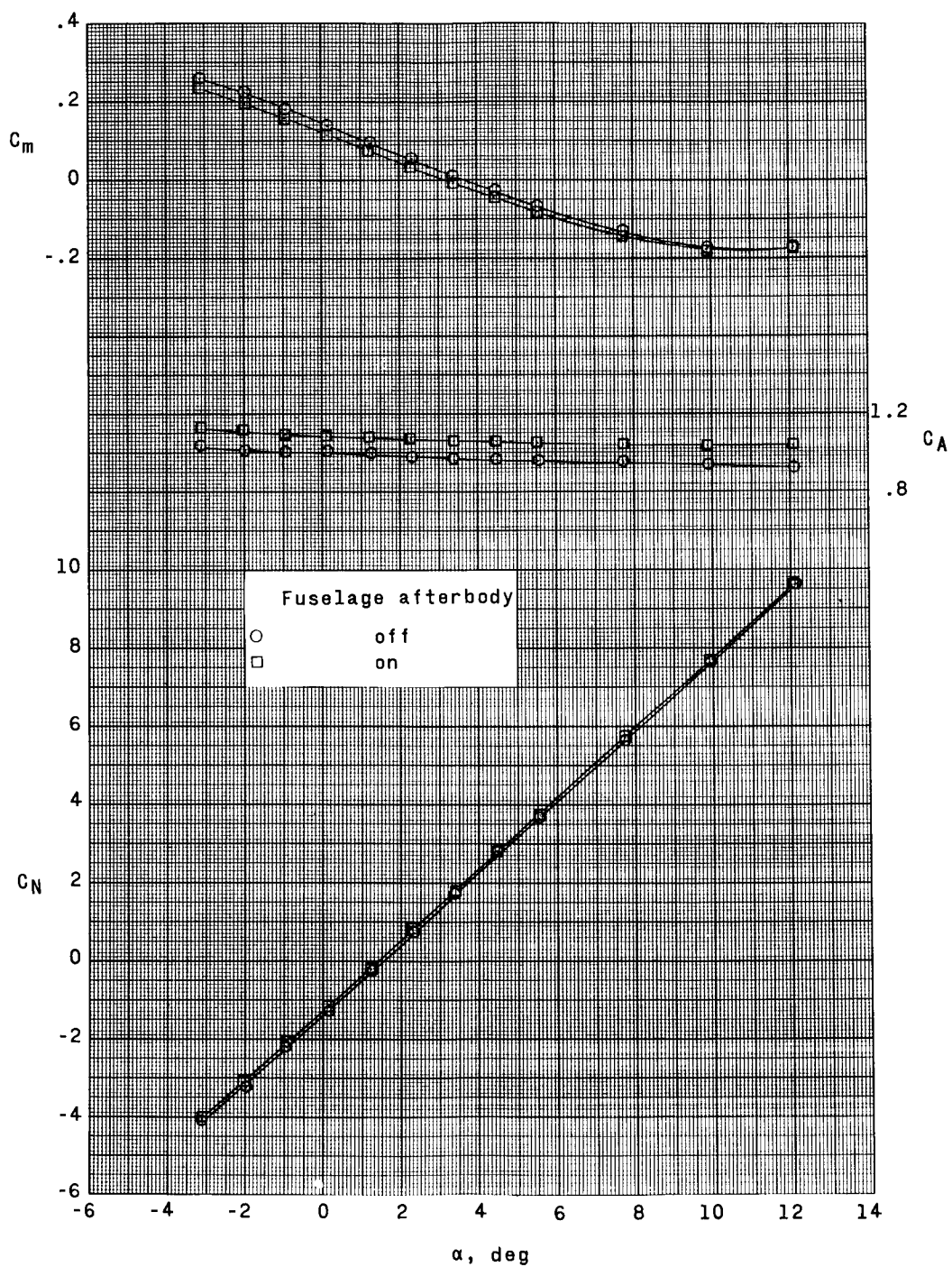
(b) Continued.

Figure 11.- Continued.



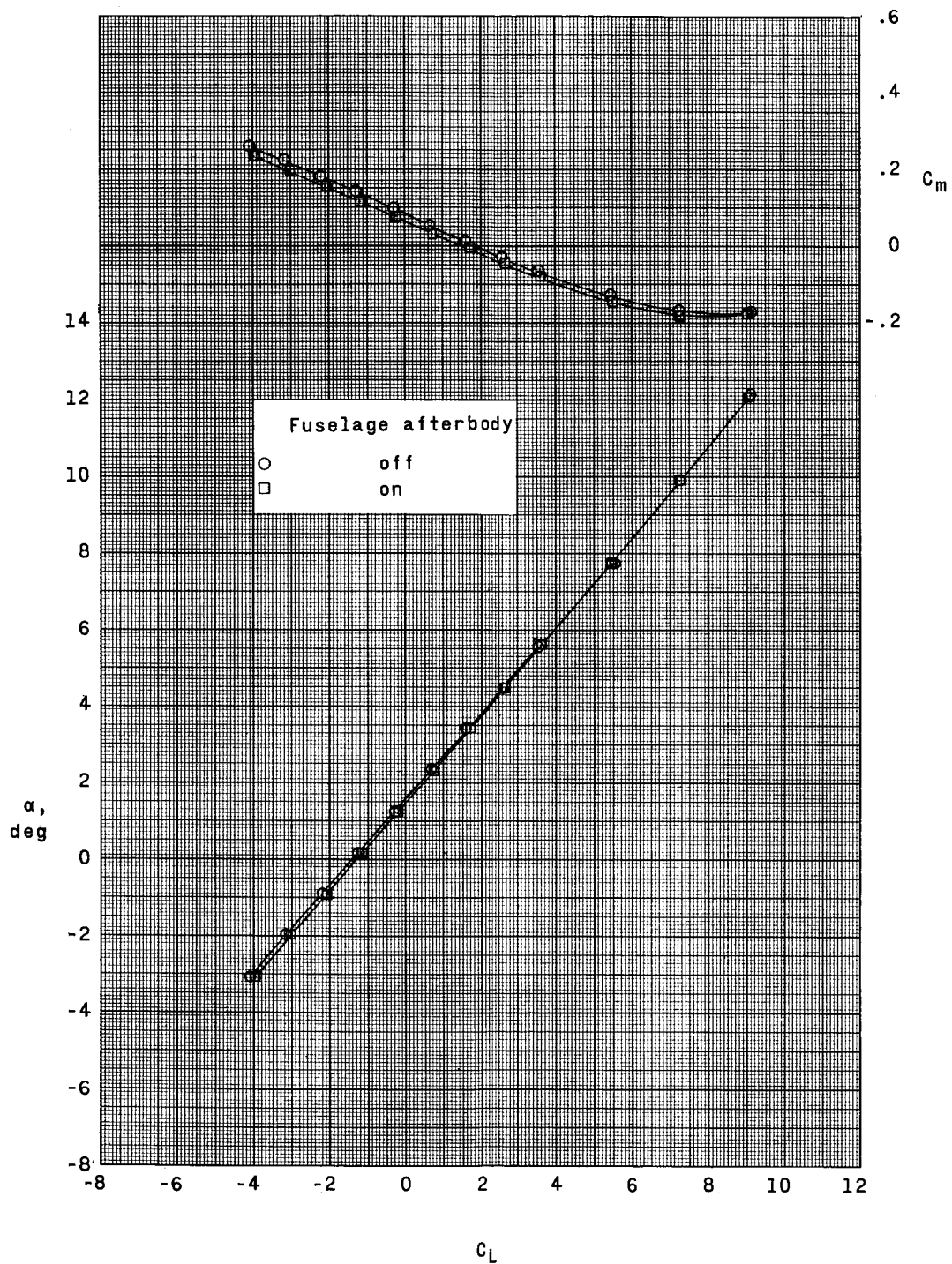
(b) Concluded.

Figure 11.- Continued.



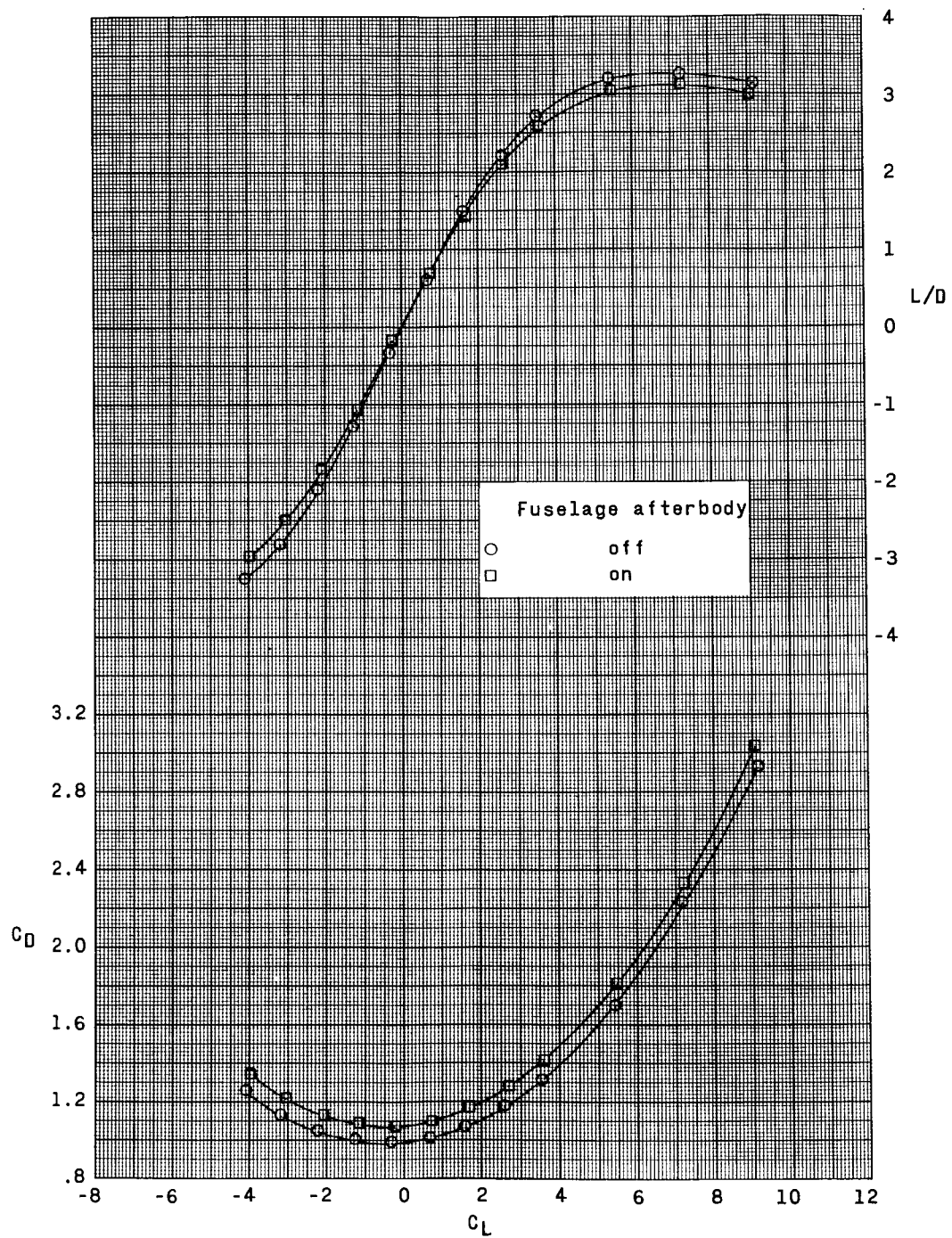
(c) $M = 2.16$.

Figure 11.- Continued.



(c) Continued.

Figure 11.- Continued.



(c) Concluded.

Figure 11.- Concluded.

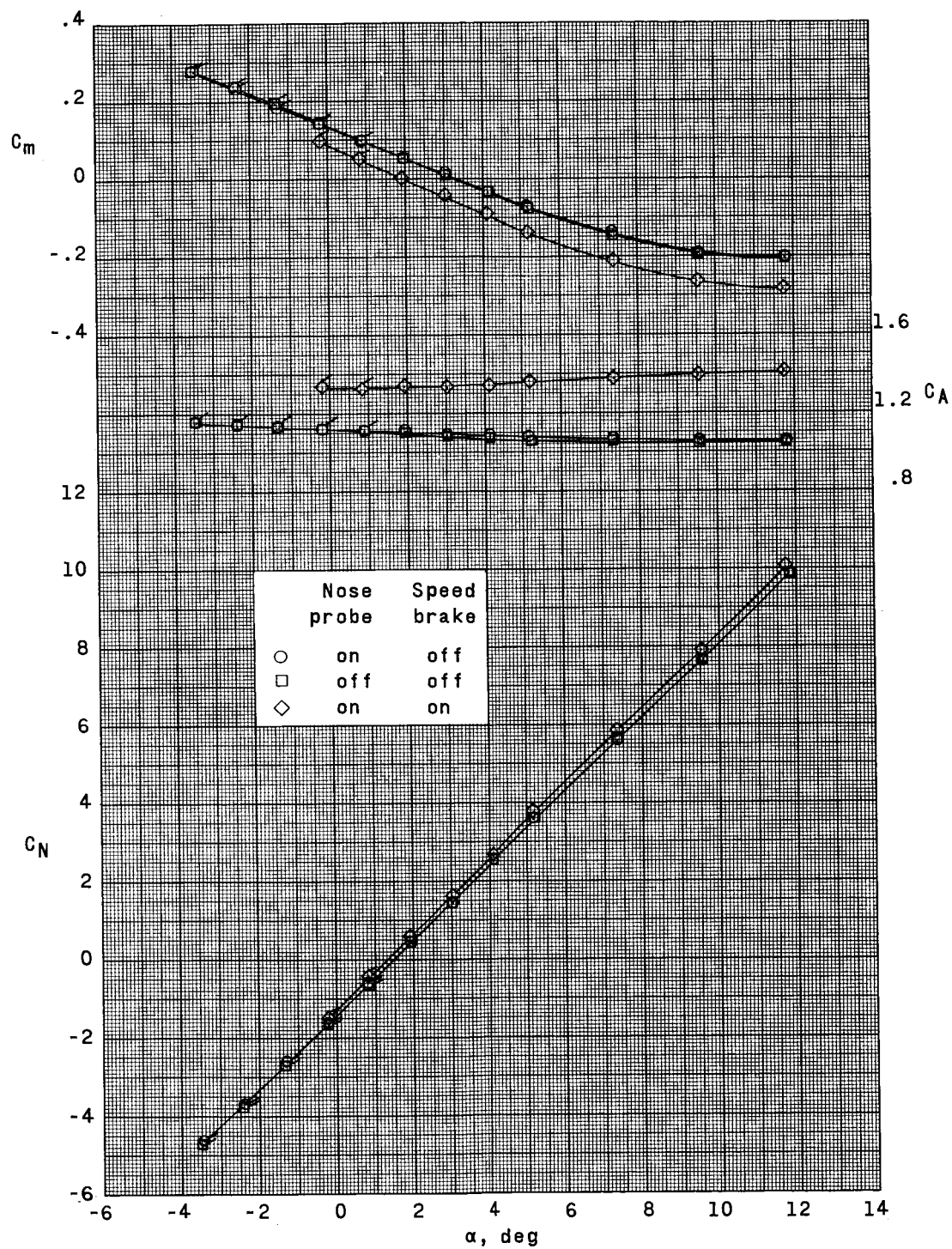


Figure 12.- Effect of nose probe and speed brake on longitudinal aerodynamic characteristics. Balance in nacelle; afterbody on; $\delta_F = 0^\circ$; $\delta_p = 0^\circ$; $M = 2.00$. (Flagged symbols denote shock impingement on model.)

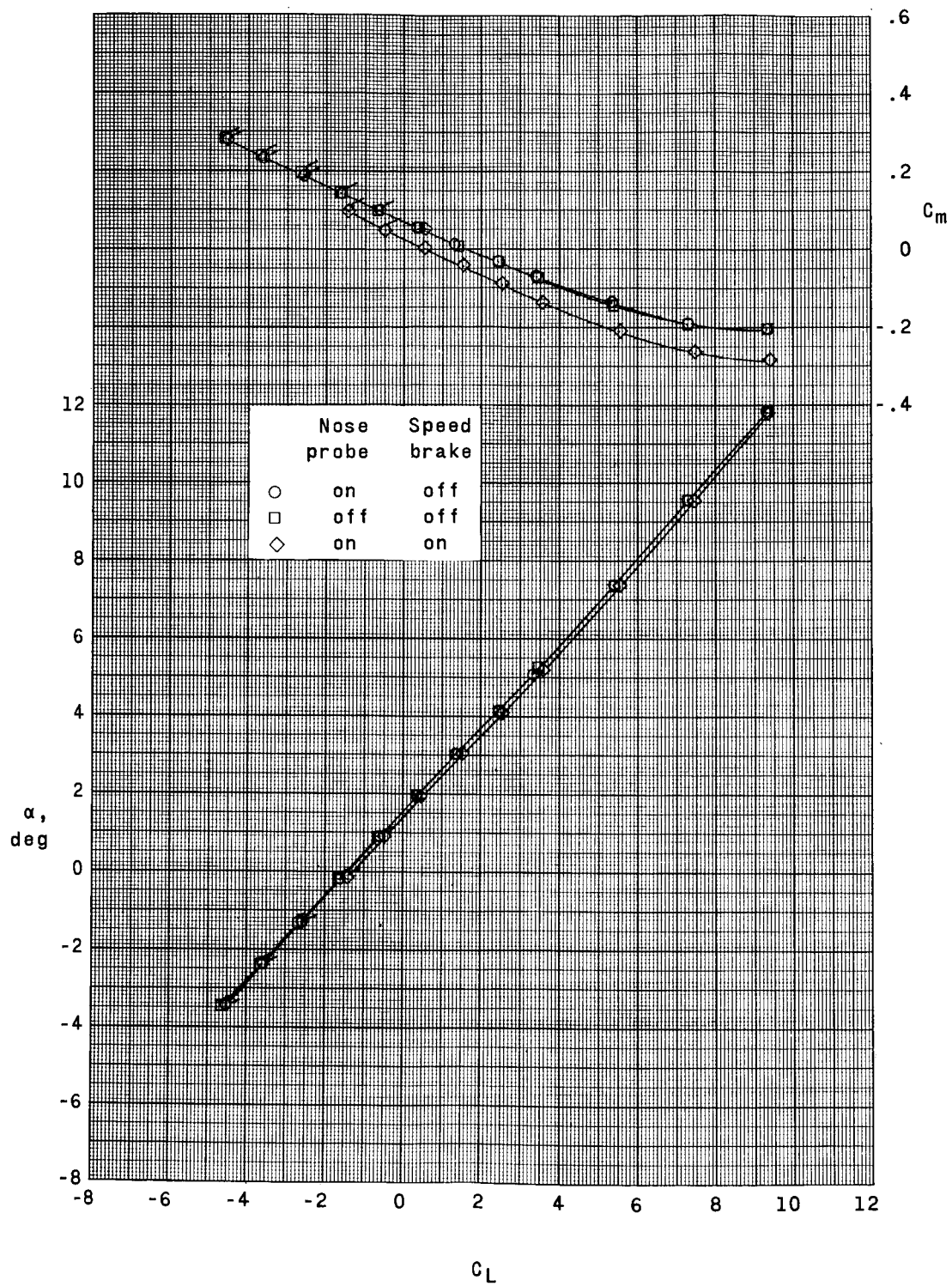


Figure 12.- Continued.

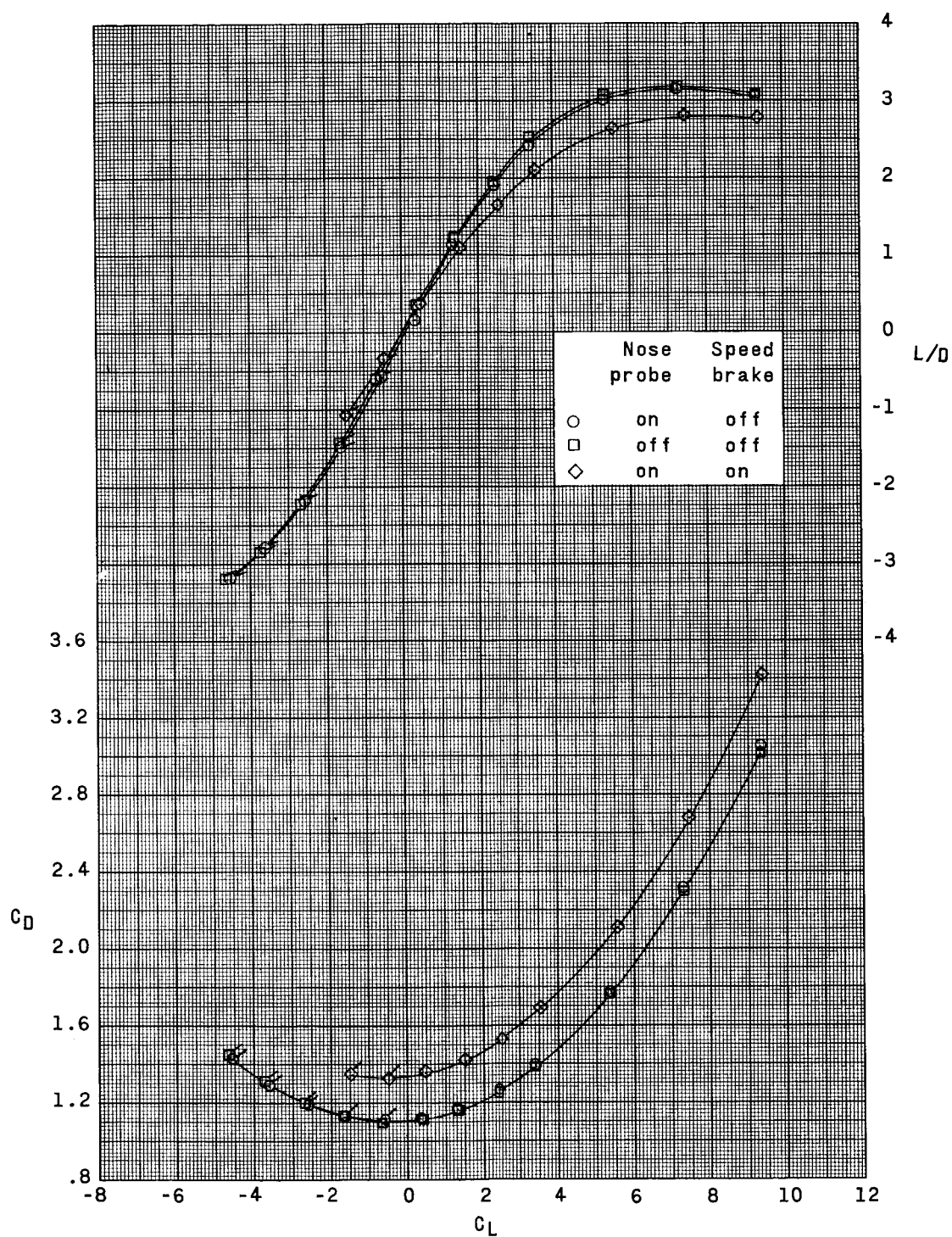


Figure 12.- Concluded.

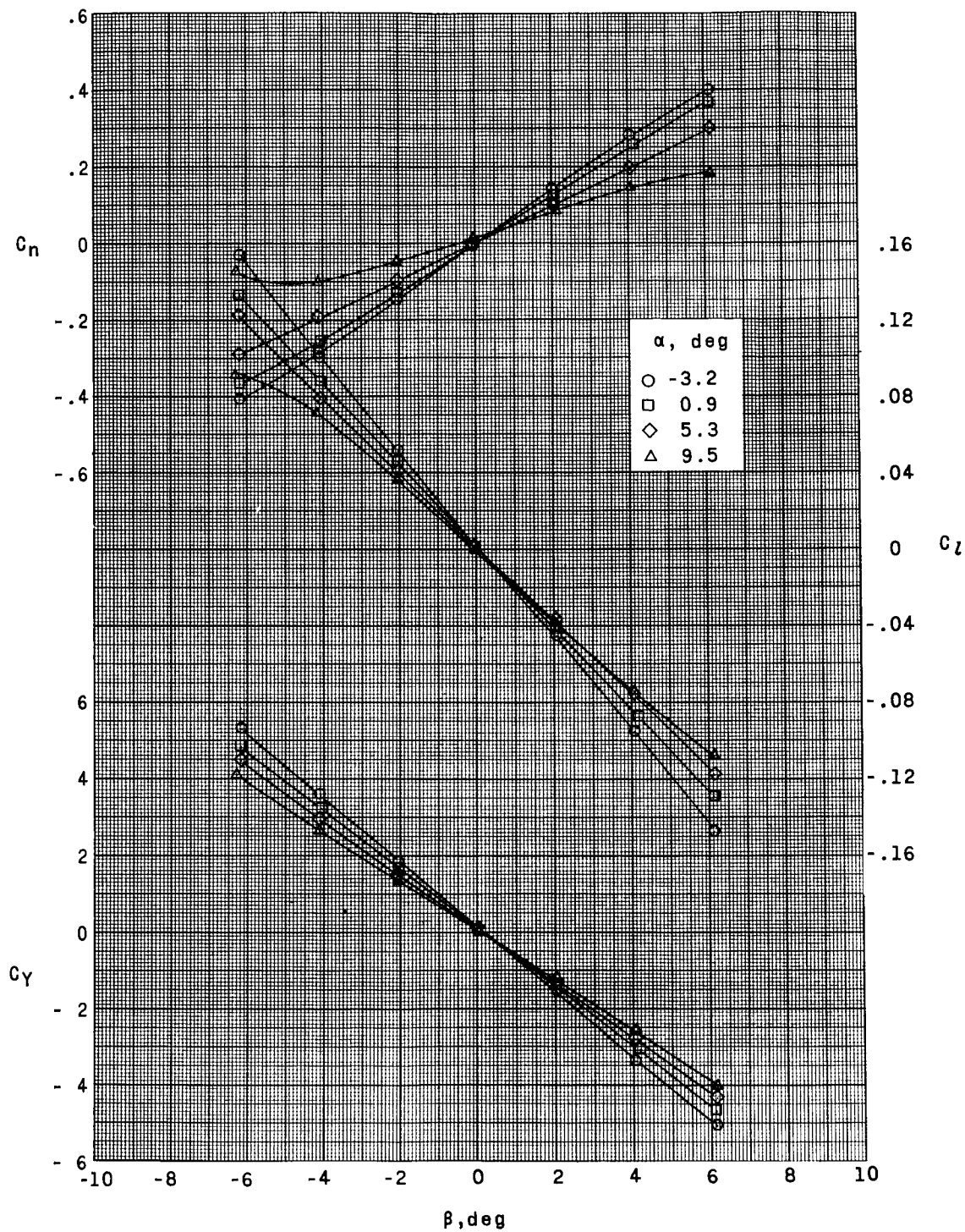
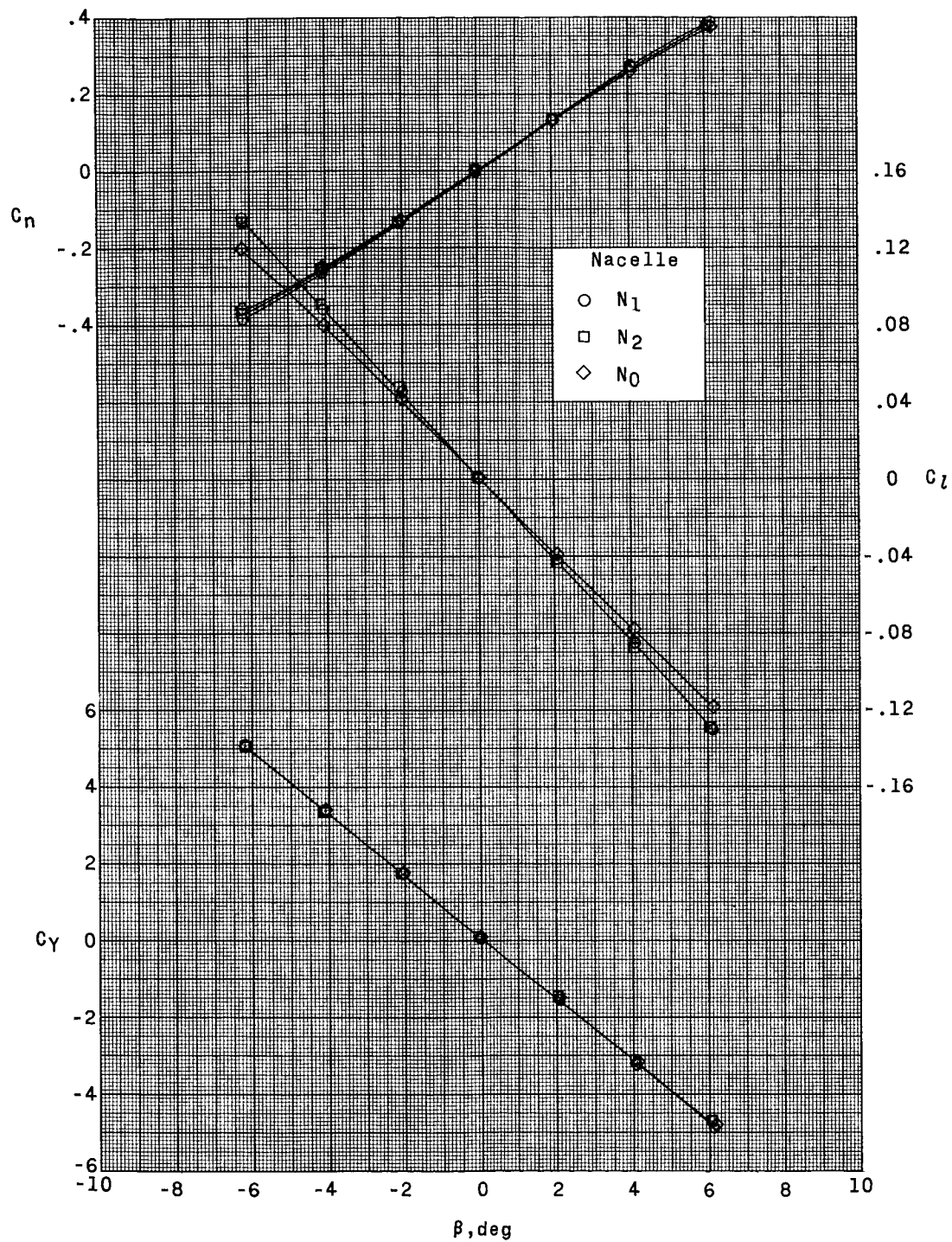
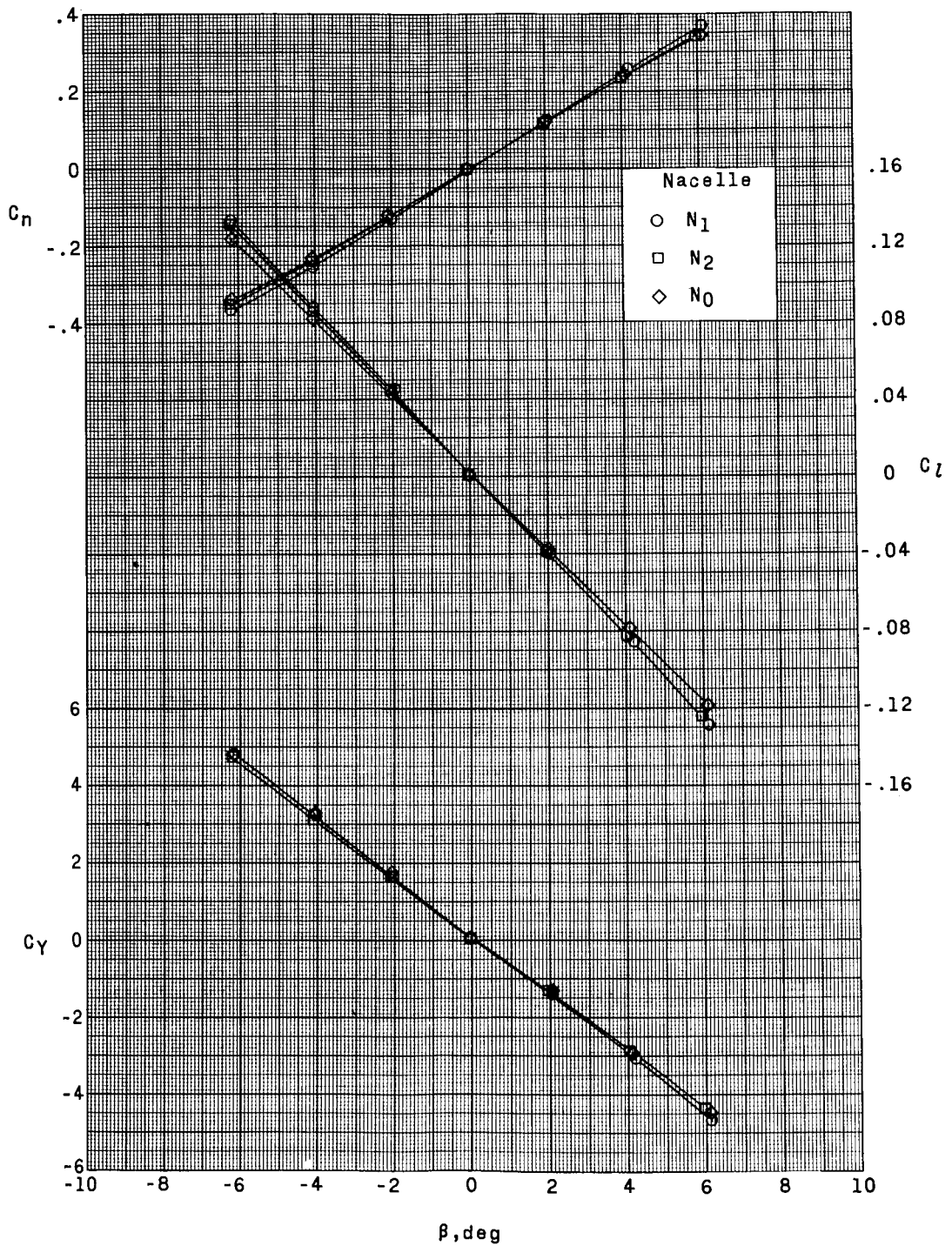


Figure 13.- Effect of angle of attack on lateral aerodynamic characteristics of the N₁ nacelle configuration. Balance in fuselage; $\delta_f = 0^\circ$; $\delta_p = 0^\circ$; $M = 2.00$.



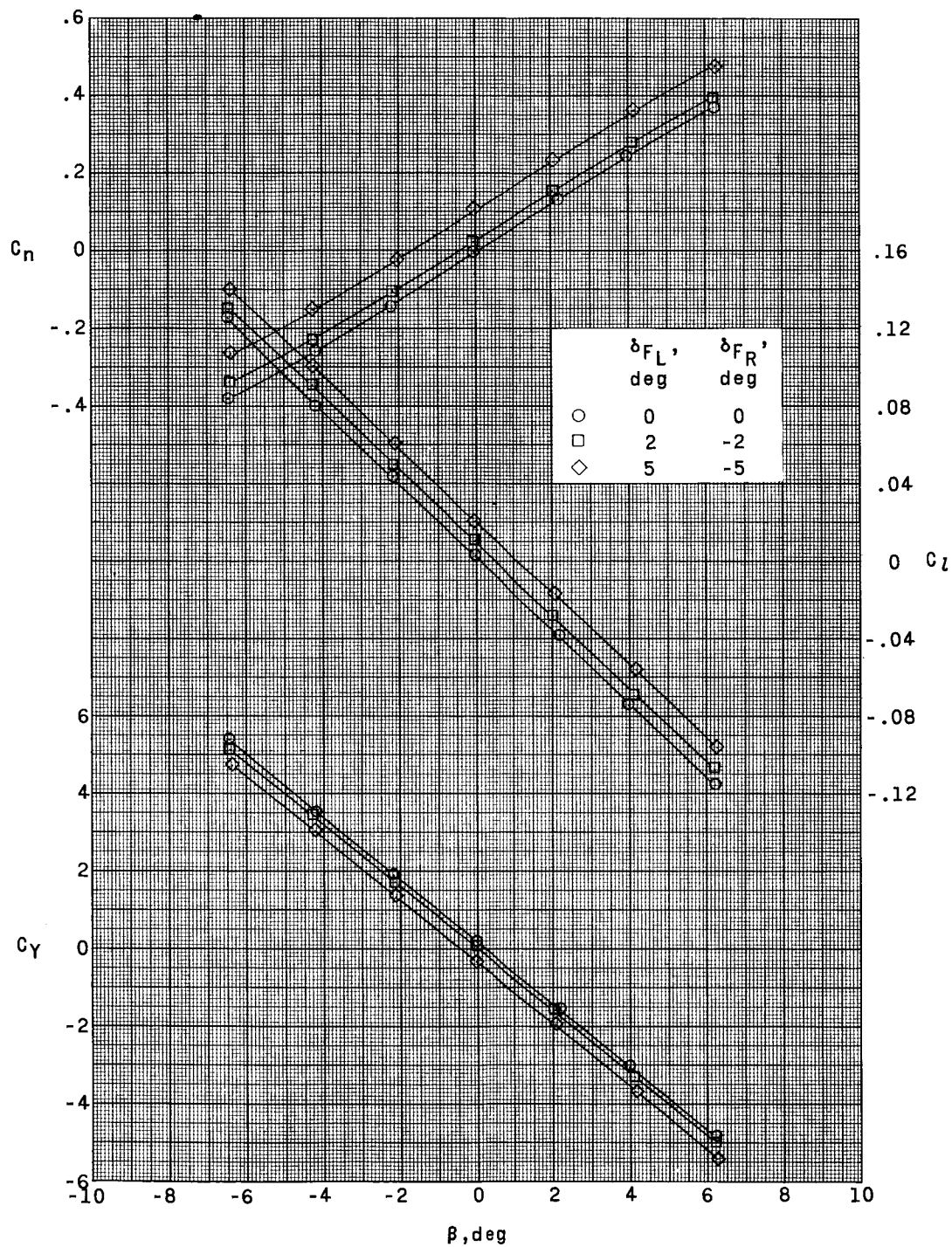
(a) $M = 1.80$; $\alpha = 0.5^\circ$.

Figure 14.- Effect of mass-flow ratio of nacelles on lateral aerodynamic characteristics. Balance in fuselage; $\delta_f = 0^\circ$; $\delta_p = 0^\circ$.



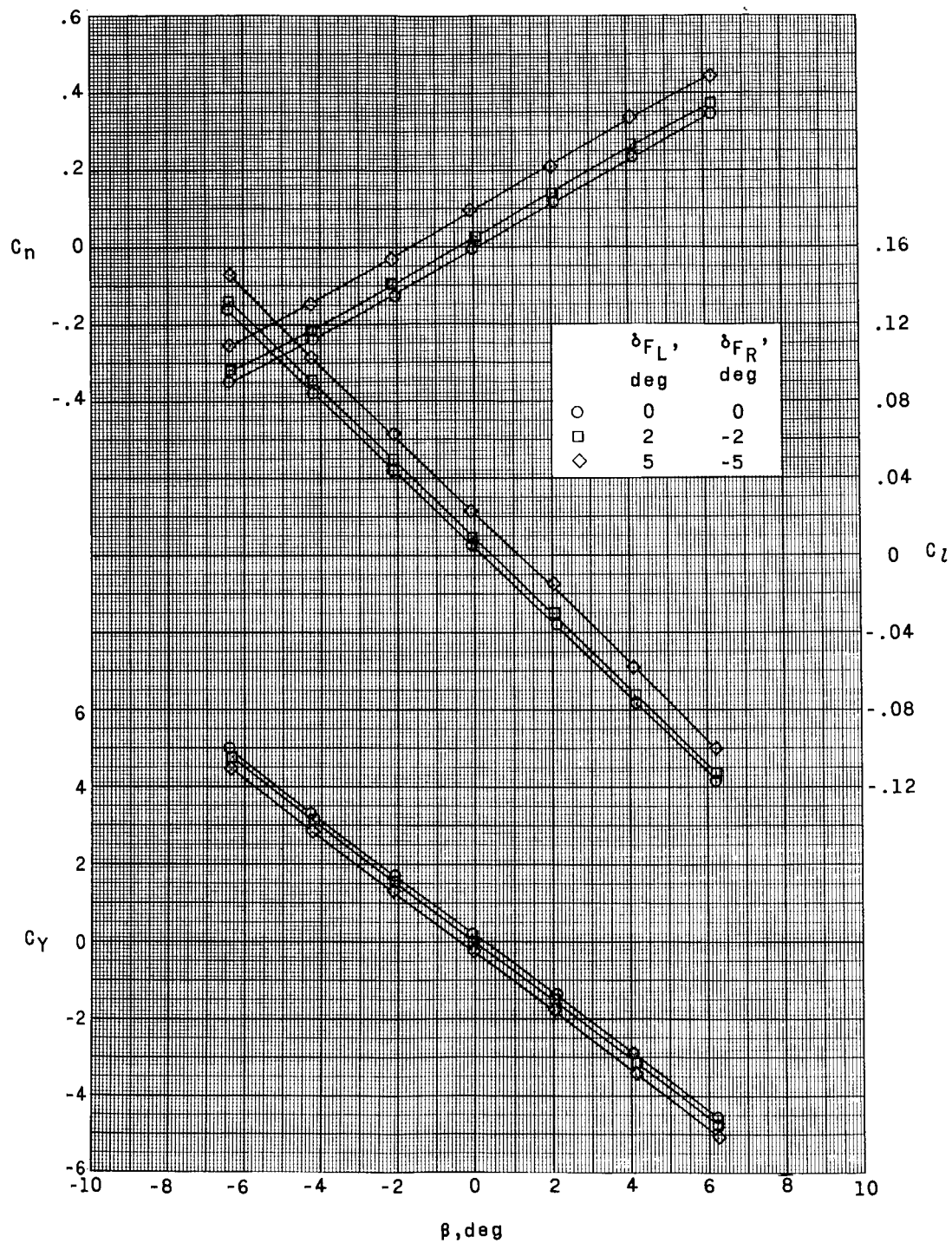
(b) $M = 2.00$; $\alpha = 1.0^\circ$.

Figure 14.- Concluded.



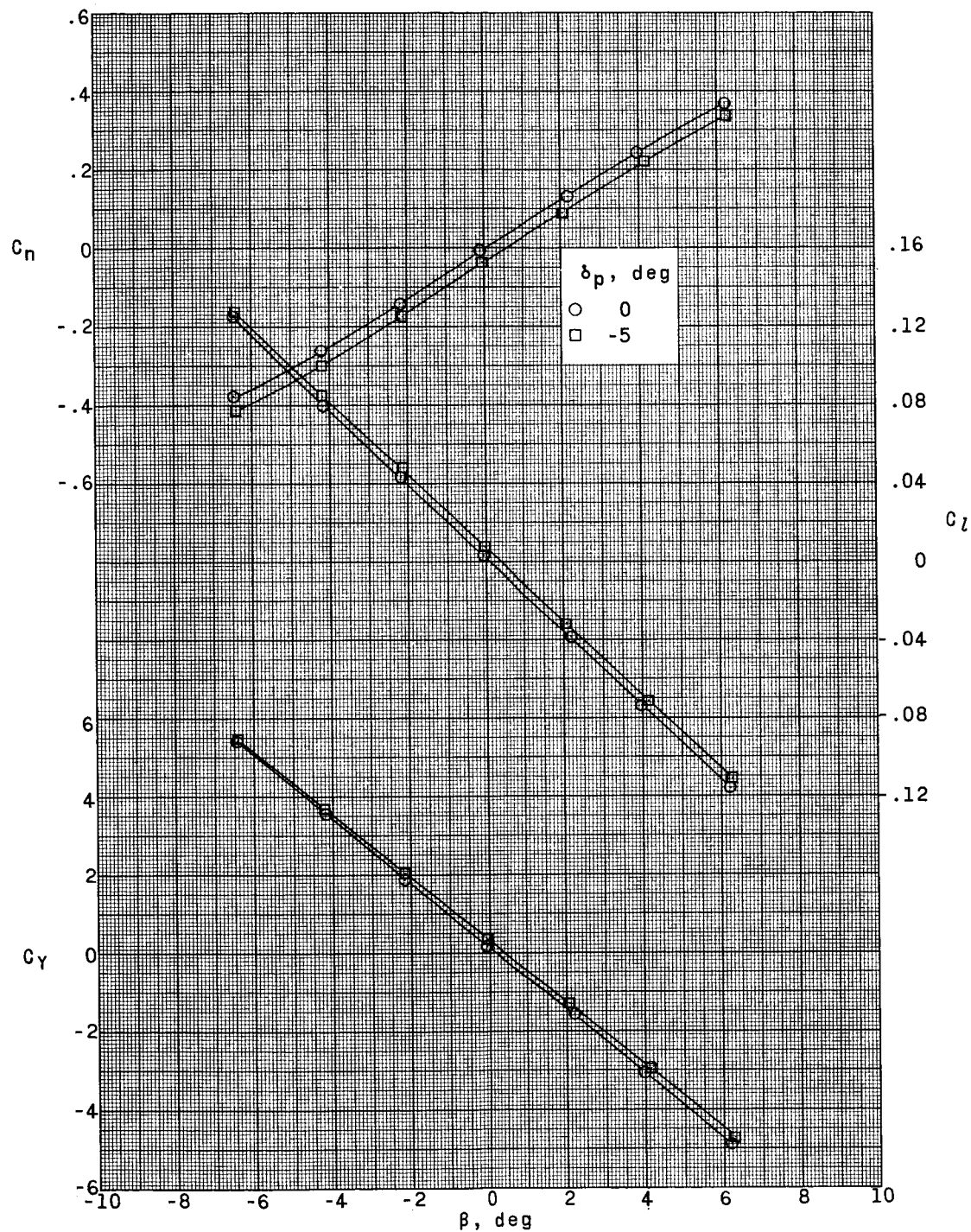
(a) $M = 1.80$; $\alpha = 0.3^\circ$.

Figure 15.- Effect of differential tail-fin deflections on lateral aerodynamic characteristics. Balance in nacelle; afterbody off; $\delta_p = 0^\circ$.



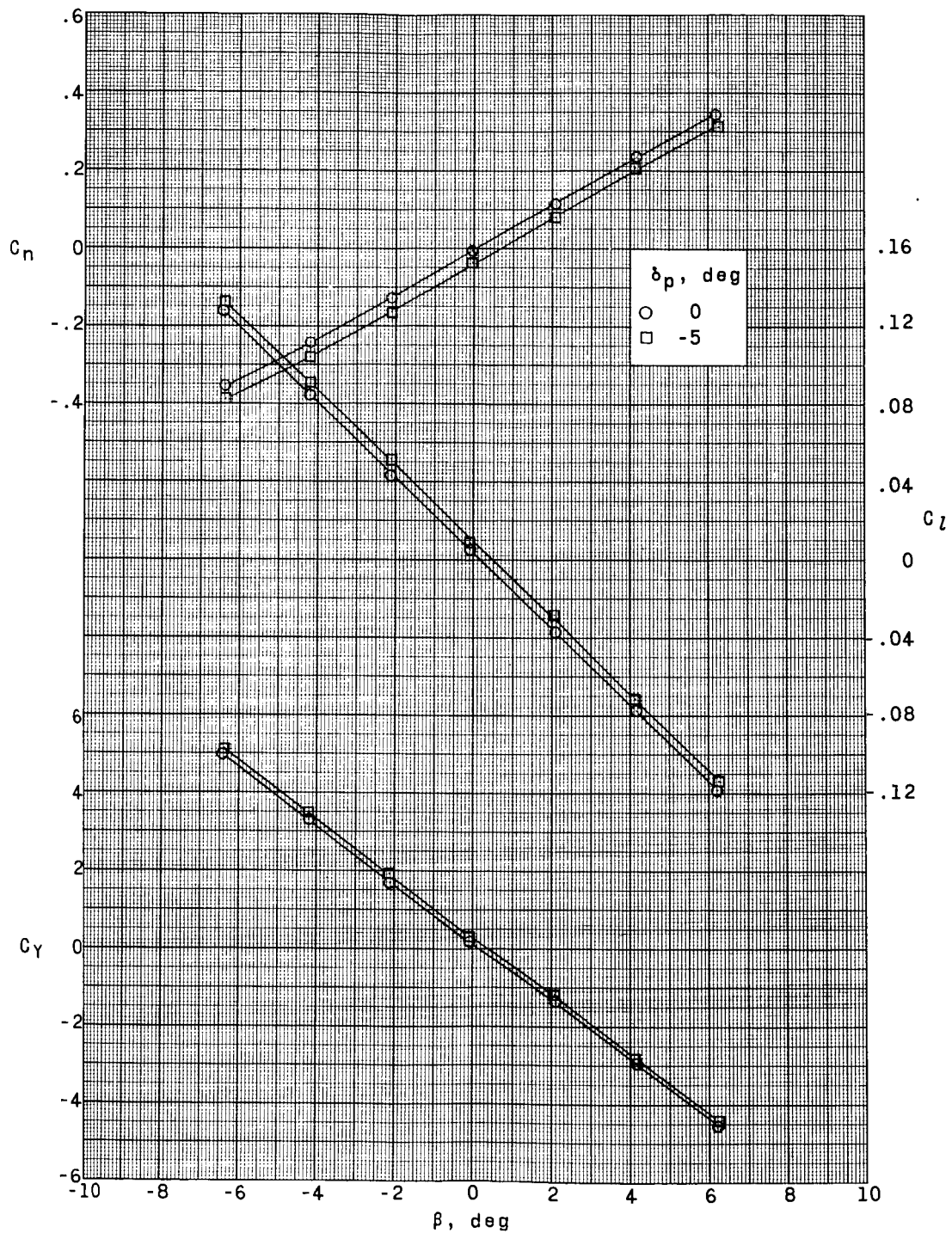
(b) $M = 2.00$; $\alpha = 0.90^\circ$.

Figure 15.- Concluded.



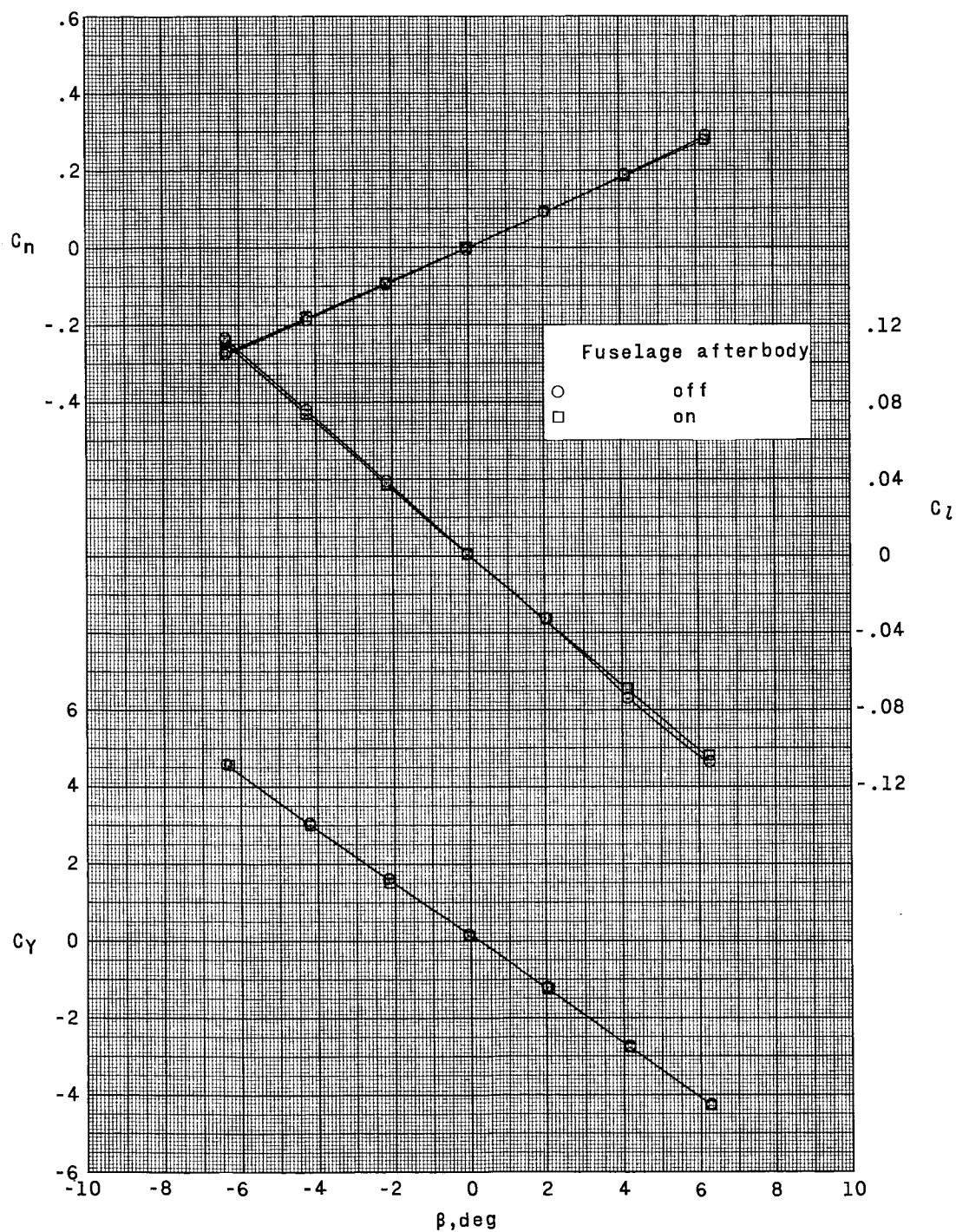
(a) $M = 1.80$; $\alpha = 0.3^\circ$.

Figure 16.- Effect of pylon rudder control on lateral aerodynamic characteristics. Balance in nacelle; afterbody off; $\delta_F = 0^\circ$.



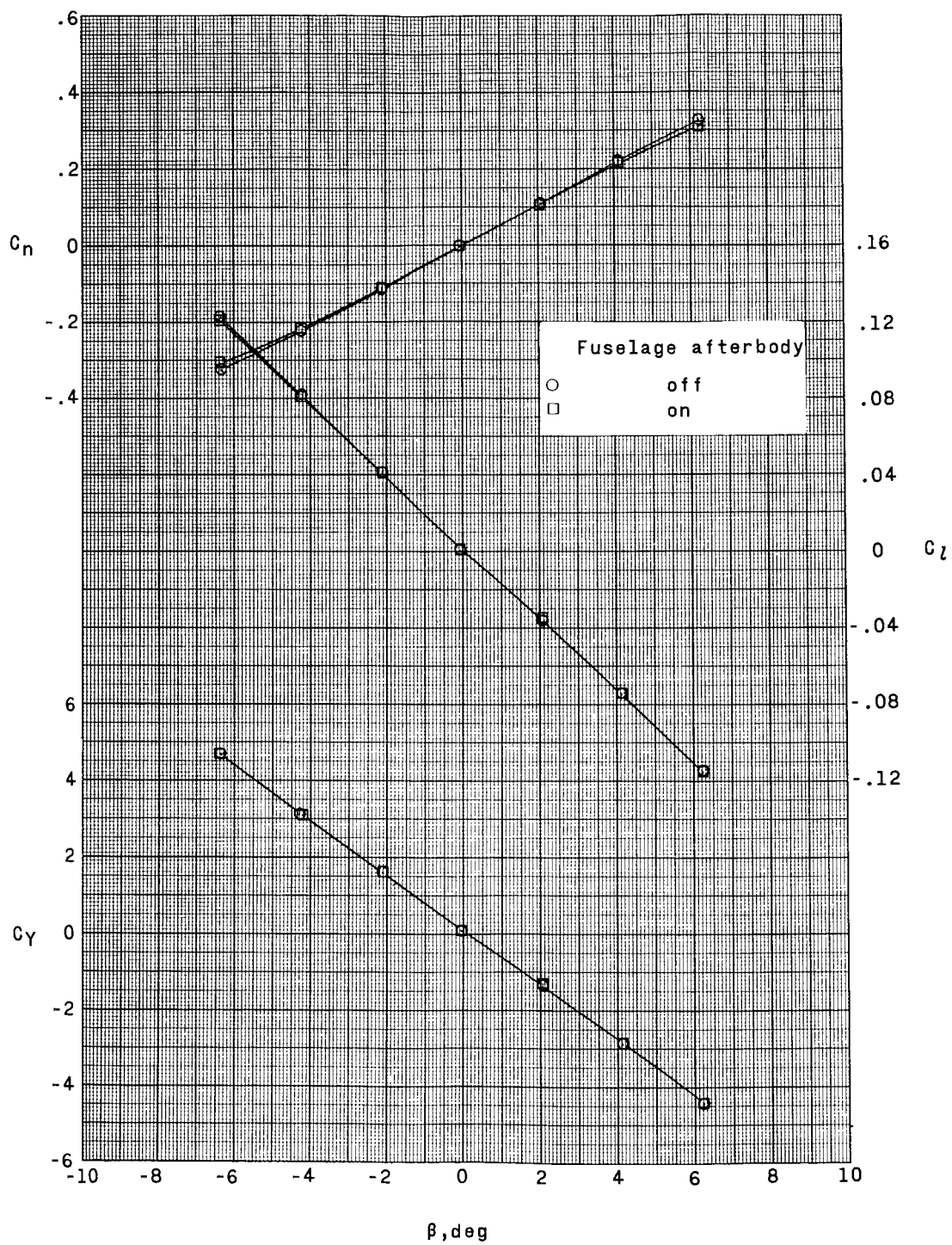
(b) $M = 2.00$; $\alpha = 0.90^\circ$.

Figure 16.- Concluded.



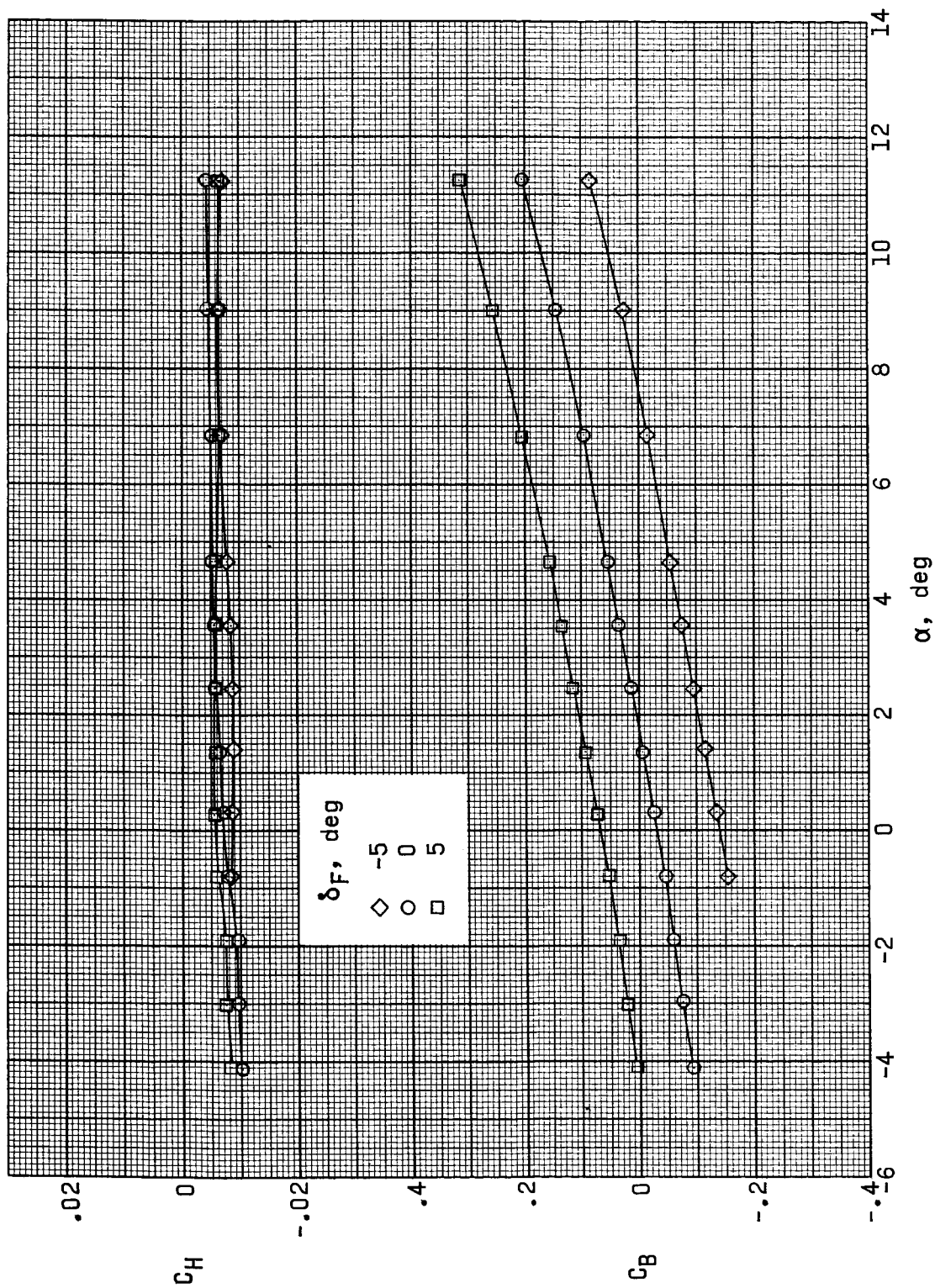
(a) $M = 2.00$; $\alpha = 5.3^\circ$.

Figure 17.- Effect of fuselage afterbody on lateral aerodynamic characteristics. Balance in nacelle; $\delta_F = 0^\circ$; $\delta_P = 0^\circ$.



(b) $M = 2.16$; $\alpha = 1.2^\circ$.

Figure 17.- Concluded.



(a) $M = 1.80$.

Figure 18.- Variation of hinge- and bending-moment coefficients with angle of attack for left tail fin. Balance in nacelle; afterbody off.

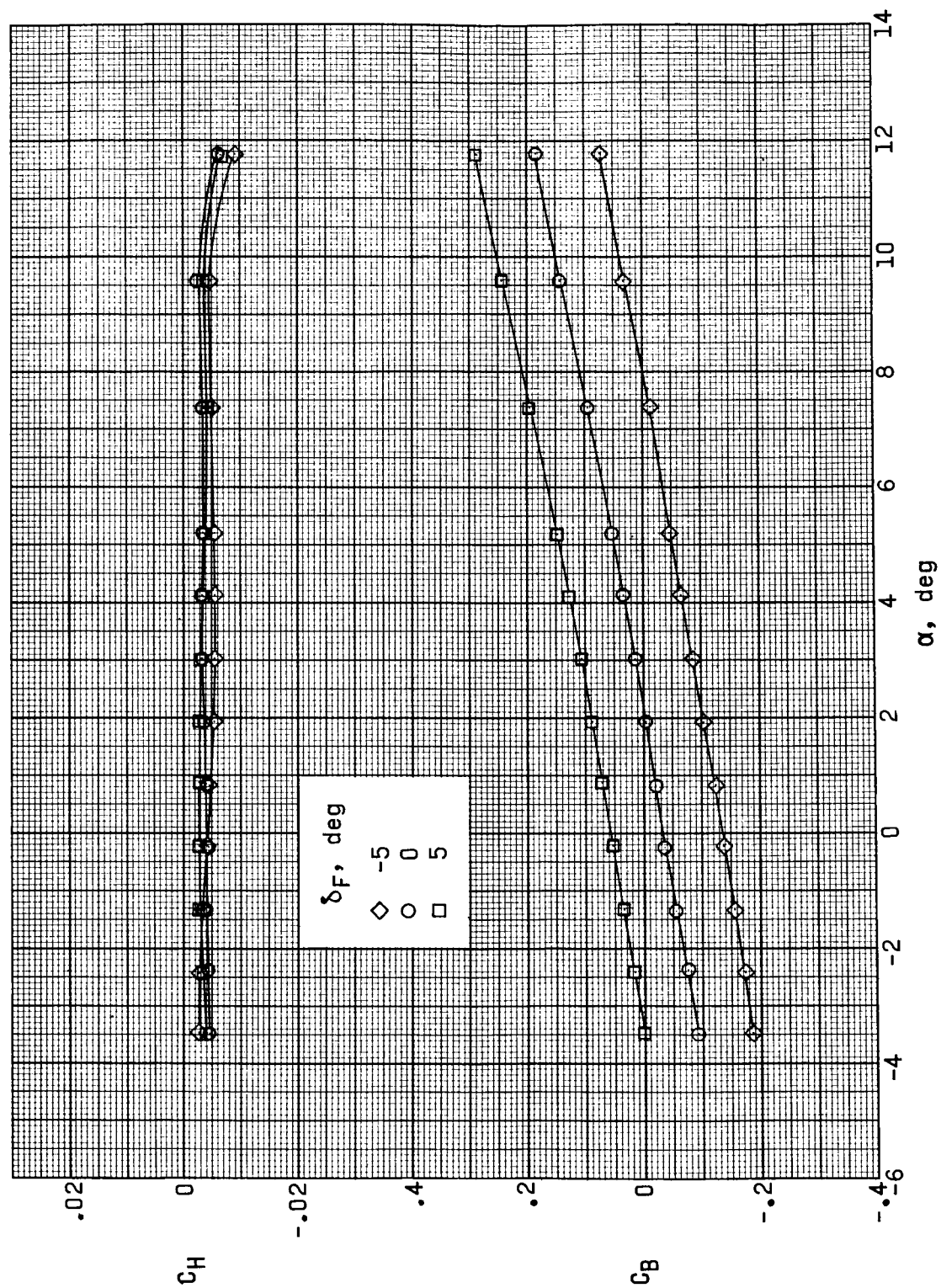
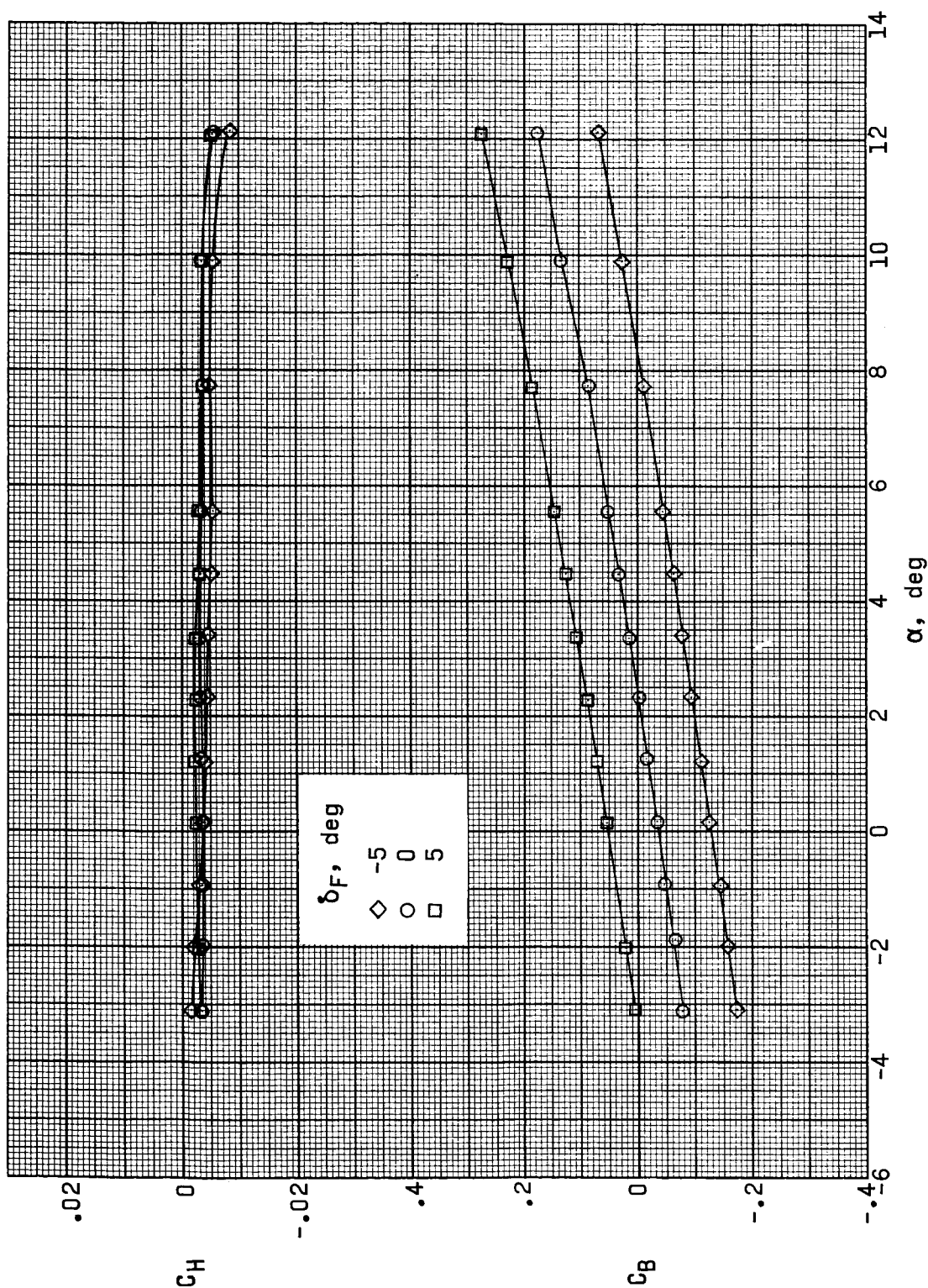
(b) $M = 2.00$.

Figure 18.- Continued.



(c) $M = 2.16$.

Figure 18.- Concluded.

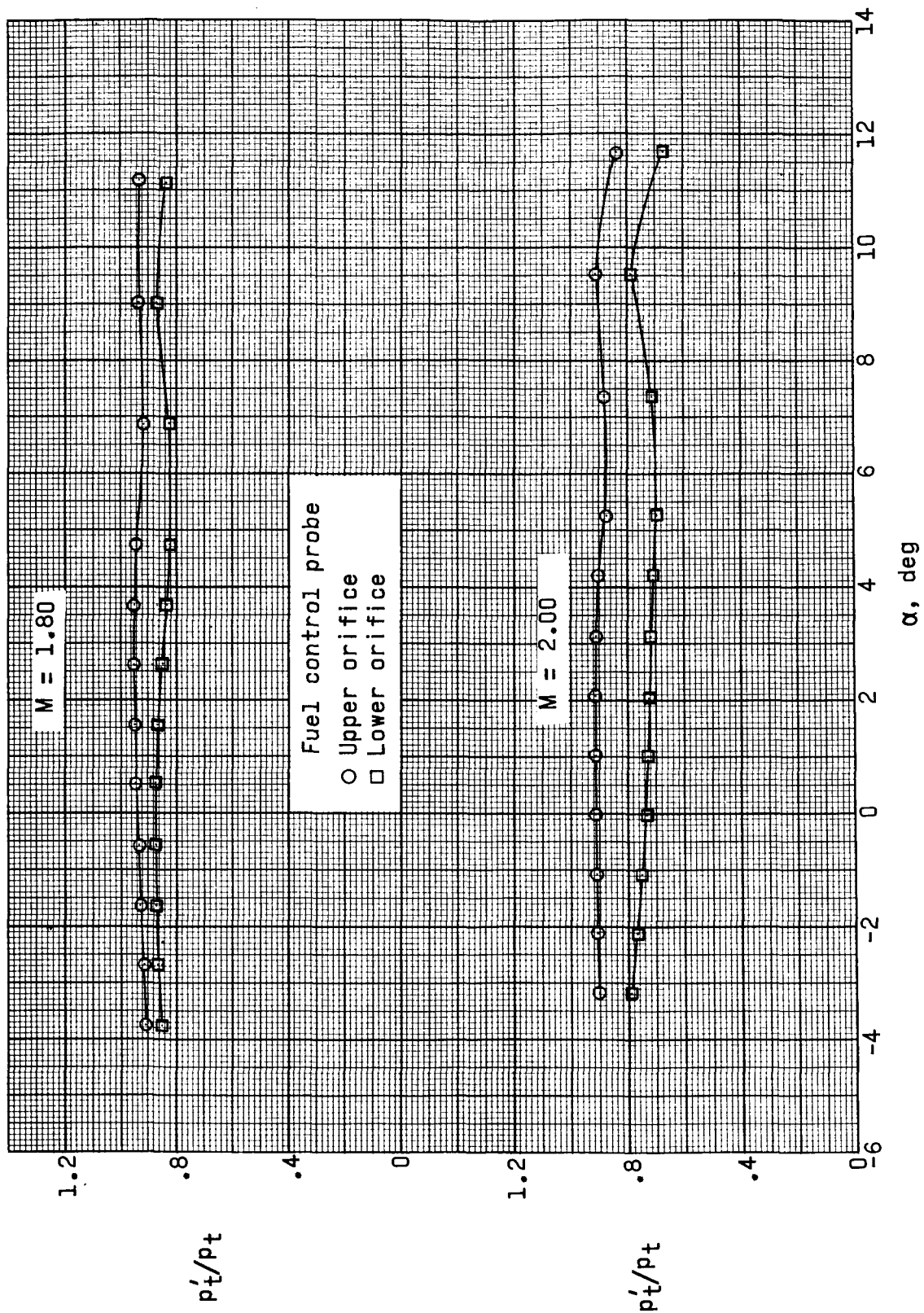


Figure 19.- Variation of fuel-control-probe pressure p'_t/p_t with angle of attack. Balance in fuselage; N1 nacelle.

"The aeronautical and space activities of the United States shall be conducted so as to contribute . . . to the expansion of human knowledge of phenomena in the atmosphere and space. The Administration shall provide for the widest practicable and appropriate dissemination of information concerning its activities and the results thereof."

—NATIONAL AERONAUTICS AND SPACE ACT OF 1958

NASA SCIENTIFIC AND TECHNICAL PUBLICATIONS

TECHNICAL REPORTS: Scientific and technical information considered important, complete, and a lasting contribution to existing knowledge.

TECHNICAL NOTES: Information less broad in scope but nevertheless of importance as a contribution to existing knowledge.

TECHNICAL MEMORANDUMS: Information receiving limited distribution because of preliminary data, security classification, or other reasons.

CONTRACTOR REPORTS: Technical information generated in connection with a NASA contract or grant and released under NASA auspices.

TECHNICAL TRANSLATIONS: Information published in a foreign language considered to merit NASA distribution in English.

TECHNICAL REPRINTS: Information derived from NASA activities and initially published in the form of journal articles.

SPECIAL PUBLICATIONS: Information derived from or of value to NASA activities but not necessarily reporting the results of individual NASA-programmed scientific efforts. Publications include conference proceedings, monographs, data compilations, handbooks, sourcebooks, and special bibliographies.

Details on the availability of these publications may be obtained from:

SCIENTIFIC AND TECHNICAL INFORMATION DIVISION
NATIONAL AERONAUTICS AND SPACE ADMINISTRATION

Washington, D.C. 20546